University of West Bohemia
Faculty of Applied Sciences
Department of Mechanics

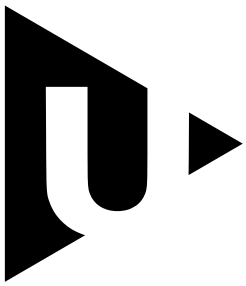

Micromechanical Analysis of Unidirectional Carbon Fiber Composite

Ing. Hana Srbová

DISSERTATION
in Applied Mechanics Submitted in Partial Fulfillment of the Requirements for the Degree of Doctor of Philosophy

Advisor: Ing. Robert Zemčík, Ph.D.
Co-advisor: Ing. Tomáš Kroupa, Ph.D.

Pilsen, 2017

Západočeská univerzita v Plzni
Fakulta aplikovaných věd
Katedra mechaniky

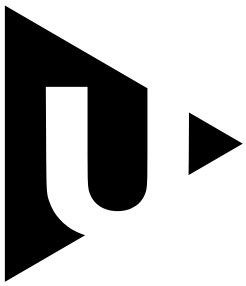

Analýza jednosměrového vláknového kompozitu z hlediska mikromechaniky

Ing. Hana Srbová

DIZERTAČNÍ PRÁCE
k získání akademického titulu doktor v oboru Aplikovaná mechanika

Školitel: Ing. Robert Zemčík, Ph.D.
Školitel specialista: Ing. Tomáš Kroupa, Ph.D.

Plzeň, 2017

I declare that this thesis has been composed by myself and that it has not been submitted, in whole or in part, in any previous application for a degree. Except where states otherwise by reference or acknowledgment, the work presented is my own.

Pilsen, March 30, 2017

.....
Ing. Hana Srbová

Acknowledgements

I would like to express my deep gratitude to Ing. Tomáš Kroupa, Ph.D. and Ing. Robert Zemčík, Ph.D. for their devoted support and human approach. They both became much more than advisors to me.

I would also like to thank all my colleagues, who helped me with different parts of my work. My thanks belong to Ing. Jan Krystek, Ph.D., Ing. Vladimír Lukeš, Ph.D., Ing. Ivan Pirner, Ing. Lukáš Bureš and Ing. Jan Klesa Ph.D.

My gratitude also belongs to my beloved mother for her unconditional and endless support.

Abstract

Aim of this dissertation was to analyze influence of spatial distribution of fibers in the unidirectional carbon fiber composite on overall behavior of the material. The dependency of homogenized material properties of a composite lamina on its degree of irregularity are investigated, proved and described.

Because the real composite material has irregular microstructure, its fiber distribution in different areas of the composite material made of multiple layers of prepreg was determined. Images of the composite cross-section were obtained by scanning electron microscopy and fibers identified by algorithms proposed for automatic fiber detection written in programming language *Python*. The results of the algorithms were compared to ground truth data obtained in another application using *OpenCV* designed for manual fiber identification.

Degree of irregularity of the analyzed microstructure was evaluated by a proposed parameter, which expresses deviation of the analyzed 2D geometry from idealized regular hexagonal fiber distribution. The parameter is suitable for evaluating both, the non-periodic geometry of the real composite cross-section or geometries of periodic unit cells used for finite element analyses. The periodic unit cells were created in an algorithm proposed for generating geometries of unit cells with random fiber distribution.

An automatic tool for performing all steps leading to results of finite element analysis was build in *Python*. Finite element analysis is performed in *Abaqus/CAE* and the results depicted using *ploTRA*, library of functions written in *Python*. Micromodels with proposed unit cells are built, periodical boundary conditions were prescribed and chosen combination of linear or nonlinear material models assigned to the composite substituents by scripts. The loadings were defined in accordance of the type of performed analysis and the results of finite element analysis were processed.

Homogenized material parameters of 200 proposed micromodels with geometries of different degrees of irregularity were identified. A dependence between the parameter evaluating the cross-section irregularity and the range of the resulting homogenized parameters, i.e. degree of material anisotropy, was quantified.

Abstrakt

Cílem této dizertace bylo analyzovat, jaký vliv má rozložení uhlíkových vláken v jednosměrovém kompozitu na celkové chování materiálu. Je zkoumána a popsána závislost homogenizovaných parametrů kompozitové laminy na stupni nepravidelsosti její struktury.

Protože skutečný kompozitní materiál má nepravidelnou mikrostrukturu, je zjištěno rozložení vláken v různých částech řezu kompozitu složeného z více vrstev prepregu. Fotografie řezu kompozitu byly pořízeny pomocí skenovací elektronové mikroskopie a vlákna identifikována algoritmem v programovacím jazyce *Python*. Algoritmus byl navržen za účelem automatické detekce vláken. Výsledky byly srovnány s Ground Truth daty získanými v aplikaci, která využívá *OpenCV* a je určena pro manuální detekci vláken.

Stupeň nepravidelnosti zkoumané mikrostruktury byl vyčíslen navrženým parametrem, který vyjadřuje odchylku analyzované 2D geometrie od pravidelného šestiúhelníkového rozložení vláken. Tímto parametrem lze ohodnotit jak neperiodickou mikrostrukturu skutečného řezu kompozitem, tak geometrie periodických jednotkových buněk použitých v konečnoprvkové analýze. Periodické buňky byly vytvořeny pomocí algoritmu, který byl navržen za účelem generování buněk s náhodným rozložením vláken.

V rámci práce vznikl automatický nástroj, který vykoná veškeré kroky vedoucí k vyjádření výsledků konečnoprvkové analýzy, ty jsou řízeny pomocí skriptů. Analýzy probíhaly v *Abaqus/CAE* a výsledky byly vykresleny v *ploTRA*, což je knihovna funkcí napsaná v jazyce *Python*. Mikromodely s navrženými jednotkovými buňkami byly sestaveny a byly jim předepsány periodické okrajové podmínky. Dále byly složkám kompozitu přiřazeny zvolené kombinace lineárních a nelineárních materiálových modelů. Zatížení bylo definováno podle typu prováděné analýzy. Nakonec byly výsledky konečnoprvkové analýzy zpracovány.

Byly identifikovány homogenizované materiálové parametry 200 navržených mikromodelů s různými stupni nepravidelnosti geometrie. Byla kvantifikována závislost mezi parametrem určujícím tento stupeň nerovnoměrnosti a intervalem, ve kterém se nachází výsledné homogenizované materiálové parametry, tedy mírou anizotropie daného materiálu.

Abstrait

L'objectif de cette these était d'analyser l'influence de la répartition spatiale des fibres dans le composite de fibre de carbone unidirectionnel sur le comportement global du matériau. La dépendance des propriétés de matériau homogénéisé d'une lame composite sur son degré d'irrégularité est étudiée et décrite.

Parce que un matériau composite réel a une microstructure irréguliere, la distribution des fibres dans les zones différentes constituées de couches multiples de pré-imprégnés a été determinée. Les images des sections transversales du composite ont été obtenues par la microscopie électronique a balayage. Ensuite, les fibres ont été identifiées par des algorithmes écrites en langage de programmation *Python* lequel a été conçu pour la détection automatique des fibres. Les résultats des algorithmes ont été comparés aux données de vérité obtenues dans une autre application utilisant *OpenCV* conçue pour l'identification manuelle des fibres.

Le degré d'irrégularité de la microstructure analysée a été évalué par un parametre donné exprimant la déviation de la 2D géométrie analysée de la disposition réguliere hexagonale de fibres. Ce parametre est adapté pour l'évaluation de la géométrie non périodique du coupe transversale aussi bien que la géométrie des cellules particulieres périodiques utilisées pour la méthode des éléments finis. Les cellules périodiques ont été créées par un algorithme proposé pour générer des cellules unitaires avec une distribution de fibres aléatoire.

Un outil automatique pour effectuer toutes les étapes menant aux résultats acquises par méthode des éléments finis a été construit en *Python*. Les analyses par éléments finis sont effectuée dans *Abaqus/CAE* et les résultats sont représentés a l'aide de *ploTRA*, bibliotheque de fonctions écrites en *Python*. Des micromodeles avec des cellules unitaires proposées ont était construites ainsi que les conditions limites ont été prescrites. De plus, les composants de composites ont été également attribués a la combinaison de modeles de matériaux linéaires et non linéaires. Les chargements du materiau ont été définis en fonction du type d'analyse effectuée. Enfin, les résultats obtenues par l'analyse MÉF ont été traités.

Des parametres de matériaux homogénéisés de 200 micromodeles proposés avec des différents degrés d'irrégularité de géométrie ont été identifiés. Une dépendance entre le parametre déterminant cette irrégularité et l´interval des parametres homogénéisés finaux. C'est-a-dire que le degré d'anisotropie du matériau a été quantifié.

Contents

Notation

List of Latin Symbols

a, b, c	[m]	unit cell dimensions
A_{int}	[m^2]	area of intersection
A_{id}	[m^2]	area of analyzed geometry
A_{reg}	[m^2]	area of regular geometry
A_n	[−]	coefficients of relative motion of nodes
$\mathbf{c}$	[m]	fiber center positions
$\mathbf{C}$	[Pa]	material stiffness matrix
d_R	[m]	distance of fibers
d_y, d_z	[m]	dimensions of basic regular geometry
E_{ii}	[Pa]	Young's modulus
E_{m}	[Pa]	Young's modulus of matrix
E_{11}^0	[Pa]	initial Young's modulus of fiber
$\mathcal{F}$	[−]	physical quantity
F_x	[N]	tensile force
g	[−]	shape parameter of Young's modulus of fibers
$\bar{g}$	[−]	fiber grow rate
G_{ij}	[Pa]	shear modulus
l_{seed}	[m]	seed length
Δl	[m]	gage length extension
L	[−]	number of intensity values of image (image matrix)
m, n	[pixel]	image width and height
n_{el}	[−]	number of elements within fiber circumference
n_{f}	[−]	number of fibers
$\mathbf{N}$	[−]	diagonal matrix with integers n_1, n_2 and n_3
p	[pixel]	kernel size
p_γ	[−]	normalized histogram
P_A, P_A	[Pa]	shape parameters of matrix hardening function
P_K, n	[Pa, −]	shape parameters of matrix hardening function
q	[−]	number of segments representing fiber in image

r_1, r_2	$[-]$	residuals
R_f	[m]	fiber radius
R_A	[m]	circle radius for determining degree of irregularity
$K_{i,j}$	$[-]$	kernel element
S	$[-]$	least square fitting method residual
$\mathbf{S}$	$\left[\mathrm{Pa}^{-1}\right]$	material compliance matrix
t	$[-]$	number of boundary points
t_{ij}^col	[s]	collision time of pair of fibers i and j
Δt	[s]	time increment
$\mathbf{T}_\sigma$	$[-]$	stress transformation matrix
$\mathbf{T}_\varepsilon$	$[-]$	strain transformation matrix
u_i	[m]	displacement in direction i
V_f	$[-]$	fiber volume ratio
$\mathbf{v}$	$[\mathrm{m}\cdot\mathrm{s}^{-1}]$	fiber velocities
$\mathbf{X}$	$[-]$	matrix of pixel intensities
$\mathbf{X}^\mathrm{DC}$	$[-]$	matrix of intensities of blurred image
$\mathbf{x}_{123} = [x_1, x_2, x_3]^\mathrm{T}$	[m]	point coordinates in coordinate system (123)
$\mathbf{X}^\mathrm{CLAHE}$	$[-]$	matrix of equalized image ans subimage
$\mathbf{X}^\mathrm{BIN}$	$[-]$	binary image
$\mathbf{X}^\mathrm{WS}$	$[-]$	matrix representing segmented image
(xyz)	$[-]$	cartesian global coordinate system
$(123) \equiv (x_1x_2x_3)$	$[-]$	cartesian local coordinate system of micromodel

List of Greek Symbols

α	$[-]$	intensity of image pixel
$\boldsymbol{\beta}$	$[-]$	list of boundary points of segmented image
γ	$[-]$	contrast limit of CLAHE method
$\boldsymbol{\varepsilon}$	$[-]$	strain
$\boldsymbol{\varepsilon}_\mathrm{e}$, $\boldsymbol{\varepsilon}_\mathrm{p}$	$[-]$	elastic and plastic strains
$\overline{\varepsilon}_\mathrm{p}$	$[-]$	equivalent plastic strain
η	$[-]$	coefficients of mutual influence
μ	$[-]$	Chentsov's coefficients
ν_{ij}	$[-]$	Poisson's ratio
ν_m	$[-]$	Poisson's ratio of matrix
ρ	$\left[\mathrm{kg}\cdot\mathrm{m}^{-3}\right]$	density
φ, ψ, θ	$[^\circ]$	rotation angles about axes
σ_red	[Pa]	equivalent stress
σ_1, σ_2, σ_3	[Pa]	principle stress components
σ_y	[Pa]	yield stress
σ_y^0	[Pa]	initial yield stress
$\overline{\sigma}_\mathrm{max}$	[Pa]	arithmetic mean of strengths
$\tilde{\sigma}_\mathrm{max}$	[Pa]	median of strengths
$\boldsymbol{\sigma}$	[Pa]	stress
Υ	$[-]$	degree of irregularity
ϕ	[m]	distance between fiber center positions
Φ	$[-]$	yield function
Ψ	$[\mathrm{J}\cdot\mathrm{m}^3\cdot\mathrm{kg}^{-3}]$	Helmholz free energy

Abbreviations

CLAHE	–	contrast limited adaptive histogram equalization
FEA	–	finite element analysis
GT	–	ground truth data
LSQ	–	least square fitting method
OAT	–	one-at-a-time method
RVE	–	representative volume element
RANSAC	–	random sample consensus
SEM	–	scanning electron microscope
UC	–	unit cell

Introduction

Unidirectional fiber-reinforced composites have advantageous properties arising also from varying characteristics in different directions. To understand the given composite material, many analyses have to be performed in order to predict its behavior and fully advantage from it. To predict overall mechanical properties of composite materials, a homogenization procedure can be used to relate the constituent properties and the macroscopic behavior. Geometry of a micromodel – representative volume element – used for the homogenization process has to be periodical, capable of repeating. The representative volume element serves to build a fully three-dimensional model and is usually approximated by a geometry with regularly distributed fibers in its cross-section. In general, manufacturing of unidirectional composite materials in general leads to fiber distribution differing from the idealized regular geometry.

The aim of this work is to investigate the influence of spatial fiber distribution on the effective composite material properties. Specific goals set in the author's dissertation theses:

1. Analysis of the influence of specimen width, tab material and length on convenient cyclic tensile test process

2. Tensile tests of epoxy resin and utilization of obtained data for improvement of the material model of matrix of the composite material

3. Produce a unit cell geometry according to the real morphology of a microstructure and analyze the influence of the irregularity of fiber distribution in the composite cross-section on the macroscopic behavior of the material

The dissertation is divided into five chapters followed by conclusions, appendices, authors bibliography and references. The first chapter summarizes selected published works of other authors, which are dedicated to the related fields of research as the topic of this work.

Second chapter deals with experimental tensile tests, which equip the author by experimental data necessary for analyses of the examined composite material. Additional tensile tests and analysis of the tensile test configurations for specific material type and orientation are performed in Appendix A.

In the third chapter, the composite material is subjected to image processing analysis. Images of the composite cross-section are obtained by scanning electron microscopy

and enclosed in Appendix B. Degree of irregularity described by proposed parameter is evaluated for microstructure in the images. Algorithms for automatic detection of fibers from the images of cross-section are built.

The fourth chapter states material models which will be further used for the composite substituents, fiber and matrix, and for analysis of material anisotropy. One of the material model was proposed with respect to behavior of epoxy resin. Data obtained from cyclic tensile tests of the specimens made of epoxy resin and cured for different time periods are in Appendix C.

In the last and the most comprehensive chapter a homogenization approach using a periodic geometry and periodic boundary conditions is proposed. Transition from the microstructure to the macroscopic response is executed using analyses in finite element software. The chapter describes the procedure of building a micromodel and defining parameters for finite element analyses and acquisition of the results. Used micromodels are subjected to several sensitivity analyses, which prove the suitability of chosen material models and geometric properties. Results of the finite element analyses are summarized at the end of the chapter. Degree of anisotropy of several micromodels is identified and the results of different micromodel cross-section geometries are compared. Homogenized material properties are identified for numerous micromodels with cross-sections distributed on a wide interval of degree of irregularity. Anisotropic properties are depicted in form of a dependency on the parameter evaluating the degree of irregularity. The results illustrate the effects of the fiber spatial distribution in terms of the overall properties. From these findings, elastic properties and response to mechanical loading can be obtained for the design of composite structures with the knowledge, how precise the results are for a composite material with known degree of irregularity.

In the conclusions, the results of the work are summarized and the consequences of the analyses are discussed. The direction of future author's work is delineated.

Chapter 1

Current State

Hmogenization process is crucial, when identifying the overall behavior of composites, which are characterized by being consisted of phases of different material properties. Homogenization may be done analytically or numerically by using finite element method (FEM).

1.1 Analytical Homogenization

In case of the analytical homogenization, the resulting effective parameters are described by partial differential operators mainly with constant coefficients. It is necessary to solve a boundary value problem on a periodic cell when defining the coefficients, a so-called cell problem.

One of the methods of homogenization of a material with a periodic substructure is a homogenization using an asymptotic expansion (AEH – Asymptotic Expansion Homogenization) [8, 9, 10], which leads to explicit equations. Advantage of this method is the degree of freedom reduction and the ability to ensure the deformation and stress state on the microscopic level at a given macroscopic equilibrium state. Such procedure is called a localization.

If the material does not have a periodic microstructure, there are preferable methods being used for homogenization, for example a G-convergence method [11] is suitable for symmetric tasks, for non-symmetric tasks a H-convergence method is suitable [12].

In [13] authors introduce a homogenization method based on a two-scale approach. The homogenized parameters are identified by solving a task with periodic boundary conditions applied on a representative volume element, which represents a mesoscale and is further divided into subdomains (approximately of inclusions size). The subdomains represent the microscale. The solution of this method is a sum of a smooth mesoscale component and microscale correction component.

A mean-field theory [14] is used in [15], where scaling is shown on crystallic materials, which are considered as a multilevel structure. An elastoplasticity problem is processed by a continuous description and its origin is explained by dislocations. A microscopic

elastoplastic medium has a dimension of crystals, mesoscopic medium has a dimension of distances between individual dislocation planes and a macroscale id on the material dimension level.

Several approaches based on homogenization of locally periodic structures with strong heterogeneities are summarized in [16]. The solution is based on asymptotic analysis of partial differential equations with oscillating coefficients. The strong heterogeneities are represented by coefficients are dependent on the scale, for example elasticity in case of phononic materials or permeability in case of fluid-saturated porous media. Herein a homogenized model of phononic material is stated, which is the a bi-phase material with a periodic structure and big contrast at the elastic coefficients of the phases. These materials have the ability to suppress transmission of elastic waves at certain frequencies.

A Mori-Tanaka homogenization method [17] was formulated in 1973 and deals with the average stress designation in matrix of materials with inclusions. It is shown in the work, that the average stress in the matrix is uniform and independent of the position of the domain, where the average behavior is examined. The actual stress in matrix consists of average stress and the locally fluctuating stress. The average stress vanishes in the matrix. To consider effects of interaction among inclusions, average elastic energy is used. The Mori-Tanaka homogenization method is used for instance in [18] and [19].

1.2 Numerical Homogenization

In case of the numerical homogenization a repeating (periodic) volume of a heterogeneous microstructure (RVE – representative volume element) is built. These volume elements represented by a unit cell are modelled with the use of finite element method (FEM). After applying a load corresponding to the real material loading we obtain the response. The required homogenized material parameters can be identified by minimizing the difference of load/response dependencies obtained numerically and experimentally.

Results of two RVE types built on the base of square and hexagonal approximation of fiber distribution in case of a unidirectional composite are compared in [20]. A differential quadrature element method (DQEM) is used, where the continuity of displacements between neighboring elements and tensile force reciprocity has to be maintained. The proposed method allows the eight-node grid (3 elements in case of the square fiber distribution and 4 in case of the hexagonal fiber distribution) to model the unit cell, whereas much more elements are required for geometric description of the unit cell in the case of finite element analysis. The DQEM method leads to the same Young's modulus and Poisson's ratio in case of both types of RVE. Admittedly there are differences at stress and strain decomposition in the cross-section of the volume elements as well as the strain boundary curves decompositions.

An algorithm for automatical building of 3D finite element models of fiber composited with high volume fraction of fibers was proposed in [21]. Geometry of a unit cell results by moving the fibers in a composite cross-section from their regular hexagonal distribution. The model also considers the random strength distribution within fibers by

a randomly distributed corruptible (damagable) layers, which are planes with different strengths whose normals are identical to the fiber direction. In mentioned work, the effect of strength distribution of fibers on mechanical response and overall strength of the composite is investigated.

The numerical methods may also include methods based on the modelling of cells, which have multiscale features. A 3 dimensional elastoplastic block model consisting of 8 cells, which is able to simulate behavior of particle and fiber composites is used in [22].

1.3 Mixture Approach

Formulae based on the mixture theory use composite constituents with weights related to their volume fractions to determine the macroscopic elastic constants. Hill [23] considers the composite as one spherical element. Single fiber is surrounded by matrix in the shape of a cylinder and the substituents are embedded. Elastic behavior of two solid phases firmly bonded together (both isotropic) is considered. The shape of the inclusions is not restricted, it may be fibrous, spherical, etc. and they can form any concentrations in the composite, which is in the work called a mixture. The overall parameters of the mixture are expressed by their bounds as functions of the parameters of the mixture constituents.

Bounds of effective elastic moduli for a multiphase material were also formulated by Hashin and Shtrikman. A variational principle involving elastic polarization tensor in [24] shows a good result for experimental results. Such bounds of effective moduli should be a good estimation when the ratios between the phases are not too large.

Hashim and Rosen [25] formulate the functions determining bounds of elastic moduli for materials which are reinforced by circular fibers. The exact homogenized parameters are considered to be the parameters obtained for hexagonal fiber distribution and the approximate parameters from random fiber distribution.

Different variations of equations for approximation of the effective (reduced) material parameters of reinforced materials are proposed in different works. They differ in assumptions for the material of the constituents and also in assumptions for the spatial distribution of the reinforcements and their geometries. A set of equations for a variety of fiber geometries were formed by Halpin and Tsai and are reviewed in [26].

1.4 Morphology of a Microstructure

Overall properties of heterogeneous microstructures such as man-made composite materials or biological tissues can be obtained by transition from local material properties (properties of the phases) to those of a homogenized mixture [27]. This can be examined in the context of statistical geometry [28, 29, 30] or by evaluating images of the microstructure manually [31] or by automatic geometry evaluation using computer vision tools [32].

The work [30] presents a review of basic concepts and hypotheses associated with quantification of microstructure morphology. Several statistical descriptors suitable for the microstructure characterization of a two-phase random heterogeneous media of arbitrary phase geometry are examined. One method uses the principle of so-called ensemble where each member of the ensemble is described by a random stochastic function that equals to one when point lies in given phase and zero otherwise [28, 29]. Another method uses the approach found in statistical mechanics of liquids where the particulate composite is described only by the centers of fibers using a fundamental function and statistical moments [33]. This approach, however, is only applicable to composite having inclusions of identical shape. The work is concluded with numerical analysis with the objective to identify a number of particles within RVE required for a sufficiently accurate representation of the behavior of real composite using FEM based on the extended Hashin-Shtrikman variational principle [34].

Work [35] compares transverse elastic properties of two microstructures of fiber reinforced composites – periodic (hexagonal) and random. The analyses of high volume fractions and high Young's modulus contrast between fibers and matrix identified by finite element simulations showed that the microstructure strongly affects the effective properties (unlike microstructures with low fiber volume fractions and low Young's modulus contrasts).

In [31], images of tissue samples obtained by transmission electron microscopy (TEM) are processed. Spatial arrangement of a cluster of smooth muscle cells in the tissue is assessed in order to choose proportions and orientations of ellipsoids approximations. The ellipsoids are used in a 3D reconstruction (micromodel) of the cells in the tissue and homogenized material properties of the micromodel of the examined tissue are further identified. Delauny triangulation method was used to assess anisotropy of the cells center distributions in the image. Triangulation method is the simplest method to evaluate spatial distribution of 2D geometric objects (2D images of 3D objects).

Groups of potential microstructures were created in [32], to classify images of examined microstructure. A support vector machine (SVM) was trained to classify the microstructures on microstructural signatures, which were created by processing a large and diverse microstructural image data sets.

When determining the geometry of a unit cell, which represents the micromodel, thus it influences the identified homogenized material parameters, it is crucial to know the volume ratio of fiber and matrix (in case of a biphase composite material). The volume ratio significantly influences the results of numerical analyses [36] as well as the homogenized characteristics obtained from the simplified relations. Unfortunately, the volume ratios given by the manufacturer may not be in all cases corresponding with the real volume ratios. For example volume ratio of fibers in case of a composite specimen manufactured by a transfer molding method usually varies by 10% [37].

There are a several standard methods for designation of the real fiber volume ratio. The matrix material may be removed by a matrix digestion, where the matrix is cauterized by a mordant or by an ignition loss, where the matrix material is incinerated (burnt). The remaining fibers are weighed and the volume ratio of fibers is identified from the

weight ratio. Other methods benefit on divergent thermal conductivity of fiber and matrix material or different coefficients of thermal expansions. It is also possible to obtain the real volume ratio of fibers from an image of the composite cross-section. This optical method allows to allocate the fibers and the outcome may include also the real fiber distribution.

The fiber distribution is commonly approximated by a hexagonal distribution when building the unit cell. Both, the idealized fiber distributions as well as the real fiber distribution obtained from images of the composite cross-section are considered in [38]. [39] examines the effect of fiber distribution in composite cross-section on local stresses and failure initiation.

[40] develops a computational model to explicitly determine transversely isotropic elastic constants of a unidirectional composite as a function of microstructure parameters. A standard finite element homogenization technique of a periodic representative volume element is used. Different shapes of fiber layout patterns in the RVE cross-section are analyzed.

1.5 Material Models

Composite materials exhibit highly anisotropic and non-linear behavior, therefore different material models are used to simulate their overall behavior. Different approaches are used to calibrate the material parameters of such models.

In case of anisotropic material, both the normal and shear components of strain affect both the normal and shear components of stress. In case of orthotropic material, the normal and shear components are decoupled, normal stresses only cause normal strains and shear stresses only cause shear strains. Furthermore, individual shear stresses are decoupled from each other.

If the latter formulations are used to determine overall properties of the composite material, it is crucial to know material properties of all substituents. Not all these data are always available from the manufacturer. There are several publications reporting the properties for specific materials used for the composite. [41] for example lists the material parameters for four types of epoxy matrices and four types of fibers made of glass and carbon. Also overall properties of the unidirectional laminae of carbon and glass fiber composites are listed. Typical stress/strain curves for the considered laminae under variety of uniaxial loadings are shown.

Material parameters of the composite substituents can be accessed using experimental tests. There are several types of tests, which can be performed, typically tensile tests, pressure tests, bending test or shear tests.

In the proposed work, behavior of a composite material made of unidirectional carbon fibers with high stiffness and epoxy matrix is examined. To do so, tensile tests are performed on specimens with different orientations of fibers according to the loading direction. The material exhibits nonlinear behavior, when loaded in the direction of fibers. Therefore the fiber may be considered as nonlinear. Typically, the fibers are modelled as orthotropic material with the plane of isotropy perpendicular to the fiber

axis. Due to the extremely small dimensions of fibers in the transverse direction, ranging several micrometers, it is difficult to obtain the material parameters for this substituent on its own.

The matrix behavior may be observed from tensile tests performed on specimens with fiber oriented perpendicularly to the direction of loading force. To perform tests on specimens made of the epoxy resin is also a way to obtain the matrix material specifications. The matrix may be considered as material with viscoelastic elastoplastic behavior. Damage behavior can be also observed from cyclic tests.

[42] presents an approach to tune the nine parameters of a compliance matrix relating Green-Lagrange strain and Cauchy stress for purposes of linear finite element method. The orthotropic materials are used for simulations in computer graphics and the work describes a method for tuning the material parameters by parametrizing six Poisson's ratios by a one-dimensional parameter family similar to relationships between parameters of isotropic material.

Transversely isotropic hyperelastic material models are used in [43] to simulate biological tissues. To characterize the used material, the hyperelastic model is fitted to experimental data. Strain energy functions with pseudo-invariants are included into the response to the transversely isotropic models to identify the material parameters using uniaxial and biaxial mechanical tests.

Overall behavior of composite materials with phases having different properties can be obtained by different approaches. Common indicator of majority of the approaches is the knowledge of properties of the constituents of the considered material. Also the geometry of the microstructure is beneficial to be investigated before the homogenization approach is chosen.

Chapter 2

Tensile Tests

To understand the mechanical behavior of a material and obtain data for material specifications, quality assurance and structural design and analysis, mechanical tests need to be performed. Mechanical testing is the way to determine how real materials behave when they are subjected to loads. The usual procedure is to place specimens of the material in testing machines, apply the loads, and measure the resulting deformations (i.e., changes in length, deflections, rotations or changes in diameter). There can be either static or dynamic loading applied according to the capability of the testing machines and desired material properties. The experimental test methods differ also by type of load applied to the specimen. Among the basic experimental methods, tensile tests, compressive tests, bending tests, shear tests or torsional tests are counted.

For oncoming analyses of a composite material using micromodel in finite element software, the behavior of composite material needs to be tested. Static tensile tests were performed to obtain experimental data for material specification for finite element analysis.

The tensile test methods described for instance in [44] are designed to produce tensile properties in the test direction such as:

- ultimate tensile strength
- ultimate tensile strain
- tensile chord modulus of elasticity
- Poisson's ratio
- transition strain

Tensile tests in this work were performed on testing machine *Zwick/Roell Z050* on continuous fiber reinforced composite material with high modulus carbon fibers and epoxy resin – SE84LV-HSC-450-400-35 and Hexply 913C-HTS(12k)-5-40. The thin flat stripes (coupons) of material having a constant rectangular cross-section and different fiber orientations θ (Fig. 2.1) were cut from plates by abrasive water jet. Water jet was chosen

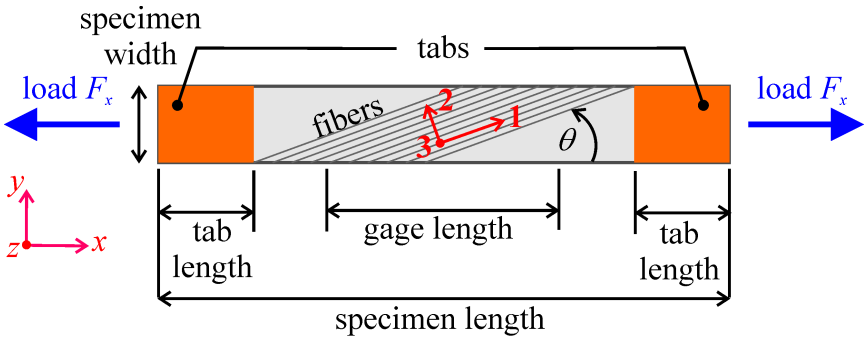

Figure 2.1: Geometry of specimen for simple tensile tests with local coordinate system (123) and global coordinate system (xyz).

because apart from other cutting and finishing techniques, such as laser cutting, cutting with rotary tools and cutting with blades, water jet does not affect the composite structure by potential heat. Some composite laminates can delaminate when being cut, especially poorly bonded resin to reinforcement. Water jet has positive results from the delamination point of view. Disadvantage of the water jet cutting technique is moisture absorption of the composite material.

2.1 Standards

Because a physical property of a material is often affected by the precise method of testing, norms and requirements for ensuring repeatable experiments and reliable outcoming data are established in technical standards. One type of a technical standard is a standard test method. It describes a definitive procedure that produces a test result. Standard test methods order uniform test conditions for determination of the desired material properties based upon general principles.

Factors that influence the tensile response and should therefore be reported include the following: material, methods of material preparation and lay-up, specimen preparation, specimen conditioning, environment of testing, specimen alignment and gripping, speed of testing, time at temperature, void content, and volume percent reinforcement.

Two international standards and one Czech standard were an inspiration (Tab. **??**) for specimen manufacturing and tensile tests in this work:

- ISO 527–5 Plastics – Determination of tensile properties – Part 5: Test conditions for unidirectional fiber-reinforced plastic composites [45]
- ASTM D 3039/D 3039 M Standard Test Method for Tensile Properties of Polymer Matrix Composite Material [44]
- ČSN EN 2561 Aerospace series – Carbon fibre reinforced plastics – Unidirectional laminates – Tensile test parallel to te fibre direction [46]

Table 2.1: Tensile test configuration given by stndards.

	ISO	ASTM	ČSN
specimen width	15 ± 0.5 mm	15 mm ±1%	15 ± 0.5 mm
specimen length	250 mm	250 mm	250 ± 1 mm
thickness	1 ± 0.2 mm	1 mm ±4%	1 ± 0.2 mm
tab length	> 50 mm	56 mm minimum $L_{min} = \frac{F^{tu}h}{2F^{su}}$ [1]	65 ± 15 mm
tab thickness	0.5 to 2 mm	1.5 mm ±1%	0.5 to 1 mm
gage length	50 ± 1 mm	–	–
dist. betw. tabs	150 ± 1 mm	–	–
dist. betw. grips	136 mm	–	–
tab material	cross-ply or fabric glass fiber/resin laminate	continuous E-glass polymer matrix mat. [2]	glass fabric/epoxy laminate ±45°
	material under test	material under test	–
	emery or sand paper	emery cloth	–
	–	incorporated steel	–
test speed	2 mm/min	2 mm/min [3]	mutual disp. of grips 2 mm/min

[1] F^{tu} – ultimate tensile strength of coupon material in MPa, h – coupon thickness, F^{su} – shear strength of adhesive coupon material or tab material (the lowest) in MPa

[2] woven or unwoven in a [0/90] laminate configuration, tab material applied at 45° to the force direction to provide a soft interface

[3] The strain rate should be selected so as to produce failure within 1 to 10 min.

Standard test method ASTM D 3039/D 3039 M also defines three-part failure mode codes for recording the mode and location of failure of the tested specimen. Failure modes and locations are shown in (Fig. 2.2) and (Tab. 2.2) [44].

If a significant fraction of failures in a sample population occurs within one specimen width of the tab or grip, the force introduction into the tested material is supposed to be reexamined. The concerned factors should include the tab alignment, tab material, tab angle, tab adhesive, grip type, grip pressure and grip alignment.

2.2 Experiments

Simple tensile tests were performed on specimens (Fig 2.3) cut from a plate 1.8 mm thick made of 8 layers of prepregs SE84LV-HSC-450-400-35 with the same fiber orientation θ. One layer of the unidirectional prepreg was 0.21 mm thick made of high-modulus continuous fibers and epoxy (polymer) resin. The specimen were 150 mm long, 10 mm wide and the gage length was 60 mm. Parameters of the fiber material specified by the manufacturer are in Tab. 2.3.

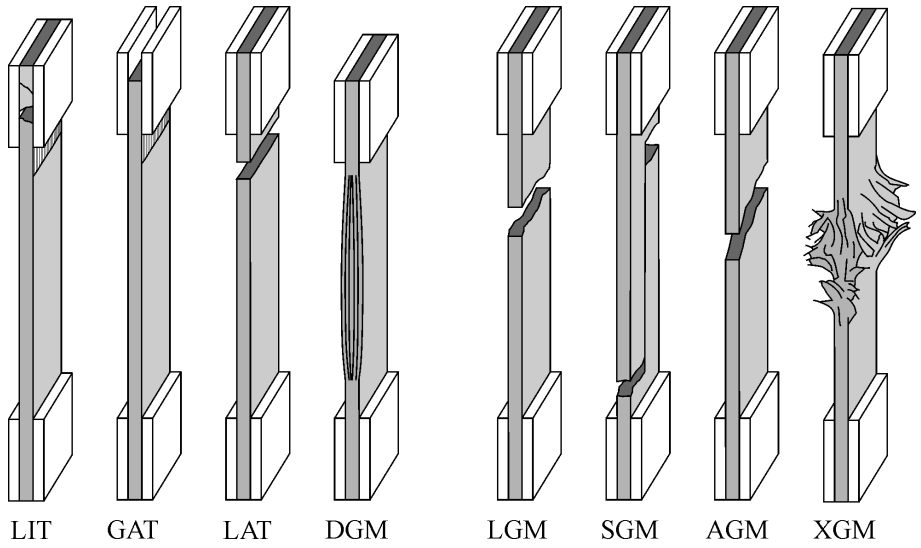

Figure 2.2: Failure modes and locations.

Table 2.2: Identification codes for failures of specimen loaded by tension.

first character		second character		third character	
failure mode	code	failure area	code	failure location	code
angled	A	inside grip/tab	I	bottom	B
edge delamination	D	at grip/tab	A	top	T
grip/tab	G	< width from grip/tab	W	left	L
lateral	L	gage	G	right	R
multi-mode	M	multiple areas	M	middle	M
long. splitting	S	various	V	various	V
explosive	X	unknown	U	unknown	U
other	O				

Specimens with constant rectangular cross-section were clamped in the grips of the testing machine. Aluminium or friction emery cloth tabs were placed between serrated wedge grips of the testing machine and the specimen to transfer the force into the specimen and provide necessary friction in order to avoid slipping during the test. The aluminium tabs were bonded by a two component epoxy adhesive *Araldite AV 138* with Hardener *HV 998* [47]. Emery cloth tabs were held in place by the pressure of the grip and enclosed between the specimen and grips with the rough side oriented towards the specimen.

The specimen were monotonically loaded in tension by test speed of 2 mm/min defined by the testing machine crosshead. The loading force increased up until failure while recording extension of the gage length (Fig. 2.3) and loading force.

Data obtained from the test – loading force F_x, gage length extension (displacement) Δl and time t were exported into *.TRA data files. Experimental data were processed by a library of functions named *ploTRA* programmed in *Python 2.7* by Ing. Tomáš Kroupa Ph.D.

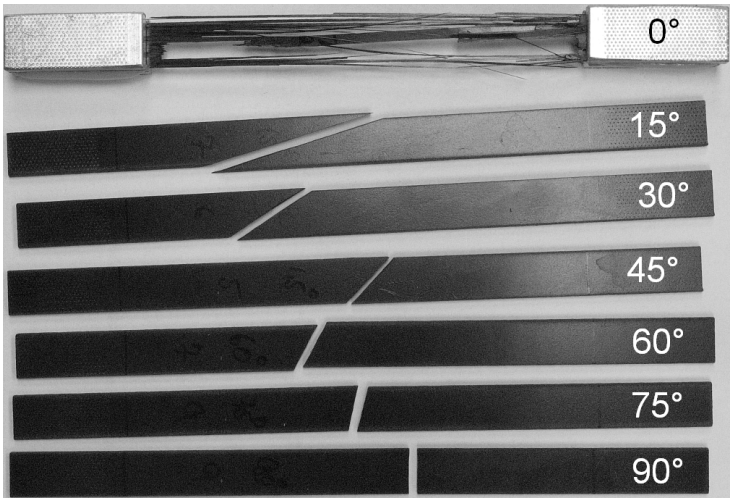

Figure 2.3: Fractured specimens with different fiber orientations θ.

at the Department of Mechanics of University of West Bohemia in Pilsen. Data for further analysis were averaged for each group of fiber orientation θ in sense of strain ε_x.

Configuration of tab materials and specimen number for the groups of specimen with different fiber orientation are in Tab. 2.4.

Table 2.3: Parameters of prepreg SE84LV-HSC-450-400-35 fibers specified by the manufacturer.

E_{11}	[GPa]	230.00
$E_{22} = E_{33}$	[GPa]	15.00
ν_{12}	[−]	0.28
$G_{12} = G_{13}$	[GPa]	4.50
$G_{23} = \frac{E_{22}}{2(1+\nu_{23})}$	[GPa]	5.77

Only one tensile test for fiber orientation $\theta = 0°$ produced successful failure mode according to ASTM D 3039/D 3039 M. The remaining specimens failed inside tabs or the tabs were detached before the specimens failed.

Therefore, further simple and cyclic tensile tests were performed to find the suitable combination of tab material and geometry and specimen geometry to produce failures of the specimens in the gage area. The tensile tests were performed by loading the

Table 2.4: Configuration of specimen and tabs for simple tensile tests.

specimen		tabs	
fiber orientation θ [°]	# of samples	material	length [mm]
0	1	aluminium	25
15, 30, 45, 60, 75, 90	10	emery cloth	25

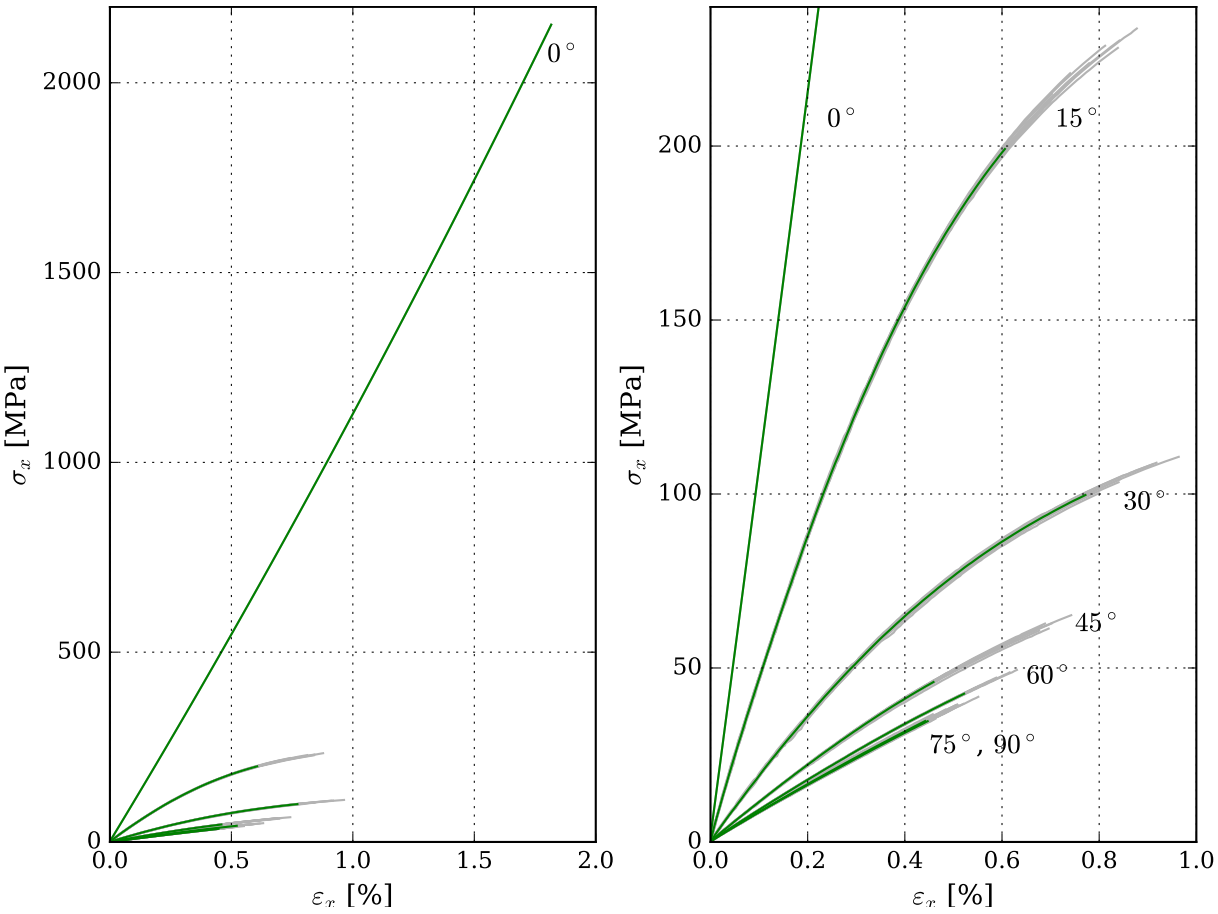

Figure 2.4: Stress-strain dependencies obtained by simple tensile tests (grey) with averaged data for every fiber orientation θ (green).

unidirectional high-modulus long-fiber composite Hexply 913C-HTS(12k)-5-40 in the fiber direction (Appendix A).

The specimen with fiber orientation $\theta = 0°$ is fractured by explosive failure mode along the whole specimen length caused by fiber failures. Specimen with nonzero fiber orientations θ were fractured by angled failure mode caused by matrix failure (Fig 2.3).

Chapter 3

Morphology of Composite Microstructure

All methods of manufacturing fiber reinforced composites result in a non-regular fiber distribution in the composite cross-section. The irregularity of the microstructure influences the homogenized material properties of the resulting lamina. Deviation of local fiber volume fraction V_f in the composite also affects the material behavior.

For modelling the composite material on a microscale level, the real fiber distribution in the matrix is crucial for example for analysis of homogenized material properties. It is also important for instance for further manufacturing of the composite. In this part of work, a new parameter describing the degree of irregularity of a microstructure is proposed and two methods for determining real fiber volume ratio and fiber center positions are used.

3.1 Quantification of Degree of Irregularity

For further analyses, it was crucial to define a parameter quantifying the irregularity of fiber distribution in cross-section perpendicular to fiber direction in unidirectional composite. The proposed parameter, designated as Υ, was designed to quantify deviation of fiber distribution in a composite cross-section from idealized hexagonal fiber distribution having the same fiber volume fraction V_f.

The aim of the presented work is to investigate, prove and describe a dependency of resulting homogenized characteristics (properties) of a composite lamina on Υ. Such dependency could be useful for instance during processes of construction. The ability to predict deviations of particular properties of a lamina with known microstructure from properties of a material with idealized cross-section geometry would provide useful information.

Parameter Υ expresses the degree of irregularity related to hexagonal fiber distribution

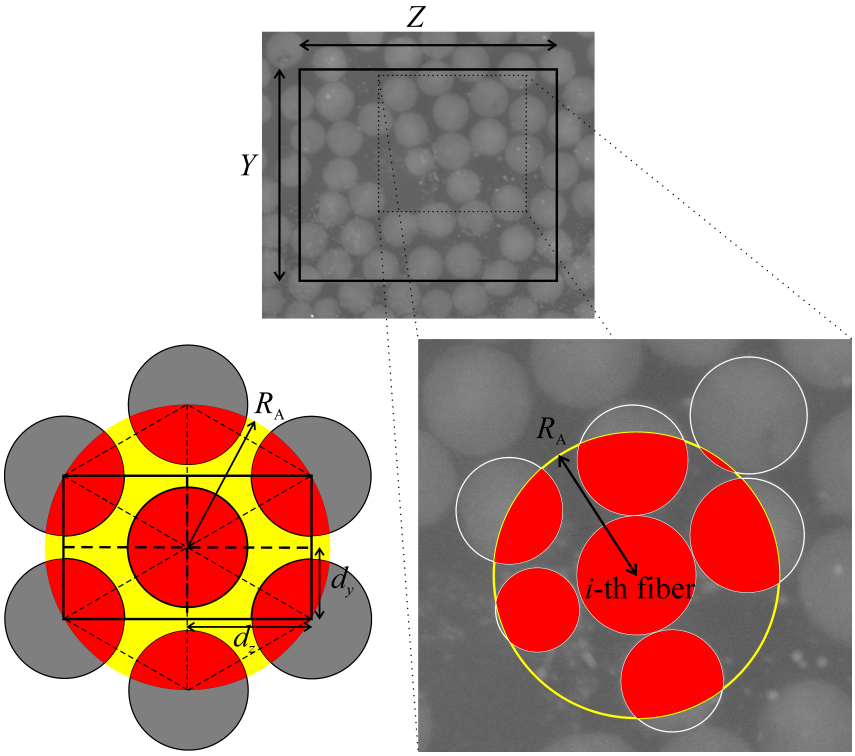

Figure 3.1: Hexagonal (left) and irregular (right) fiber distribution with a circle (yellow) of diameter R_{A} covering a red area of fibers $A_{\mathrm{int}}^{\mathrm{reg}}$ (left) and A_{int}^{i} (right).

with fiber volume ratio V_{f} of the identified geometry

$$\Upsilon = 100 \cdot \frac{A_{\mathrm{reg}}}{A_{\mathrm{id}}} \sum_{i=1}^{n_{\mathrm{f}}} \left| \frac{A_{\mathrm{int}}^{i} - A_{\mathrm{int}}^{\mathrm{reg}}}{A_{\mathrm{int}}^{\mathrm{reg}}} \right|, \tag{3.1}$$

where $A_{\mathrm{reg}} = 4 \cdot d_y \cdot dz$ is area of the basic repeatable geometry for regular fiber distribution (Fig. 3.1 – left), and $A_{\mathrm{id}} = Y \cdot Z$ is area of the analyzed rectangular geometry. For a geometry with regular fiber distribution, the dimensions Y and Z are multiples of d_y and d_z, respectively. Number of fibers in the analyzed geometry is n_{f} and $A_{\mathrm{int}}^{\mathrm{reg}}$ is area of intersection of fibers with a circle having diameter R_{A} and center in fiber center in a geometry with regular hexagonal fiber distribution (Fig. 3.1 – left).

The diameter R_{A} was chosen as the distance of neighboring fibers in the regular distribution, and A_{int}^{i} is area of fibers covered by a circle of diameter R_{A} and center in the center of the i-th fiber (Fig. 3.1 – right) in the analyzed geometry (Fig. 3.1 – top).

The geometry for which Υ is evaluated can be obtained either from real microstructure, where no periodicity can be found, or a periodical microstructure built for finite element analysis. In case of the periodical microstructure, n_{f} is the number of original fibers. In the latter case, where the structure cannot be repeated, n_{f} is number of fibers which have center in the area for which Υ is quantified.

3.2 Preparation of Specimen for Microscopy

Five specimens were cut by water jet from five carbon/epoxy composite plates with unidirectional long-fiber layers. The plates were 4.3 mm, 3.0 mm, 1.1 mm, 0.9 mm, and 0.8 mm thick. Each plate was made from different number of prepreg layers and cured in autoclave. Specimens having a size of 5 mm × 10 mm were cut with cross-section having one side perpendicular to the fiber direction.

The specimens were embedded in resin and their cross-section perpendicular to the fiber direction was polished on a polishing machine (Fig. 3.2).

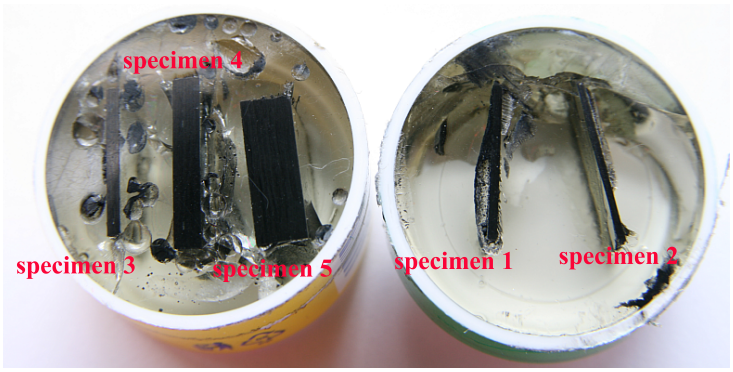

Figure 3.2: Composite specimen embedded in resin.

3.3 SEM Images of Composite Cross-section

Images of different parts of the polished composite cross-section (see Appendix B, Figs. B.1a, B.2a, B.3a, B.4a and B.5a) were taken by scanning electron microscope (SEM). The monochromatic images were taken with 2 different magnifications of 1000 and 4000. In case of magnification 1000 theresolution was 1 pixel ≈ 0.16 μm (Figs. B.1b, B.1c, B.1d, B.2b, B.2c, B.2d, B.3b, B.3c, B.3d, B.4b, B.4c, B.4d, B.5b, B.5c and B.5d) and in case of 4000 it was 1 pixel ≈ 0.064 μm (Figs. B.1e, B.1f, B.1g, B.2e, B.2f, B.2g, B.3e, B.3f, B.3g, B.4e, B.4f, B.4g, B.5e, B.5f and B.5g).

3.4 Automatic Detection of Fibers in SEM Images

An algorithm was proposed with the aim to detect fiber areas in images of unidirectional long–fiber composite cross–section (Fig. B.1 – B.5). An application for Ground Truth data (GT) and two algorithms for automatic fiber detection were built with cooperation with Ing. Lukáš Bureš and Ing. Ivan Pirner from the Department of Cybernetics using a library of programming functions which is aimed at real-time computer vision – *OpenCV* (Open Source Computer Vision). The codes were written in *Python*.

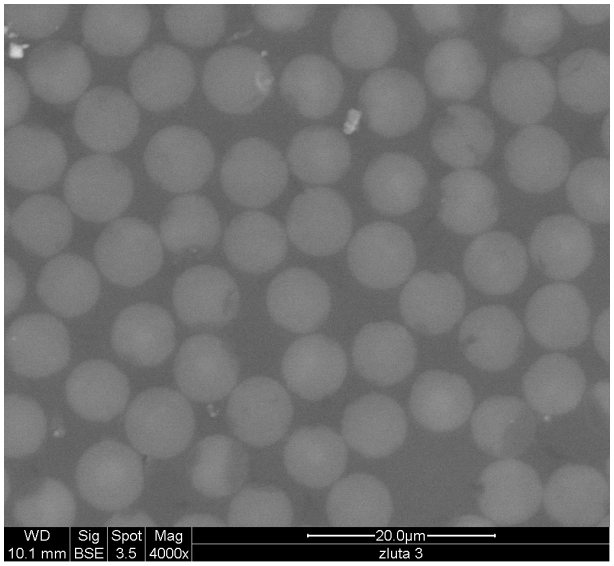

Figure 3.3: Monochromatic image of composite cross-section with magnification of 4000.

3.4.1 Image Preprocessing

The principle of proposed algorithms is shown for image (Fig. 3.3). Matrix $\mathbf{X}(m \times n)$ of integer pixel intensities (with a number of possible intensity values L) represents the monochromatic image.

$\mathbf{X}$ was blurred by discrete convolution with kernel $K_{i,j} = \frac{1}{p^2}$, where $i, j = 1, ..., p$,

$$X_{k,l}^{\mathrm{DC}} = \sum_{i=-p}^{p} \sum_{j=-p}^{p} K_{i,j} X_{k-i,l-j}, \tag{3.2}$$

which causes that an element of the resulting image $\mathbf{X}^{\mathrm{DC}}$ (Fig. 3.4a) has intensity value equal to the average value of its neighbouring pixels in the input image [48, 49].

Contrast of the image was adjusted and fiber edges enhanced by contrast limited adaptive histogram equalization (CLAHE). It computes several histograms, each corresponding to a distinct section of the image $\mathbf{X}^{\mathrm{DCsub}}(m_{\mathrm{sub}} \times n_{\mathrm{sub}})$ and limits the amplification (contrast) by redistributing part of the histogram exceeding certain value γ equally among all histogram bins [50]. The equalized image section elements are defined as

$$X_{i,j}^{\mathrm{CLAHEsub}} = \mathrm{floor}\left((L-1) \sum_{n=0}^{\mathrm{X}_{i,j}^{\mathrm{DCsub}}} p_{\gamma} \right), \tag{3.3}$$

where function floor() rounds down to the nearest integer and p_{γ} is the normalized histogram of $\mathbf{X}^{\mathrm{DCsub}}$ with a bin for each possible intensity

$$p_{\gamma} = \frac{\text{number of pixels with intensity } \alpha}{\text{total number of pixels}}, \tag{3.4}$$

where $\alpha = 0...L-1$ [51]. To ensure continuity between the subimages a bilinear interpolation is applied and matrix $\mathbf{X}^{\mathrm{CLAHE}}$ represents the equalized image (Fig. 3.4b).

The grayscale image $\mathbf{X}^{\mathrm{CLAHE}}$ was transformed to binary image $\mathbf{X}^{\mathrm{BIN}}$ (Fig. 3.4c) by Otsu's method, a clustering–based image thresholding. Otsu's algorithm assumes that the image contains foreground and background pixels and it calculates the optimum global threshold which separates pixels into the two classes [52].

3.4.2 Image Segmentation

Marker–based image segmentation was performed using watershed algorithm which views the grayscale image $\mathbf{X}^{\mathrm{CLAHE}}$ as a topographical surface, where high and low intensities denote peaks and valleys, respectively. Water with different label in every isolated valley rises until all peaks are under water. To avoid merging the water from different valleys, barriers are built in locations of merging and denote the segmentation result. Oversegmentation caused by noise is prevented by labelling different regions of the image before segmentation — the regions of background and foreground (all fiber areas separately) are labelled each with different integer and the remaining area is labelled with zero (Fig. 3.4d).

After applying the watershed algorithm markers of segmented image $\mathbf{X}^{\mathrm{WS}}$ have labels $X_{i,j}^{\mathrm{WS}} = -1$ for boundary regions and $X_{i,j}^{\mathrm{WS}} = s$, $s = 255, 254, ..., q$ for the number of segments q which represent the fibers in the image [48]. Each set of boundary points is represented by a list $\boldsymbol{\beta} = [\boldsymbol{\beta}_k]$, $k = 1, ..., t$ of t pairs of element positions in the matrix $\mathbf{X}^{\mathrm{WS}}$ (Fig. 3.4e).

3.4.3 RANSAC Algorithm

Two algorithms were applied on the preprocessed and segmented image $\mathbf{X}^{\mathrm{WS}}$. The first one is the iterative method RANSAC (RANdom SAmple Consensus) which is a learning technique to estimate parameters of a model by random sampling of data which can contain both, the so-called inliers (data whose distribution can be explained by some set of model parameters) and the so-called outliers (data that do not fit the model).

The proposed algorithm serves to approximate the points classified as boundary points of segments in $\mathbf{X}^{\mathrm{WS}}$ by circles (Fig. 3.5a) with a minimum of effect of the inaccurately classified points [53].

The algorithm consists of several iteratively repeated steps:

1. Randomly select 3 points from $\boldsymbol{\beta}$ and interpolate a circle containing these 3 points.
2. Test all other points of the input set.
   (a) Calculate the distance of all points from the circle.
   (b) Points closer to the circle than 5 pixels consider as inliers.
3. If the number of inliers is larger than in the best so far found model, save the new model.

4. If maximum number of iterations (given) is not exceeded and minimal number of inliers (given) is not identified, return to step 1.

5. Select the circle designated by the best model (Fig. 3.4f).

3.4.4 Least Squares Fitting Method

Least squares fitting method (LSQ) was the second algorithm applied. It was used to find the center positions of fibers in the preprocessed and segmented image $\mathbf{X}^{\mathrm{WS}}$ (Fig. 3.5b). The best fiber center position found by minimizing sum of squared residuals [54, 55]

$$S = \sum_{k=1}^{t} \left(\overline{\phi} - \phi\left(\boldsymbol{\beta}_k, \mathbf{c}\right)\right)^2, \tag{3.5}$$

where

$$\overline{\phi} = \frac{\sum_{k=1}^{t} \phi\left(\boldsymbol{\beta}_k, \mathbf{c}\right)}{t} \tag{3.6}$$

and $\phi\left(\boldsymbol{\beta}_k, \boldsymbol{c}\right)$ is the distance between fiber center position $\mathbf{c}$ and the k-th pixel in $\boldsymbol{\beta}$. When the fiber center position $\mathbf{c}_{\mathrm{id}}$ is identified, the fiber radius is obtained as

$$R_{\mathrm{f}} = \sum_{k=1}^{t} \frac{\phi\left(\boldsymbol{\beta}_k, \mathbf{c}_{\mathrm{id}}\right)}{t}. \tag{3.7}$$

3.4.5 Ground Truth Data

In the context of computer vision, ground truth data includes a set of images, and a set of labels on the images. The labels are added either by a human or automatically by image analysis, depending on the complexity of the problem. The collection of labels, such as interest points, corners, feature descriptors, shapes, and histograms, form a model or serve as validation of some method on a test set [56].

In this work the test set of images consists of nine monochromatic images of composite cross-section (Figs. B.3e, B.3f, B.3g, B.4e, B.4f, B.4g, B.5e, B.5f, B.5g), and the labels are fiber center positions and fiber radii.

The ground truth data were acquired in a proposed application, which enables the annotator to display the monochromatic image (Fig. 3.3) in three different modes – original, with improved contrast by adaptive histogram equalization, and in false color. At least three points on the boundary have to be marked and subsequently the center position $\mathbf{c}$ and radius of the fiber R_{f} are obtained by least square method.

3.4.6 Results of Fiber Detection Algorithms

The proposed methods, RANSAC and LSQ, were applied with parameters listed in Tab. 3.1 to estimate fiber center positions and radii in 9 images (Figs. B.2e, B.2f, B.2g, B.3e, B.3f, B.3g, B.4b, B.4c, B.4d). The results were compared with GT data in graphical

(Fig 3.5) and numerical terms (Tab. 3.2). Figs. 3.5a and 3.5b show the detected fibers by the proposed algorithms and the fibers from GT data. Figs. 3.5c, 3.5d and 3.5e depict the representation of the distribution of identified fiber radii.

Both proposed methods identify the searched radii of fibers R_f systematically smaller than the GT data, therefore the identified volume ratios V_f on a subimage (Figs. 3.5a, 3.5b) are smaller. The average fiber volume fraction over all identified cross-section images is smaller compared to GT data by 20.1% in case of LSQ method and 19.3% in case of RANSAC method data (Tab. 3.2). While the averaged fiber radii over all images are the same for both, LSQ and RANSAC methods, the difference in identified fiber volume fraction can be explained by more identified fibers in case of the RANSAC method. The two proposed methods for visual fiber detection applied on 9 images provide slightly different data. We can state that the RANSAC method provides better results than LSQ method compared to the GT data.

Table 3.1: Parameters of testing images and identification methods.

designation	unit	value	meaning
m	pixel	1024	image width
n	pixel	883	image height
L	–	256	no. of intensity values
p	pixel	5	kernel size
γ	–	40	CLAHE limit
m_sub, n_sub	pixel	8	image section size

Table 3.2: Identified image data.

image	GROUND TRUTH			LEAST SQUARE			RANSAC		
	V_f [%]	$\overline{R_\mathrm{f}}$ [μm]	Υ [–]	V_f [%]	$\overline{R_\mathrm{f}}$ [μm]	Υ [–]	V_f [%]	$\overline{R_\mathrm{f}}$ [μm]	Υ [–]
B.3e	68.4	3.39	16.71	57.2	3.32	17.40	56.9	3.33	16.03
B.3f	67.6	3.51	13.53	55.8	3.30	15.13	56.0	3.34	17.55
B.3g	71.7	3.45	15.88	60.8	3.31	16.23	61.2	3.30	15.73
B.4e	67.4	3.51	19.31	51.4	3.28	23.09	51.9	3.30	22.50
B.4f	67.0	3.56	22.69	50.3	3.34	22.94	51.2	3.25	24.06
B.4g	66.1	3.73	22.42	52.1	3.45	21.04	52.5	3.44	25.88
B.5e	70.7	3.48	12.53	54.4	3.26	15.46	55.1	3.29	14.80
B.5f	52.8	3.51	26.90	42.5	3.31	28.55	42.9	3.33	29.62
B.5g	64.2	3.49	18.00	51.8	3.25	19.18	52.7	3.24	21.33
mean values	66.2	3.51	18.66	52.9	3.31	19.89	53.4	3.31	20.83

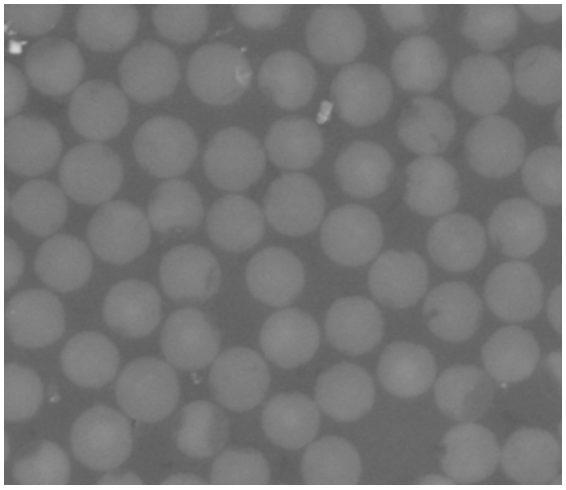

(a) Blurred image $\mathbf{X}^{\mathrm{DC}}$.

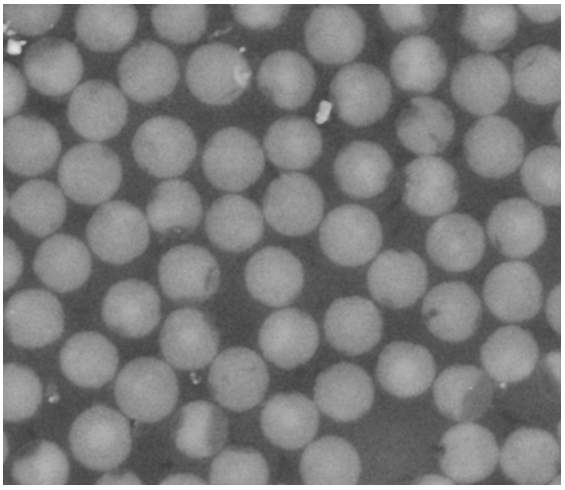

(b) Equalized image $\mathbf{X}^{\mathrm{CLAHE}}$.

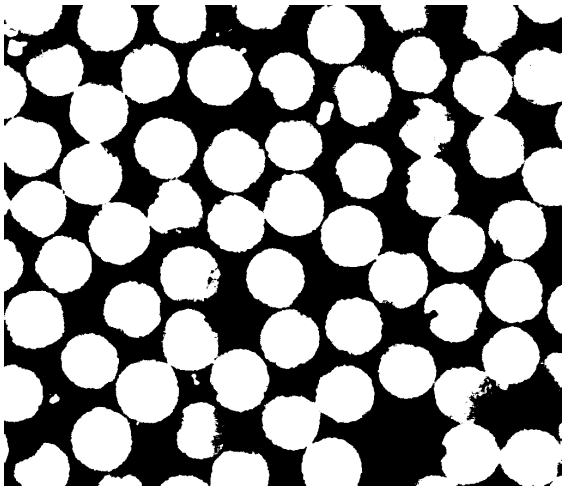

(c) Binary image $\mathbf{X}^{\mathrm{BIN}}$.

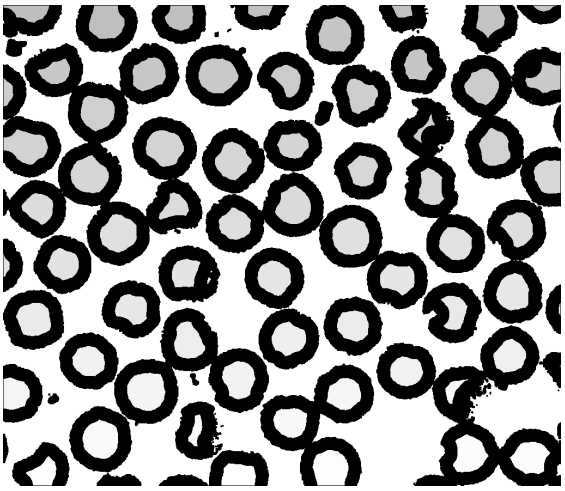

(d) Labelled image.

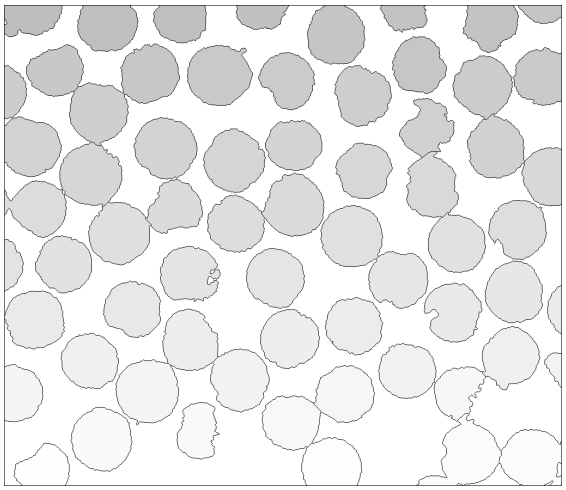

(e) Segmented image $\mathbf{X}^{\mathrm{WS}}$.

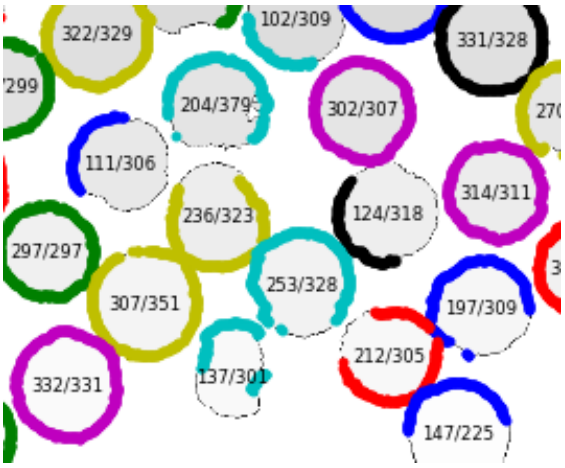

(f) Inliers/sets of points of a fiber boundary.

Figure 3.4: Images during processing by RANASAC algorithm.

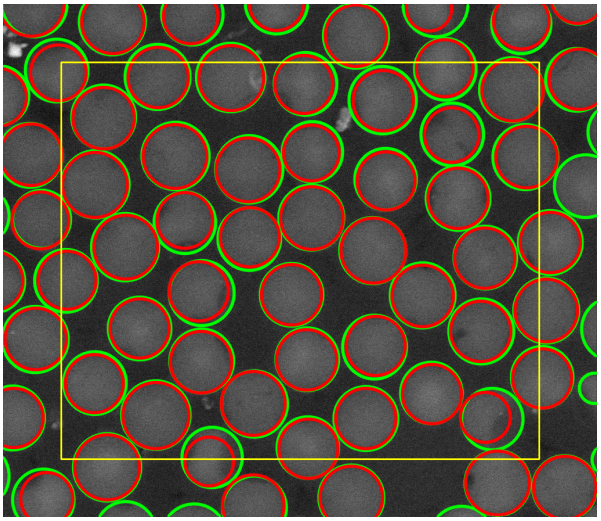

(a) Image with GT (green) and RANSAC detected (red) fibers and shrinked area (yellow).

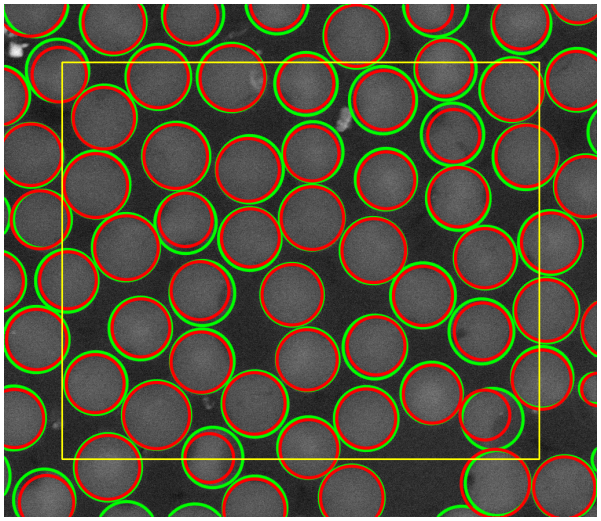

(b) Image with GT (green) and LSQ detected (red) fibers and shrinked area (yellow).

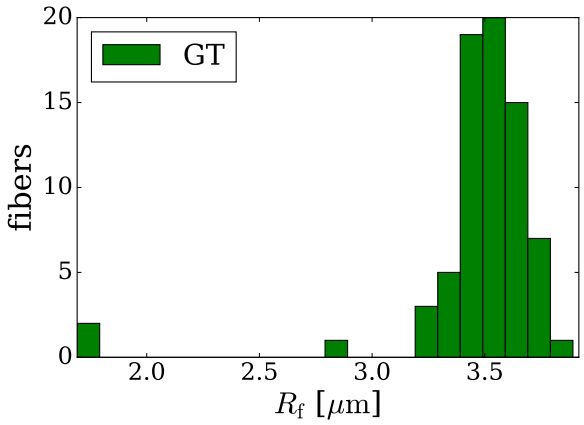

(c) Fiber radii histogram - GT data.

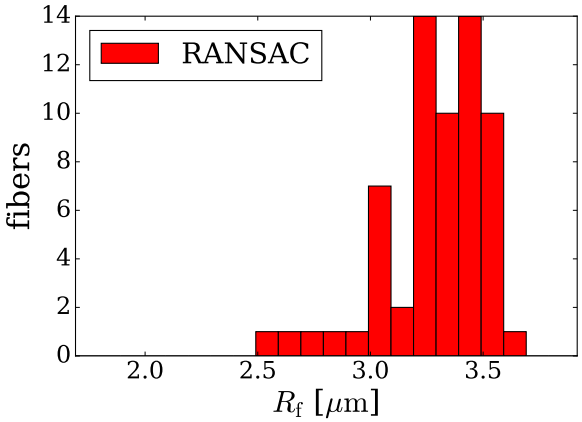

(d) Fiber radii histogram - RANSAC data.

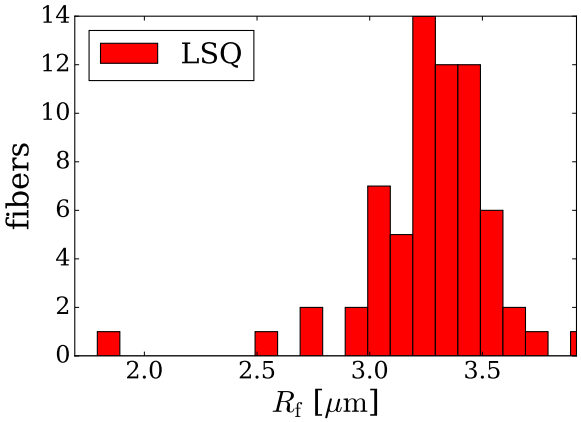

(e) Fiber radii histogram - LSQ data.

Figure 3.5: Results of RANSAC and LSQ fiber detection algorithms and GT data.

Chapter 4

Material Models

Before pursuing an approach to the micromechanics of the heterogeneous media such as the analyzed unidirectional long-fiber composite material, basic material behavior descriptions have to be introduced first. Material models used in the following work are described by the listed constitutive relationships. Even the basic relationships expressing material behavior have certain assumptions or boundaries of applicability. It is appropriate to state these limits to ensure full capability to model actual behavior.

4.1 Linear Elasticity

A homogeneous linear elastic continuum is considered in rectangular Cartesian coordinate system (123) which can also be written as $(x_1x_2x_3)$. Relationship between stress

$$\boldsymbol{\sigma}_{123} = \left[\sigma_{11}, \sigma_{22}, \sigma_{33}, \tau_{23}, \tau_{13}, \tau_{12}\right]^{\mathrm{T}} \tag{4.1}$$

and strain

$$\boldsymbol{\varepsilon}_{123} = \left[\varepsilon_{11}, \varepsilon_{22}, \varepsilon_{33}, \gamma_{23}, \gamma_{13}, \gamma_{12}\right]^{\mathrm{T}} \tag{4.2}$$

in such continuum is expressed by Hooke's law

$$\boldsymbol{\sigma}_{123} = \mathbf{C}\boldsymbol{\varepsilon}_{123}, \tag{4.3}$$

where $\mathbf{C}$ is symmetric stiffness matrix (6×6) (a fourth order tensor of elastic moduli, in general), σ_{ii} are normal components of of Cauchy stress tensor τ_{ij} are shear components of Cauchy stress tensor (Fig. 4.1), ε_{ii} are components of infenitisimal strain tensor and γ_{ij} are engineering shear strains.

In this case, the Cauchy stress is equivalent to second Piola-Kirchoff stress, which relates forces in reference configuration to areas in reference configuration [57].

The strain components can be derived from displacement u_i along given direction x_i

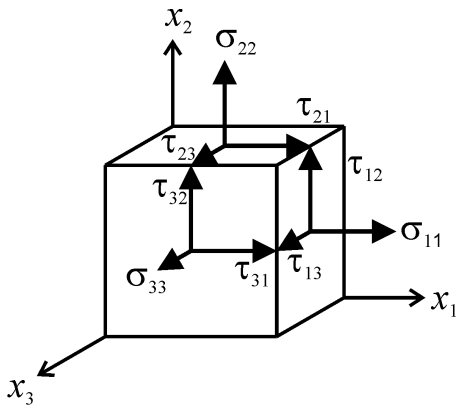

Figure 4.1: Stress cube showing all positive stress components.

defined as

$$\varepsilon_{11} = \frac{\partial u_1}{\partial x_1}, \tag{4.4}$$

$$\varepsilon_{22} = \frac{\partial u_2}{\partial x_2}, \tag{4.5}$$

$$\varepsilon_{33} = \frac{\partial u_3}{\partial x_3}, \tag{4.6}$$

$$\varepsilon_{23} = \frac{1}{2}\left(\frac{\partial u_2}{\partial x_3} + \frac{\partial u_3}{\partial x_2}\right), \tag{4.7}$$

$$\varepsilon_{13} = \frac{1}{2}\left(\frac{\partial u_1}{\partial x_3} + \frac{\partial u_3}{\partial x_1}\right), \tag{4.8}$$

$$\varepsilon_{12} = \frac{1}{2}\left(\frac{\partial u_1}{\partial x_2} + \frac{\partial u_2}{\partial x_1}\right) \tag{4.9}$$

and relations between engineering shears and shear components of strain tensor are

$$\gamma_{ij} = 2 \cdot \varepsilon_{ij}. \tag{4.10}$$

The generalized Hooke's law (4.3) can be expressed in an inverse form

$$\boldsymbol{\varepsilon}_{123} = \mathbf{S}\boldsymbol{\sigma}_{123}, \tag{4.11}$$

where $\mathbf{S}$ is a symmetric compliance matrix, which can be related to the stiffness matrix

$$\mathbf{S} = \mathbf{C}^{-1}. \tag{4.12}$$

4.1.1 Isotropic Material

Properties of isotropic material are identical in all directions. The compliance matrix has the same form in any Cartesian coordinate system

$$\mathbf{S} = \begin{bmatrix} \frac{1}{E} & -\frac{\nu}{E} & -\frac{\nu}{E} & 0 & 0 & 0 \\ -\frac{\nu}{E} & \frac{1}{E} & -\frac{\nu}{E} & 0 & 0 & 0 \\ -\frac{\nu}{E} & -\frac{\nu}{E} & \frac{1}{E} & 0 & 0 & 0 \\ 0 & 0 & 0 & \frac{2(1+\nu)}{E} & 0 & 0 \\ 0 & 0 & 0 & 0 & \frac{2(1+\nu)}{E} & 0 \\ 0 & 0 & 0 & 0 & 0 & \frac{2(1+\nu)}{E} \end{bmatrix}. \tag{4.13}$$

It is possible to express the material behavior by two independent parameters, for instance E and ν [58].

4.1.2 Transversely Isotropic Material

Transversely isotropic material has three planes of symmetry and one of them is also the plane of isotropy (same elastic parameters in all directions). If the plane of isotropy is plane (23), then the main direction of anisotropy is identical to axis x_1 and the compliance matrix is

$$\mathbf{S} = \begin{bmatrix} \frac{1}{E_{11}} & -\frac{\nu_{21}}{E_{22}} & -\frac{\nu_{21}}{E_{22}} & 0 & 0 & 0 \\ -\frac{\nu_{12}}{E_{11}} & \frac{1}{E_{22}} & -\frac{\nu_{32}}{E_{33}} & 0 & 0 & 0 \\ -\frac{\nu_{13}}{E_{11}} & -\frac{\nu_{23}}{E_{22}} & \frac{1}{E_{33}} & 0 & 0 & 0 \\ 0 & 0 & 0 & \frac{1}{G_{23}} & 0 & 0 \\ 0 & 0 & 0 & 0 & \frac{1}{G_{13}} & 0 \\ 0 & 0 & 0 & 0 & 0 & \frac{1}{G_{12}} \end{bmatrix}, \tag{4.14}$$

where for the Young's moduli are $E_{22} = E_{33}$, shear moduli are $G_{12} = G_{13}$, and Poisson's ratios are $\nu_{12} = \nu_{13}$, $\nu_{23} = \nu_{32}$ and

$$G_{23} = \frac{E_{22}}{2(1+\nu_{23})}. \tag{4.15}$$

The transversely isotropic material can be expressed by 5 independent material constants E_{11}, E_{22}, G_{12}, ν_{12} a ν_{23} [58].

4.1.3 Anisotropic Material

In case of an anisotropic material, there is no plane of symmetry of elastic properties and the compliance matrix [59] has 21 independent elements

$$\mathbf{S} = \begin{bmatrix} \frac{1}{E_{11}} & -\frac{\nu_{21}}{E_{22}} & -\frac{\nu_{31}}{E_{33}} & \frac{\eta_{1,23}}{G_{23}} & \frac{\eta_{1,13}}{G_{13}} & \frac{\eta_{1,12}}{G_{12}} \\ -\frac{\nu_{12}}{E_{11}} & \frac{1}{E_{22}} & -\frac{\nu_{32}}{E_{33}} & \frac{\eta_{2,23}}{G_{23}} & \frac{\eta_{2,13}}{G_{13}} & \frac{\eta_{2,12}}{G_{12}} \\ -\frac{\nu_{13}}{E_{11}} & -\frac{\nu_{23}}{E_{22}} & \frac{1}{E_{33}} & \frac{\eta_{3,23}}{G_{23}} & \frac{\eta_{3,13}}{G_{13}} & \frac{\eta_{3,12}}{G_{12}} \\ \frac{\eta_{23,1}}{E_{11}} & \frac{\eta_{23,2}}{E_{22}} & \frac{\eta_{23,3}}{E_{33}} & \frac{1}{G_{23}} & \frac{\mu_{23,13}}{G_{13}} & \frac{\mu_{23,12}}{G_{12}} \\ \frac{\eta_{13,1}}{E_{11}} & \frac{\eta_{13,2}}{E_{22}} & \frac{\eta_{13,3}}{E_{33}} & \frac{\mu_{13,23}}{G_{23}} & \frac{1}{G_{13}} & \frac{\mu_{13,12}}{G_{12}} \\ \frac{\eta_{12,1}}{E_{11}} & \frac{\eta_{12,2}}{E_{22}} & \frac{\eta_{12,3}}{E_{33}} & \frac{\mu_{12,23}}{G_{23}} & \frac{\mu_{12,13}}{G_{13}} & \frac{1}{G_{12}} \end{bmatrix}, \tag{4.16}$$

where $\eta_{k,ij}$ are coefficients of mutual influence of the first kind

$$\eta_{k,ij} = \frac{\varepsilon_{kk}}{\gamma_{ij}}, \tag{4.17}$$

$\eta_{kl,i}$ are coefficients of mutual influence of the second kind

$$\eta_{kl,i} = \frac{\gamma_{kl}}{\varepsilon_{ii}} \tag{4.18}$$

and $\mu_{kl,ij}$ are Chentsov's coefficients

$$\mu_{kl,ij} = \frac{\gamma_{kl}}{\gamma_{ij}}. \tag{4.19}$$

4.2 Nonlinear Elasticity

Nonlinear elastic material is a material whose stress-strain dependency is not linear and there is no permanent deformation after unloading. The stress-strain curve for 1D example is identical for both, the loading and the unloading process (Fig. 4.2).

Helmholz free energy per unit mass is a thermodynamic potential that measures work obtainable from a closed thermodynamic system at a constant temperature and can have a form

$$\Psi = \frac{1}{\rho}\left(\frac{E_{11}^0 \varepsilon_{11}^2}{2} + \frac{E_{11}^0 g \varepsilon_{11}^3}{6}\right), \tag{4.20}$$

where E_{11}^0 is initial Young's modulus and g is a shape parameter and ρ is density.

Stress can be expressed from (4.20) as

$$\sigma_{11} = \rho \frac{\partial \Psi}{\partial \varepsilon_{11}} = E_{11}^0 \varepsilon_{11} + \frac{E_{11}^0 g \varepsilon_{11}^2}{2} \tag{4.21}$$

and Young's modulus as

$$E_{11} = \frac{\partial \sigma_{11}}{\partial \varepsilon_{11}} = E_{11}^0 + E_{11}^0 g \varepsilon_{11}. \tag{4.22}$$

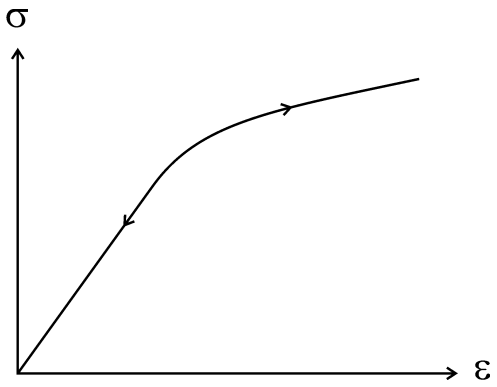

Figure 4.2: Stress-strain dependency of 1D material with nonlinear elastic behavior.

Young's modulus (4.22) expressed as a function of strain component

$$E_{11}\left(\varepsilon_{11}\right) = E_{11}^{0}\left(1 + g\varepsilon_{11}\right) \tag{4.23}$$

is used in this work for characterization of nonlinear elastic behavior of fibers.

4.3 Plasticity

Theory of plasticity concerns materials, which after being subjected to a loading, exhibit permanent (or plastic) deformations when completely unloaded. The short summary of theory below is restricted to description of materials for which the permanent deformations do not depend on the strain rate [60, 61]. Materials whose behavior can be described by the theory of plasticity are called plastic materials.

Stress-strain curve of 1D elastoplastic material with linear elastic behavior loaded by pure tension is in Fig. 4.3. In the phase of loading, where so-called equivalent stress is smaller than initial yield stress σ_{y}^{0}, the behavior is linear elastic and given by the uniaxial elastic law

$$\boldsymbol{\sigma} = \mathbf{C}\boldsymbol{\varepsilon}_{\mathrm{e}}, \tag{4.24}$$

where $\boldsymbol{\varepsilon}_{\mathrm{e}}$ is the reached elastic strain. If the material is unloaded before reaching the yield stress, it returns to the original state.

At σ_{y}^{0} the slope of the stress-strain curve changes, plastic yielding (evolution of plastic strain $\boldsymbol{\varepsilon}_{\mathrm{p}}$) is given by a function of equivalent plastic strain and strain is a sum of elastic and plastic (permanent) part

$$\boldsymbol{\varepsilon} = \boldsymbol{\varepsilon}_{\mathrm{e}} + \boldsymbol{\varepsilon}_{\mathrm{p}}. \tag{4.25}$$

After exceeding the value of σ_{y}^{0}, yield stress is changing (hardening in case of Fig. 4.3). After unloading, permanent plastic strain remains (the unstressed state differs from the initial unstressed state).

Behavior of the unloading and reloading process, where $\boldsymbol{\sigma} \in \langle 0;\ \sigma_{\mathrm{y}} \rangle$, is considered to be linear elastic. Reloading from the unstressed state has a constant plastic strain until

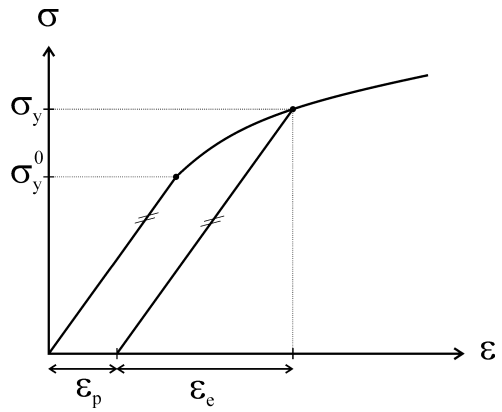

Figure 4.3: Stress-strain dependency for 1D material with plastic behavior.

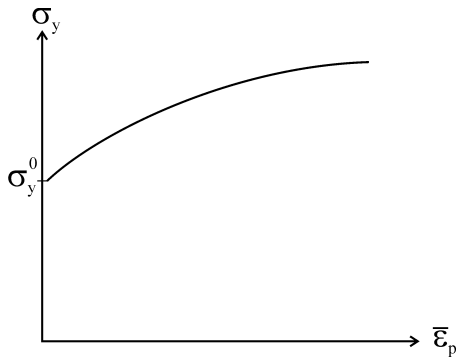

Figure 4.4: Hardening curve defined by hardening function.

reaching the new (current) yield limit σ_{y}. With every exceeding of the current yield stress σ_{y}, the equivalent plastic strain $\overline{\varepsilon}_{\mathrm{p}}$ grows.

Elastic domain at a state with yield stress σ_{y} with yield function

$$\Phi\left(\boldsymbol{\sigma}, \sigma_{\mathrm{y}}\right) = \sigma_{\mathrm{red}} - \sigma_{\mathrm{y}} \leq 0, \tag{4.26}$$

where σ_{red} is equivalent stress, is the yield criterion in general form. Plastic flow is present when (4.26) is not satisfied and it is necessary find another physically admissible state when $\Phi = 0$. That means identifying a new combination of $\overline{\varepsilon}_{\mathrm{p}}$, ε_{p} and ε_{e}.

Evolution of the yield stress hardening is accompanied by the evolution of the equivalent plastic strain. Hardening law describes this phenomenon. Yield stress is given by a function

$$\sigma_{\mathrm{y}} = \sigma_{\mathrm{y}}\left(\overline{\varepsilon}_{\mathrm{p}}\right). \tag{4.27}$$

Hardening function (4.27) defines a hardening curve (Fig. 4.4).

4.3.1 Von Mises Yield Criterion

The yield criteria in general form (4.26) describing plastic yielding is given by a certain yield criteria, i.e. for isotropic materials Tresca, von Mises, Mohr-Coulomb and Drucker-

Prager.

According to von Mises yield criterion [62], plastic yielding begins when equivalent stress σ_{red} reaches the yield stress σ_{y}, which denotes the limit of elastic behavior and the start of plastic deformation. The equivalent stress σ_{red} is defined in terms of principal stress components σ_1, σ_2 and σ_3 as

$$\sigma_{\mathrm{red}} = \sqrt{\frac{(\sigma_1 - \sigma_2)^2 + (\sigma_2 - \sigma_3)^2 + (\sigma_3 - \sigma_1)^2}{2}}. \tag{4.28}$$

4.3.2 Isotropic Hardening

Isotropic hardening is a type of evolution of the yield surface in coordinate system of the principal stress components ($\sigma_1\sigma_2\sigma_3$), a uniform (isotropic) expansion of the initial yield surface with no translation.

For multiaxial plasticity model with von Mises yield surface, isotropic hardening corresponds to the increase in radius of the von Mises cylinder in principal stress space (Fig. 4.5).

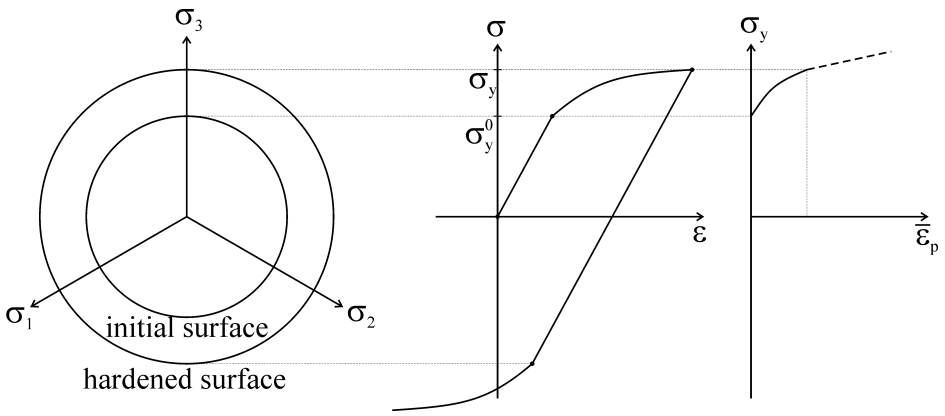

Figure 4.5: Example of isotropic hardening, stress-strain dependency for 1D material and hardening curve.

A work hardening function was proposed for purposes of capturing plastic behavior of epoxy resin, which was subjected to experimental tensile tests (Appendix C). The tensile tests were performed in order to obtain response of a separate composite phase (matrix) to mechanical loading. The work hardening function has form

$$\sigma_{\mathrm{y}} = \sigma_{\mathrm{y}}^0 + \frac{P_E \overline{\varepsilon}_{\mathrm{p}}}{\left(1 + \left(\frac{P_E \overline{\varepsilon}_{\mathrm{p}}}{P_A + P_K \overline{\varepsilon}_{\mathrm{p}}}\right)^n\right)^{\frac{1}{n}}}, \tag{4.29}$$

where P_E, P_A, P_K and n are material shape parameters.

Chapter 5

Micromodel

Micromodel of a composite material is used to simulate material behavior on a microscale level, where material parameters of individual phases and their distribution are taken into account. Micromodel in this work was built in *Abaqus/CAE* and it was used to identify parameters of material models of fibers and matrix according to data obtained from simple tensile tests and to analyze influence of fiber spatial distribution in composite cross-section e.g. on homogenized material properties.

The micromodel is used to simulate response in a specific place of the structure when the load is known or to calculate homogenized material properties. Advantage of a micromodel is its ability to describe effects of a loading state on the microscale level. It is also possible to include the influence of inclusions or defects (failures, voids, etc.) on the microscopic level.

The unidirectional longfiber composite can be considered as an heterogeneous material with a periodically repeated microstructure. The smallest volume that is repeated in the structure is usually called representative volume element (RVE) or unit cell (UC). The representative volume element is used to create the micromodel geometry in finite element software.

5.1 Micromodel Analysis Description

Several analyses were performed on the micromodel built in finite element software *Abaqus/CAE*. First, material parameters of two combinations of material models (linear elastic models for fibers and matrix or nonlinear elastic model for fibers and elaastoplastic model for matrix) of the phases (fibers and matrix) of micromodel with regular structure were identified in optimization process performed in *optiSLang*. Combination of material parameters of phases providing the best matching response to loading compared with the experiments performed in section 2.2 was identified.

When the material parameters of the proposed material models of the micromodel with regular structure were found, homogenized material properties of regular and different number of irregular micromodels with different degrees of irregularity were calculated.

Analysis of influence of the geometrical irregularity has been performed on the proposed micromodel by calculating the homogenized linear elastic material parameters for different geometries of the unit cells. Influence of deviation of the material parameters of phases on the homogenized properties of the micromodel was analyzed. Homogenized properties of unit cells with regular fiber distribution were calculated for material parameters of the phases differing from the values obtained using optimization process by up to 10 %. Each parameter was separately variated from values obtained by micromodel calibration to the experimental data.

Stress-strain dependencies corresponding to experimental tensile tests were calculated for a micromodel with proposed nonlinear elastic material model of fibers and elastoplastic material model of matrix. The stress/strain dependencies obtained from micromodel with regular fiber distribution were compared to the dependencies given by the experimental tensile tests.

Influence of deviation of material parameters of the micromodel with nonlinear material models on the micromodel response was analyzed. Stress/strain dependencies were calculated for micromodels with material parameters of the phases differing from the values obtained using identification process by up to 10 % to evaluate the influence of individual parameters change on the response of the micromodel to loadings defined by experimental tensile tests. The material parameters were variated from the calibrated values one at a time.

The process of the finite element analysis on the proposed micromodel is described in Fig. 5.1.

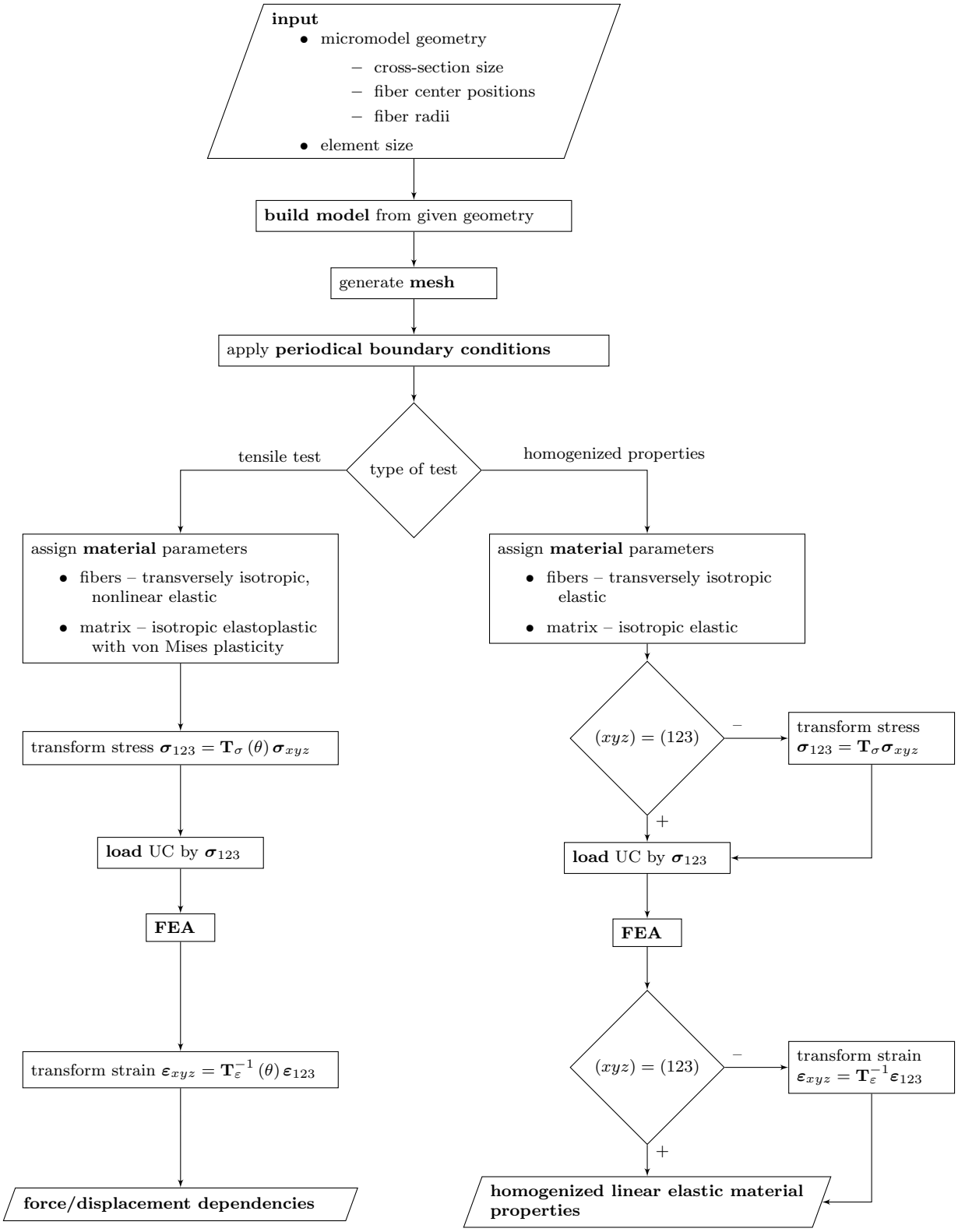

Figure 5.1: Flowchart of algorithm for computing homogenized material properties and obtaining force/displacement dependencies of given material.

5.2 Cross-section

Different cross-section geometries of a micromodel with ideally circular fibers with same fiber radii R_f and volume ratio V_f were proposed. All proposed geometries respect periodicity, which ensures the possibility to repeat the volume element in all directions (1, 2 and 3) even in deformed state.

The fiber volume ratio has been chosen with respect to results of the analysis of the real composite cross-section. In section 3.4.6, the mean fiber volume ratio given by ground truth data is $V_f = 66$ % (fibers and their radii were identified manually, and the data are considered as reliable). Image processing algorithm proposed in [1] identified the fiber volume fraction as $V_f = 58$ % and [2] as $V_f = 62$ %.

The fiber volume ratio for the unit cells was chosen $V_f = 60$ %. The higher fiber volume fraction resulting from the image processing has been determined on images in central areas of laminae. Areas at boundaries of the laminae have visibly smaller volume ratios as in Fig. 5.2, where the fiber volume ratio given by GT data is $V_f = 43$ %. Fiber radii was set as $R_f = 0.5$ for all geometries. The value has no unit, while the problem is scalable and the fiber diameter $2R_f = 1$ is a convenient reference value.

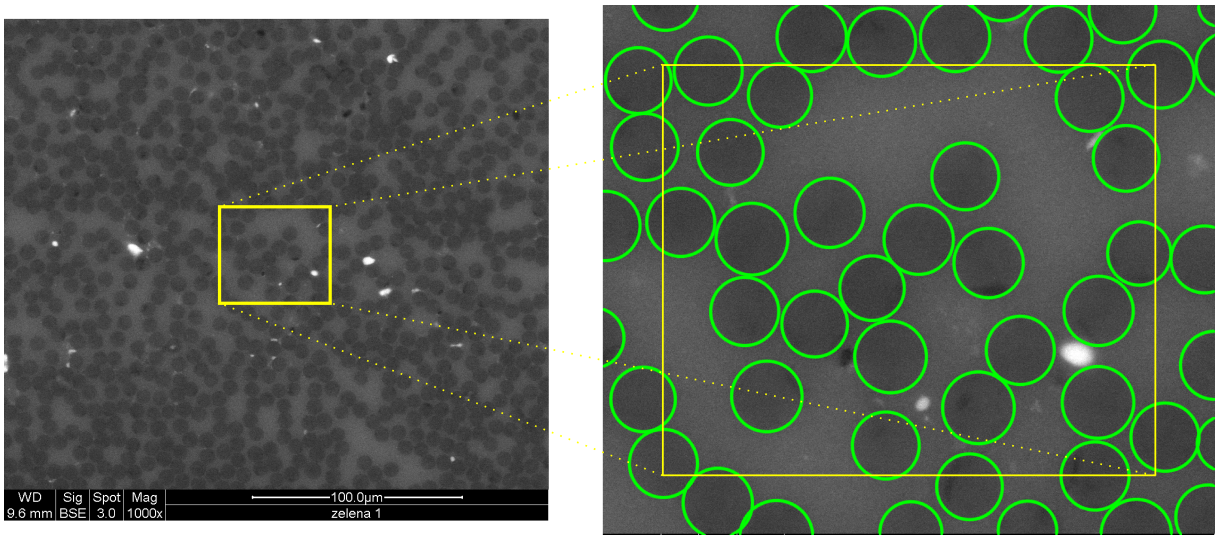

Figure 5.2: Images of composite cross-section with detected fibers in the inter-lamina area.

5.2.1 Unit Cell with Regular Fiber Distribution

Two possible approximations of fiber distribution in two-phase composite material can be used, square and hexagonal pattern (Fig. 5.3). In this work, for the regular fiber distribution approximation, hexagonal geometry was chosen. The SEM images of the composite cross-section (Figs. B.1, B.2, B.3, B.4, B.5) show that the fiber distribution has stronger resemblance to the hexagonal rather than to the square pattern (Fig. 5.4 - right). The smallest representative volume element for hexagonal fiber distribution with

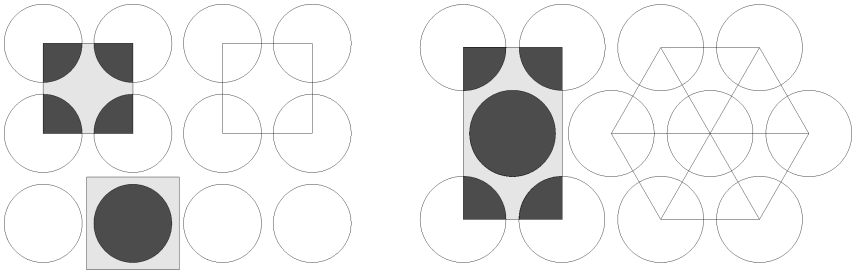

Figure 5.3: Square (left) and hexagonal (right) fiber distributions with unit cells.

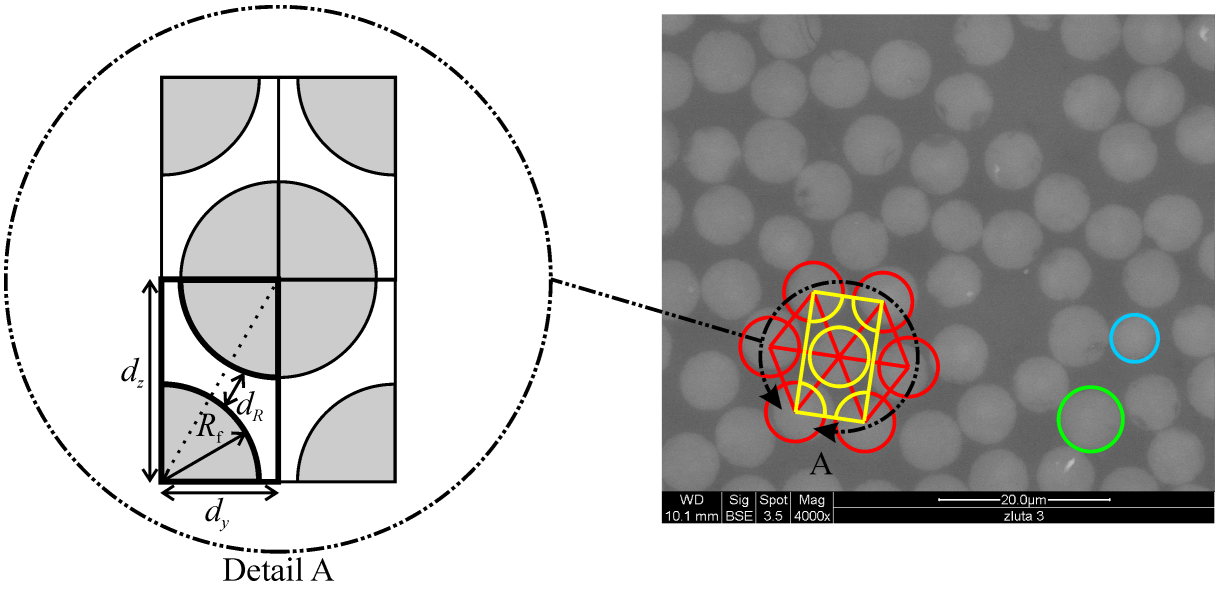

Figure 5.4: Image of composite cross-section with magnification of 4000 and a basic unit cell (yellow) used for hexagonal fiber distribution approximation and the smallest (blue) and largest (green) fiber.

periodical structure, which can be repeated along the directions of the cartesian coordinate system axes 1, 2 and 3 is a basic unit cell and has dimensions $2 \cdot d_y \times 2 \cdot d_z$ (Fig. 5.4 – left).

In the cross-section of unit cell with regular fiber distribution, fiber centers are positioned according to hexagonal (honeycomb) distribution (Fig. 5.3). The unit cell height and width of the rectangular basic element of unit cell (Fig. 5.4) respects the aspect ratio

$$d_z = \sqrt{3} \cdot d_y \tag{5.1}$$

and it can be shown that

$$V_\mathrm{f} = \frac{\pi \cdot R_\mathrm{f}^2}{2 \cdot d_y \cdot d_z}. \tag{5.2}$$

Unit cell with regular fiber distribution represents the ideal regularity, therefore the parameter expressing the degree of irregularity is $\Upsilon = 0$. Geometry with area of 56 fibers laying inside the cell area was proposed, twelve fibers are duplicated to ensure the

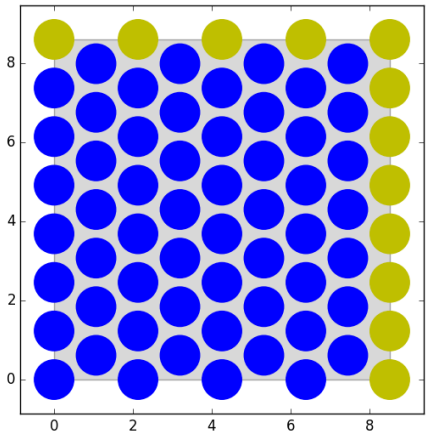

Figure 5.5: Geometry of regular unit cell with 56 fibers (blue) and 12 repeated (yellow) fibers.

periodicity of the unit cell. The unit cell was formed by repeating an elementary cell (Fig. 5.4). Dimensions of the regular unit cell $b \times c = 8d_z \times 14d_y$ were chosen to obtain an area with side ratio $8\sqrt{3} : 14 = 1 : 0.99$ as similar to square as possible while having similar number of fibers as in SEM images with magnification of 4000. Using (5.2), parameters of the unit cell respect relationship

$$V_\mathrm{f} = \frac{56 \cdot \pi \cdot R_\mathrm{f}^2}{14d_y \cdot 8d_z}. \tag{5.3}$$

5.2.2 Unit Cells with Irregular Fiber Distribution

Geometries of all irregular unit cells were proposed with the same fiber volume fraction $V_f = 60$ % and volume radii $R_f = 0.5$ (same as the unit cell with regular fiber distribution above). There are 56 fibers in all unit cells, only the number of duplicated fibers (due to periodicity of the geometry) varies.

Clustered Unit Cell

To obtain an extremely irregular fiber distribution in a unit cell a so-called clustered unit cell was proposed. The clustered unit cell (Fig. 5.6) with 56 fibers fully inside the cell was proposed by decreasing the fiber distance to $d_R = \frac{2\pi R_f}{360}$ (Fig. 5.4) in regular unit cell (Fig. 5.5). A nonzero fiber distance is desired to avoid problems with meshing [1] in real material, however, the fibers can touch. A geometry with no fibers overlapping the unit cell area and with border areas without fibers was attained (Fig. 5.6). The aspect ratio of regular unit cell sides $b \times c = 8 \cdot dz \times 14 \cdot dy$ is respected and the resulting degree of irregularity $\Upsilon = 61.69$.

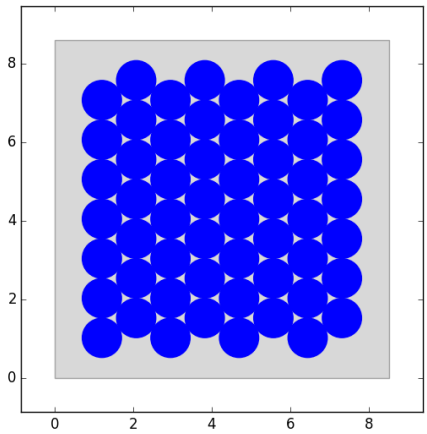

Figure 5.6: Geometry of clustered unit cell.

Unit Cell with Stripe of Fibers

Another example of a unit cell imitating an extremely irregular fiber distribution is a unit cell with stripe of fibers. A unit cell with 56 fibers, where 4 of them are overlapping the geometry area was proposed (Fig. 5.7) by enlarging the width of the regular unit cell (Fig 5.5) and rearranging a horizontal row of fibers. The unit cell has areas without fibers along two opposing sides. The distance between neighbouring fibers is $d_R = \frac{2\pi R_f}{360}$ and the resulting degree of irregularity is $\Upsilon = 66.94$.

[1] Fibers should not be connected.

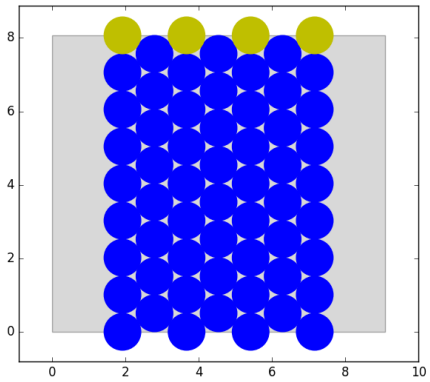

Figure 5.7: Geometry of unit cell with fibers arranged in a stripe.

Unit Cells with Random Fiber Distribution

The unit cell with random distribution of fibers was built in *Python* by an algorithm for simulating chaotically colliding billiard balls in 2D [63]. The algorithm was created by Ing. Vladimír Lukeš Ph.D. at the Department of Mechanics of University of West Bohemia in Pilsen for [3] and augmented by author for purposes of the proposed dissertation. Each circle (fiber in this case) moves along a straight line until it collides with another component. Collisions are processed in a non-decreasing order of time. The defined fiber volume fraction is ensured by termination criterion in the iterative process. Periodicity of the volume element is ensured by a component disappearing at a boundary and reappearing at the opposite side (Fig. 5.8). Principle of the algorithm for generating unit cells with random fiber distribution is depicted in Fig. 5.9.

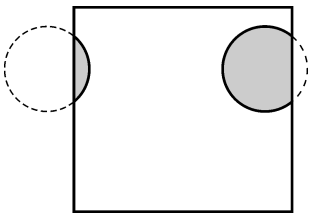

Figure 5.8: Parts of fiber on the area boundaries in accordance with periodic boundary conditions.

One hundred geometries having area $14d_y \times 8d_z$ were produced by the proposed algorithm (example in Fig. 5.10). Minimum fiber distance $d_R = \frac{2\pi R_f}{360}$ was used to avoid problems with meshing of the geometry (low-quality mesh). The cells were produced with different alternations to obtain geometries spread in interval of degree of irregularity $\Upsilon \in \langle 0;\ 66.94 \rangle$ including the geometries with regular fiber distribution

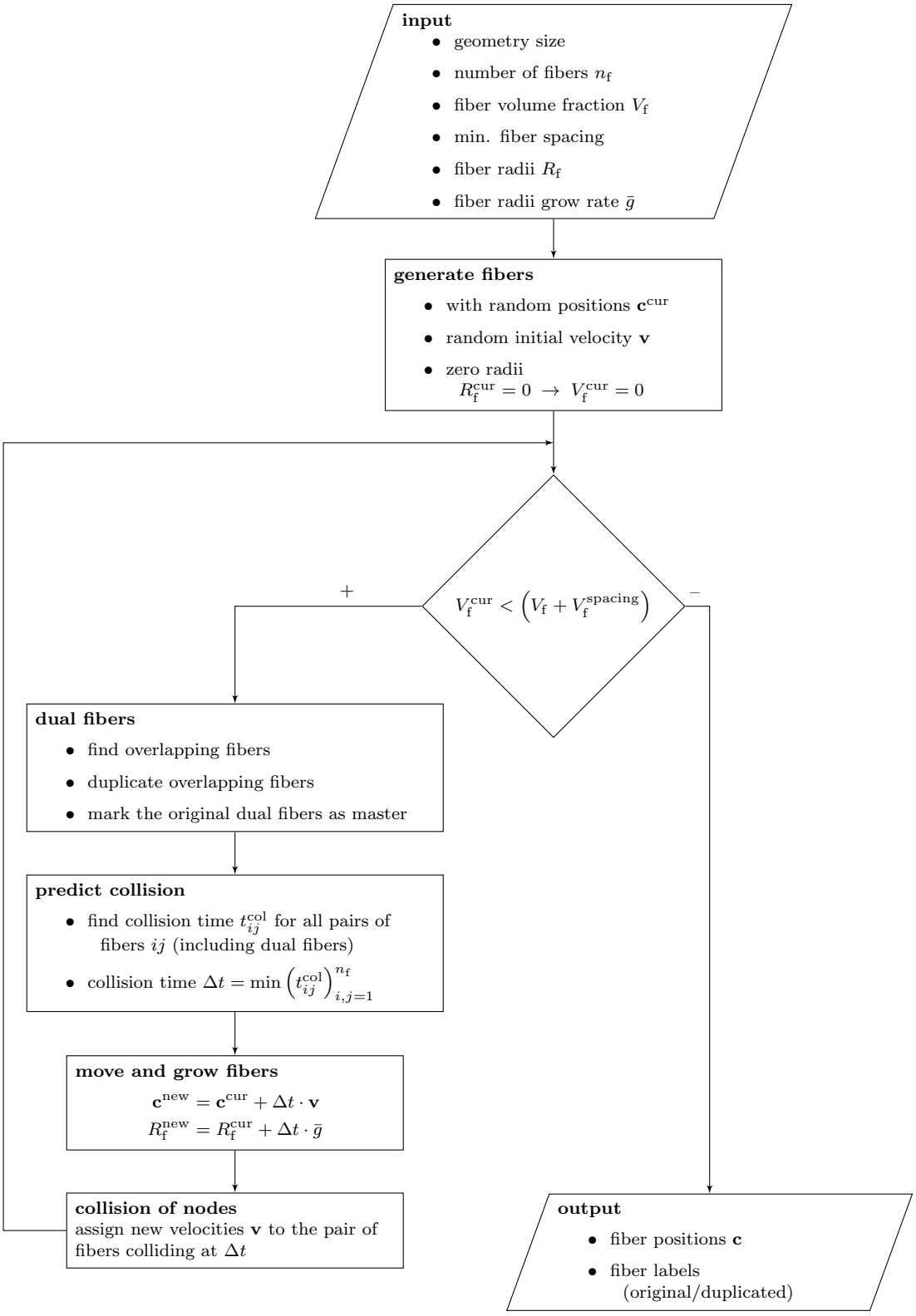

Figure 5.9: Flowchart of algorithm for generating unit cell geometry.

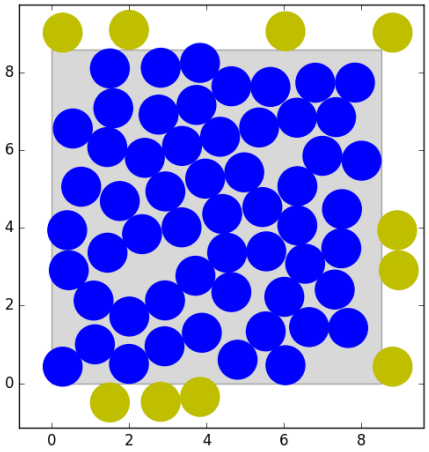

Figure 5.10: Geometry of a unit cell with random fiber distibution - 56 fibers (blue), 10 duplicated fibers (yellow).

5.3 Mesh

Micromodels consisted of one layer of linear hexahedral elements (type C3D8), and linear wedge elements (type C3D6). The number of hexahedral-shaped elements is dominating. To ensure periodicity, the opposite surfaces have identical surface meshes. Volume of the unit cell is $a \times b \times c$, where a is the thickness, b is the width and c is the height.

The micromodel was created by an automatic meshing of the 2D geometry of the cross-section of the unit cell and then by expanding along the direction of fibers by using bottom-up meshing technique [64].

Edges of the unit cell and fiber/matrix edges were seeded with a seed length l^{seed}. Seed length defines the approximate resulting element size of the mesh.

Thickness of the micromodel was set equal to the seed length $a = l^{\text{seed}}$ to ensure elements with shape as close to cube as possible. Therefore thicknesses of all unit cells is equal to the element size of built micromodel, while it consists of one layer of elements.

5.4 Periodic Boundary Conditions

The unit cell represents the repeated part of the periodic material (or structure). It means that any physical quantity $\mathcal{F}$ such as material properties (density, Young's moduli, Poisson's ratios, shear moduli and other elasticity constants etc.) or state variables (displacement vectors, stress and strain tensors, etc.) must be periodic functions of the spatial coordinates. Therefore, for unit cell having the shape of rectangular cuboid, we can write

$$\mathcal{F}(\mathbf{x}_{123}) = \mathcal{F}(\mathbf{x}_{123} + \mathbf{N}\,[\mathbf{a}, \mathbf{b}, \mathbf{c}]^{\mathrm{T}}), \tag{5.4}$$

where $\mathbf{x}_{123} = [x_1, x_2, x_3]^{\mathrm{T}}$ are point coordinates, $\mathbf{N}$ is a diagonal matrix 3×3

$$\mathbf{N} = \begin{bmatrix} n_1 & 0 & 0 \\ 0 & n_2 & 0 \\ 0 & 0 & n_3 \end{bmatrix} \tag{5.5}$$

with arbitrary integer values n_1, n_2 and n_3 on the diagonal and $[a, b, c]^{\mathrm{T}}$ is a constant vector of unit cell dimensions.

In order to ensure its periodicity even after deformation (after applying loads) the relative motion (displacements) of all pairs of corresponding nodes on opposite sides (of the unit cell) must be constant. In case of three-dimensional finite element analysis with elements having only displacement degrees of freedom (i.e. no rotations) the following three categories of constraints must be prescribed – namely the constraints for

- nodes on the surface but not on the edges or at corners,
- nodes on the edges but not at corner, and
- nodes at the corners.

The mesh has to be periodic as well, i.e., the opposite sides must be discretized with equal surface (2D) mesh.

The first category of constraints can be written for each pair of corresponding nodes (Fig. 5.11) A and B (on the two sides perpendicular to axis 1) as a set of three equations

$$u_1^B - u_1^A = a \cdot \varepsilon_{11}, \tag{5.6}$$
$$u_2^B - u_2^A = a \cdot \varepsilon_{12} = a\frac{\gamma_{12}}{2}, \tag{5.7}$$
$$u_3^B - u_3^A = a \cdot \varepsilon_{13} = a\frac{\gamma_{13}}{2}. \tag{5.8}$$

The strain tensor and strain vector components (infinitesimal strain as defined in chapter 4) on the right-hand side represent the homogenized (or effective) strains of the material (unit cell). The equations can be obtained analogously for the latter two degrees of freedom, and for the two remaining pairs of opposite sides. All these equations are linearly independent.

The second category of constraints can be written for the first degree of freedom for all corresponding quaternions of nodes A, B, C and D (belonging to 4 mutually parallel edges) as

$$u_1^B - u_1^A = a \cdot \varepsilon_{11}, \tag{5.9}$$
$$u_1^C - u_1^D = a \cdot \varepsilon_{11}, \tag{5.10}$$
$$u_1^A - u_1^D = b \cdot \frac{\gamma_{12}}{2}, \tag{5.11}$$
$$u_1^B - u_1^C = b \cdot \frac{\gamma_{12}}{2}, \tag{5.12}$$

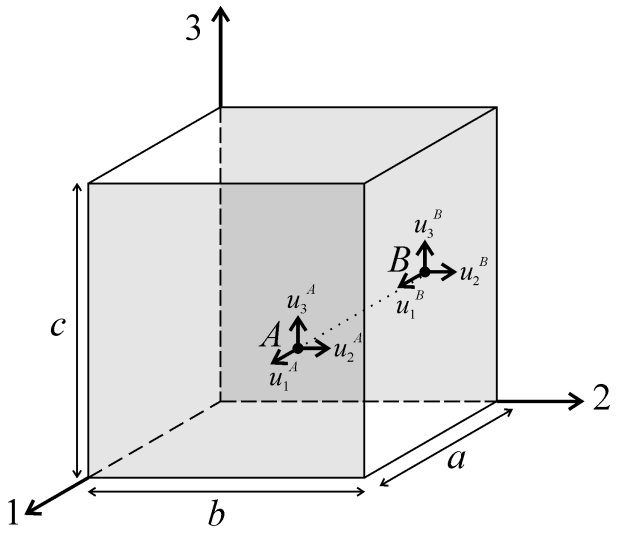

Figure 5.11: Representative volume element and nodes on opposite sides.

where a and b are dimensions of the unit cell along the two perpendicular edges (Fig. 5.12). These four equations, however, are not linearly independent. After rewriting the set of equation in matrix form

$$\begin{bmatrix} -1 & 1 & 0 & 0 \\ 0 & 0 & 1 & -1 \\ 1 & 0 & 0 & -1 \\ 0 & 1 & -1 & 0 \end{bmatrix} \cdot \begin{bmatrix} u_1^A \\ u_1^B \\ u_1^C \\ u_1^D \end{bmatrix} = \begin{bmatrix} a \cdot \varepsilon_{11} \\ a \cdot \varepsilon_{11} \\ b \cdot \frac{\gamma_{12}}{2} \\ b \cdot \frac{\gamma_{12}}{2} \end{bmatrix} . \tag{5.13}$$

it can be shown that the coefficient matrix is singular (matrix rank is three), and the system of 4 equations can be reduced (e.g. by Gauss elimination) to a system of 3 linearly independent equations (any subset of the original set, e.g. (5.10), (5.11) and (5.12)). The equations can be obtained and reduced analogously for the latter two degrees of freedom and for for the two remaining combinations of mutually parallel edges.

The third category of constraints can be written for all 8 corner nodes A, B, C, D,

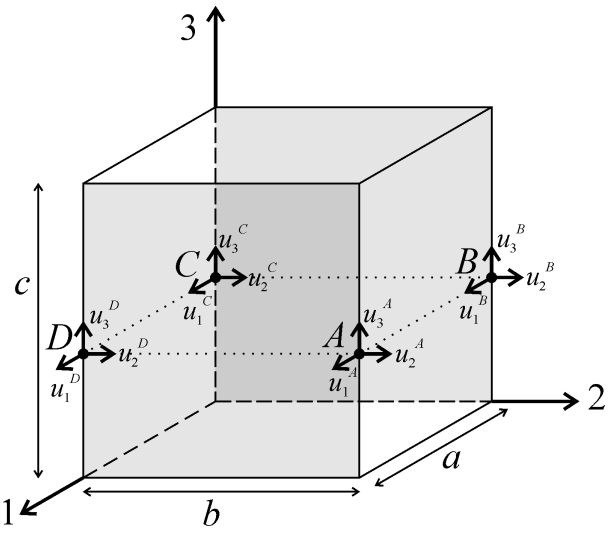

Figure 5.12: Representative volume element and nodes on opposite edges.

K, L, M and N (Fig. 5.13) of the unit cell for the first degree of freedom as

$$u_1^A - u_1^B = a \cdot \varepsilon_{11}, \tag{5.14}$$
$$u_1^N - u_1^M = a \cdot \varepsilon_{11}, \tag{5.15}$$
$$u_1^K - u_1^L = a \cdot \varepsilon_{11}, \tag{5.16}$$
$$u_1^D - u_1^C = a \cdot \varepsilon_{11}, \tag{5.17}$$
$$u_1^A - u_1^K = b \cdot \frac{\gamma_{12}}{2}, \tag{5.18}$$
$$u_1^B - u_1^L = b \cdot \frac{\gamma_{12}}{2}, \tag{5.19}$$
$$u_1^D - u_1^N = b \cdot \frac{\gamma_{12}}{2}, \tag{5.20}$$
$$u_1^C - u_1^M = b \cdot \frac{\gamma_{12}}{2}, \tag{5.21}$$
$$u_1^K - u_1^N = c \cdot \frac{\gamma_{23}}{2}, \tag{5.22}$$
$$u_1^L - u_1^M = c \cdot \frac{\gamma_{23}}{2}, \tag{5.23}$$
$$u_1^A - u_1^D = c \cdot \frac{\gamma_{23}}{2}, \tag{5.24}$$
$$u_1^B - u_1^C = c \cdot \frac{\gamma_{23}}{2}. \tag{5.25}$$

Similarly to the second category of constrains, this set of 12 equations can be reduced to 7 by eliminating for example (5.15), (5.17), (5.19), (5.20) and (5.22). The equations can be obtained and reduced analogously for the latter two degrees of freedom.

To implement the periodical boundary conditions on the micromodel in *Abaqus* the so-called linear multi-point constraints can be used. A linear multi-point constraint is defined as a linear combination of selected nodal degrees of freedom that is equal to zero.

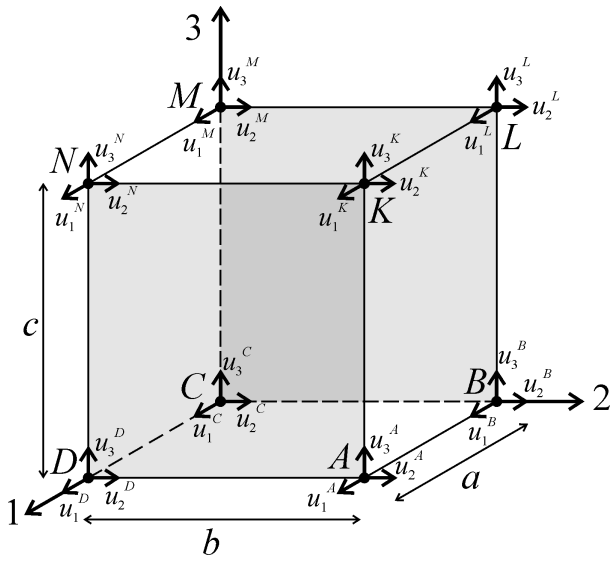

Figure 5.13: Representative volume element and nodes at corners.

For N nodal values it can be written generally in form of

$$A_1 u_i^P + A_2 u_j^Q + \quad \ldots \quad + A_N u_k^R = 0, \tag{5.26}$$

where u is displacement, the superscripts P, Q and R represent nodal ID, the subscripts i, j and k represent the selected degree of freedom (1, 2 or 3), and A_n ($n = 1 \ldots N$) are the coefficients that define the relative motion of given nodes [64].

Therefore, six additional reference points (nodes) designated as e11, e22, e33, g23, g13 and g12 must be created assuming that their displacement [2] (first degree of freedom) values represent one component of the strain vector on right-hand side of the above introduced equations, i.e. ε_{11}, ε_{22}, ε_{33}, γ_{23}, γ_{13} and γ_{12}, respectively. Then, each constraint equation ties the two corresponding degrees of freedom of nodes on the surface of the unit cell and one auxiliary node [65]. For example, the equation (5.8) is represented as

$$\begin{array}{lll} A_1 = 1, & i \sim B, & P = 3, \\ A_2 = -1, & j \sim A, & Q = 3, \\ A_3 = -\frac{a}{2}, & k \sim \text{g13}, & R = 1. \end{array} \tag{5.27}$$

[2] The corresponding force/reaction degree of freedom then represents one corresponding component of the Cauchy stress vector (as defined in chapter 4) multiplied by the volume of the unit cell.

5.5 Material Model Calibration

Two sets of material models were used in micromodels proposed in this work. The first set was designed to simulate overall elastic behavior of the analyzed composite material. Phases of the first micromodel were therefore both modelled as linear elastic materials.

The second set was designed for obtaining numerical response to loading in terms of stress/strain behavior. While the real composite material exhibits significant nonlinear behavior, non-linear material models were used for both phases.

In previous author's work a micromodel with nonlinear material models and with the basic unit cell (Fig. 5.4 – left) was proposed to simulate simple tensile tests [4] and to identify initial failure and damage of substituents [5]. The micromodel with the basic unit cell and nonlinear material parameters was used in [6] to determine the response of the micromodel to tensile cyclic loading. Micromodel with linear material models and irregular fiber distribution was proposed in [3] to compare homogenized material parameters with results of asymptotic homogenization method.

5.5.1 Linear Material Model Calibration

Micromodel designed for simulating the composite material in the elastic range consisted of elements of matrix with linear elastic isotropic material (section 4.1.1) and elements of fibers with linear elastic transversely isotropic material (section 4.1.2).

Material parameters were obtained by optimization process in *optiSLang* by minimizing a residual (using a gradient based algorithm) defined as

$$r_1 = \sum_{\theta} \left(1 - \frac{E^{\mathrm{num}}(\theta)}{E^{\mathrm{exp}}(\theta)} \right)^2, \tag{5.28}$$

where $\theta = \{0°, 15°, 30°, 45°, 60°, 75°, 90°\}$ are orientations of tensile loadings (fiber orientation of specimen),

$$E^{\mathrm{num}}(\theta) = \frac{\sigma^{\mathrm{num}}(\varepsilon^{\mathrm{num}}, \theta)}{\varepsilon^{\mathrm{num}}} \tag{5.29}$$

is Young's modulus of numerical stress/strain dependency obtained by FEA and $E^{\mathrm{exp}}(\theta)$ is experimentally obtained Young's modulus, which was enumerated on strain interval $\varepsilon \in \langle 0.05\ \%;\ 0.25\ \% \rangle$. The strain interval is the interval given in ISO standard [66] for determining Young's modulus. E^{exp} was defined by linear regression of data points on the strain interval of elastic part of the diagram.

Results of numerical analysis were obtained by loading a unit cell with regular fiber distribution (Fig. 5.5) built in *Abaqus/CAE*. Identified parameters are shown in Tab. 5.1.

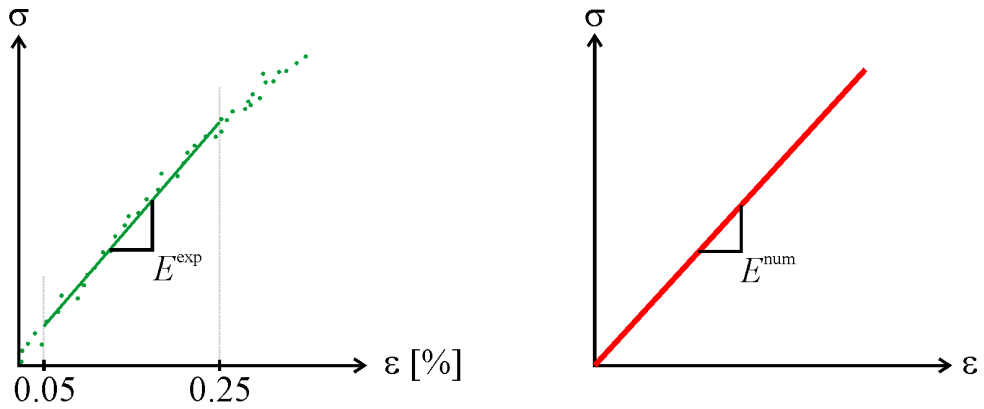

Figure 5.14: Young's moduli of experimentally (green) and numerically (red) obtained data.

Table 5.1: Material parameters of micromodel for identification of homogenized material properties.

fibers	E^{f}_{11}	[GPa]	177.23
	$E^{\mathrm{f}}_{22} = E^{\mathrm{f}}_{33}$	[GPa]	18.00
	$\nu^{\mathrm{f}}_{12} = \nu^{\mathrm{f}}_{13}$	[–]	0.22
	ν^{f}_{23}	[–]	0.40
	$G^{\mathrm{f}}_{12} = G^{\mathrm{f}}_{13}$	[GPa]	51.15
	$G^{\mathrm{f}}_{23} = \frac{E^{\mathrm{f}}_{22}}{2\left(1+\nu^{\mathrm{f}}_{23}\right)}$	[GPa]	6.44
matrix	E_{m}	[GPa]	2.98
	ν_{m}	[–]	0.38

5.5.2 Nonlinear Material Model Calibration

Micromodel for simulating the elastoplastic behavior of the composite material contained isotropic elastoplastic material model assigned to elements of matrix and transversely isotropic nonlinear elastic material assigned to elements of fibers.

Elastic parameters of matrix material were E_{m} and ν_{m} and Von Mises plasticity (4.28) was used with isotropic hardening and work hardening function (4.29) with parameters σ_y^0, P_E, P_A, P_K and n (described in section 4.3.2).

Fibers were modeled as transversely isotropic elastic material and the Young's modulus in fiber direction E_{11} was proposed in a form of a function of strain in fiber direction (4.23) due to nonlinear behavior of the composite along fiber direction (Fig. 2.4). The material model of fibers was implemented to *Abaqus/CAE* by user's subroutine UMAT written in *Fortran*.

Parameters of the material models were obtained by optimization process similar to the one in section 5.5.1. The residual was defined as

$$r_2 = \sum_{\theta} \sum_{i} \left(\frac{\varepsilon^{\mathrm{num}}\left(\theta, \sigma_i^{\theta}\right) - \varepsilon^{\mathrm{exp}}\left(\theta, \sigma_i^{\theta}\right)}{\varepsilon_{\mathrm{max}}^{\mathrm{exp}}\left(\theta\right)} \right)^2 . \tag{5.30}$$

The strain was evaluated for 20 values of stress σ_i^{θ} for given fiber orientation (Fig. 5.15) linearly spaced on interval $\sigma_i^{\theta} \in \langle 0;\ \sigma_{\mathrm{max}}^{\mathrm{exp}}\left(\theta\right)\rangle$. Identified material parameters of the model are summarized in Tab. 5.2 and stress/strain dependencies obtained from micromodel with the identified parameters is shown in Fig. 5.16.

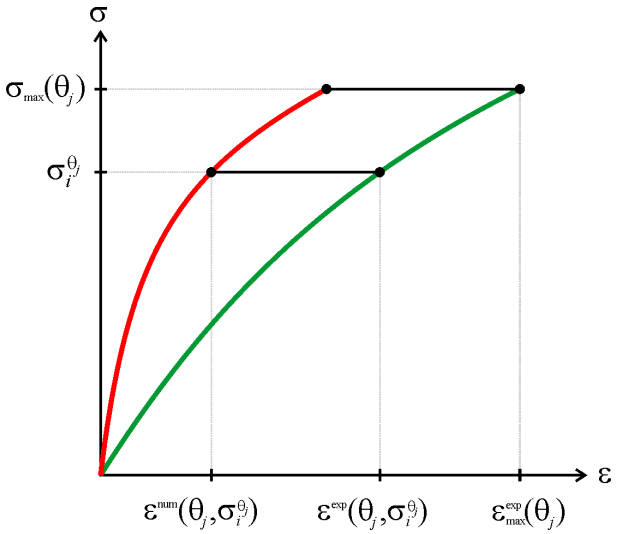

Figure 5.15: Principle of r_2 calculation using experimentally (green) and numerically (red) obtained stress/strain dependencies.

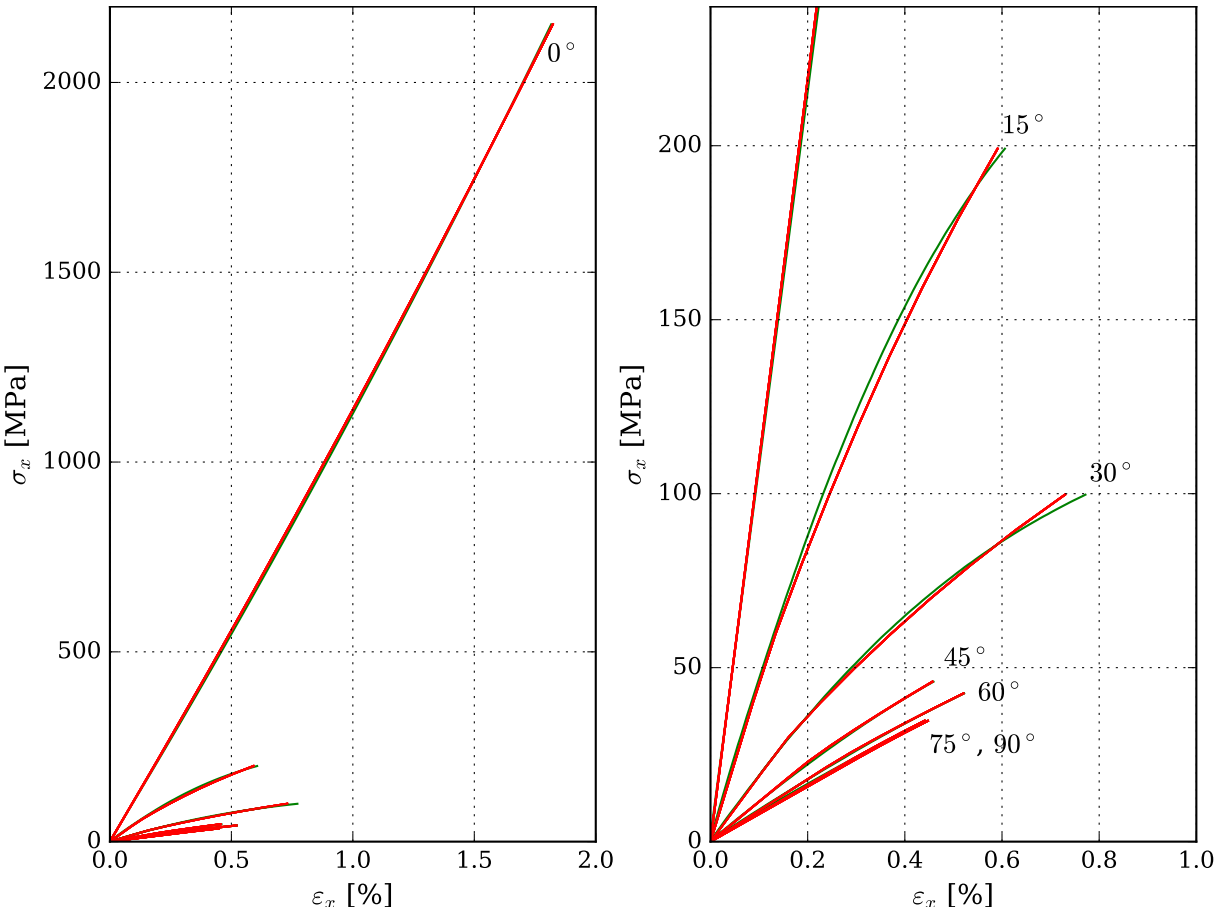

Figure 5.16: stress/strain dependencies obtained numerically (red) and experimentally (green).

Table 5.2: Material parameters of micromodel for numerical tensile test dependencies.

fibers			matrix		
E^0_{11}	[GPa]	179.47	E_m	[GPa]	3.3
$E^\mathrm{f}_{22} = E^\mathrm{f}_{33}$	[GPa]	16.88	ν_m	[–]	0.33
$\nu^\mathrm{f}_{12} = \nu^\mathrm{f}_{13}$	[–]	0.25	σ^0_y	[MPa]	23.14
ν^f_{23}	[–]	0.40	P_E	[GPa]	9.82
$G^\mathrm{f}_{12} = G^\mathrm{f}_{13}$	[GPa]	55.44	P_A	[MPa]	119.82
$G^\mathrm{f}_{23} = \frac{E^\mathrm{f}_{22}}{2\left(1+\nu^\mathrm{f}_{23}\right)}$	[GPa]	6.03	P_K	[MPa]	764.49
g	[–]	9.93	n	[–]	0.86

5.6 Coordinate Systems

Micromodels were built in local Cartesian coordinate system (123). Axis 1 is identical to the axis of fibers and axes 2 and 3 are perpendicular to axis 1 (Fig. 5.17). Loading is defined in global coordinate system (xyz). If the global and local coordinate systems are rotated, the stress vector expressing the loading state was transformed to the local coordinate system of the micromodel (section 5.6.1).

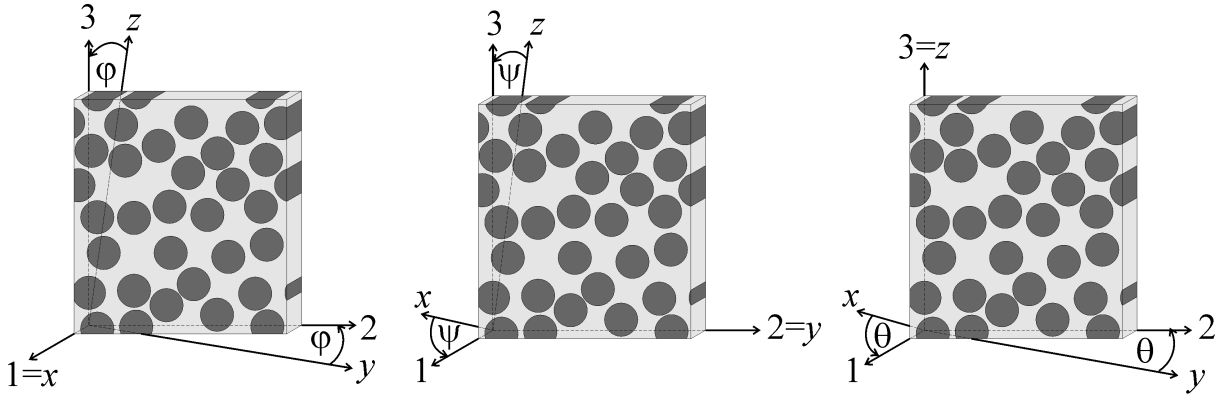

Figure 5.17: Rotated coordinate systems.

The loaded micromodel deformed and the strain was given in the coordinate system (123). If the global coordinate system (xyz), where loading was defined is rotated, the strain obtained by numerical analysis in (123) was transformed back to system (xyz) (section 5.6.2).

5.6.1 Stress Transformation

If right-handed rotation of coordinate system about one axis is considered (Fig. 5.17), relationship between stresses defined in the two different coordinate systems is given by the stress-transformation law

$$\boldsymbol{\sigma}_{123} = \mathbf{T}_{\sigma}\boldsymbol{\sigma}_{xyz}, \tag{5.31}$$

where the transformation matrix $\mathbf{T}_{\sigma}$ depends on the axis about which the coordinate systems are rotated.

Rotation about axis 1

If the global coordinate system, where loading stress is defined is rotated about axis 1 of the local coordinate system (Fig. 5.17 – left), stress (123) is calculated as

$$\begin{bmatrix}\sigma_{11}\\ \sigma_{22}\\ \sigma_{33}\\ \tau_{23}\\ \tau_{13}\\ \tau_{12}\end{bmatrix} = \begin{bmatrix}1 & 0 & 0 & 0 & 0 & 0\\ 0 & \cos^2\varphi & \sin^2\varphi & 2\sin\varphi\cos\varphi & 0 & 0\\ 0 & \sin^2\varphi & \cos^2\varphi & -2\sin\varphi\cos\varphi & 0 & 0\\ 0 & -\sin\varphi\cos\varphi & \sin\varphi\cos\varphi & \cos^2\varphi-\sin^2\varphi & 0 & 0\\ 0 & 0 & 0 & 0 & \cos\varphi & -\sin\varphi\\ 0 & 0 & 0 & 0 & \sin\varphi & \cos\varphi\end{bmatrix}\begin{bmatrix}\sigma_{xx}\\ \sigma_{yy}\\ \sigma_{zz}\\ \tau_{yz}\\ \tau_{xz}\\ \tau_{xy}\end{bmatrix}. \quad (5.32)$$

Rotation about axis 2

If global coordinate system is rotated about axis 2 of local coordinate system (Fig. 5.17 – middle), stress in (123) is defined as

$$\begin{bmatrix}\sigma_{11}\\ \sigma_{22}\\ \sigma_{33}\\ \tau_{23}\\ \tau_{13}\\ \tau_{12}\end{bmatrix} = \begin{bmatrix}\cos^2\psi & 0 & \sin^2\psi & 0 & -2\sin\psi\cos\psi & 0\\ 0 & 1 & 0 & 0 & 0 & 0\\ \sin^2\psi & 0 & \cos^2\psi & 0 & 2\sin\psi\cos\psi & 0\\ 0 & 0 & 0 & \cos\psi & 0 & \sin\psi\\ \sin\psi\cos\psi & 0 & -\sin\psi\cos\psi & 0 & \cos^2\psi-\sin^2\psi & 0\\ 0 & 0 & 0 & -\sin\psi & 0 & \cos\psi\end{bmatrix}\begin{bmatrix}\sigma_{xx}\\ \sigma_{yy}\\ \sigma_{zz}\\ \tau_{yz}\\ \tau_{xz}\\ \tau_{xy}\end{bmatrix}. \quad (5.33)$$

Rotation about axis 3

If global coordinate system is rotated about axis 3 of the local coordinate system (Fig. 5.17 – right), stress in (123) is defined as

$$\begin{bmatrix}\sigma_{11}\\ \sigma_{22}\\ \sigma_{33}\\ \tau_{23}\\ \tau_{13}\\ \tau_{12}\end{bmatrix} = \begin{bmatrix}\cos^2\theta & \sin^2\theta & 0 & 0 & 0 & 2\sin\theta\cos\theta\\ \sin^2\theta & \cos^2\theta & 0 & 0 & 0 & -2\sin\theta\cos\theta\\ 0 & 0 & 1 & 0 & 0 & 0\\ 0 & 0 & 0 & \cos\theta & -\sin\theta & 0\\ 0 & 0 & 0 & \sin\theta & \cos\theta & 0\\ -\sin\theta\cos\theta & \sin\theta\cos\theta & 0 & 0 & 0 & \cos^2\theta-\sin^2\theta\end{bmatrix}\begin{bmatrix}\sigma_{xx}\\ \sigma_{yy}\\ \sigma_{zz}\\ \tau_{yz}\\ \tau_{xz}\\ \tau_{xy}\end{bmatrix}. \quad (5.34)$$

5.6.2 Strain Transformation

The micromodel loaded by stress $\boldsymbol{\sigma}_{123}$ is deformed and strain $\boldsymbol{\varepsilon}_{123}$ is obtained. If the global coordinate system (xyz), where loading state is defined, is rotated from local coordinate system (123), where strain is obtained, strain in (xyz) is given by the strain-transformation law

$$\boldsymbol{\varepsilon}_{xyz} = \left[\mathbf{T}_{\varepsilon}\right]^{-1}\boldsymbol{\varepsilon}_{123}, \quad (5.35)$$

where the transformation matrix $\mathbf{T}_{\varepsilon}$ differs for each axis of (123) about which the coordinate systems are rotated.

Rotation about axis 1

Inverse transformation of strain between coordinate systems rotated about axis 1 (Fig. 5.17 – left) is given as

$$\begin{bmatrix} \varepsilon_{xx} \\ \varepsilon_{yy} \\ \varepsilon_{zz} \\ \gamma_{yz} \\ \gamma_{xz} \\ \gamma_{xy} \end{bmatrix} = \begin{bmatrix} 1 & 0 & 0 & 0 & 0 & 0 \\ 0 & \cos^2\varphi & \sin^2\varphi & -\sin\varphi\cos\varphi & 0 & 0 \\ 0 & \sin^2\varphi & \cos^2\varphi & \sin\varphi\cos\varphi & 0 & 0 \\ 0 & 2\sin\varphi\cos\varphi & -2\sin\varphi\cos\varphi & \cos^2\varphi - \sin^2\varphi & 0 & 0 \\ 0 & 0 & 0 & 0 & \cos\varphi & \sin\varphi \\ 0 & 0 & 0 & 0 & -\sin\varphi & \cos\varphi \end{bmatrix} \begin{bmatrix} \varepsilon_{11} \\ \varepsilon_{22} \\ \varepsilon_{33} \\ \gamma_{23} \\ \gamma_{13} \\ \gamma_{12} \end{bmatrix}. \tag{5.36}$$

Rotation about axis 2

Inverse transformation of strain between coordinate systems rotated about axis 2 (Fig. 5.17 – middle) is given as

$$\begin{bmatrix} \varepsilon_{xx} \\ \varepsilon_{yy} \\ \varepsilon_{zz} \\ \gamma_{yz} \\ \gamma_{xz} \\ \gamma_{xy} \end{bmatrix} = \begin{bmatrix} \cos^2\psi & 0 & \sin^2\psi & 0 & \sin\psi\cos\psi & 0 \\ 0 & 1 & 0 & 0 & 0 & 0 \\ \sin^2\psi & 0 & \cos^2\psi & 0 & -\sin\psi\cos\psi & 0 \\ 0 & 0 & 0 & \cos\psi & 0 & -\sin\psi \\ -2\sin\psi\cos\psi & 0 & 2\sin\psi\cos\psi & 0 & \cos^2\psi - \sin^2\psi & 0 \\ 0 & 0 & 0 & \sin\psi & 0 & \cos\psi \end{bmatrix} \begin{bmatrix} \varepsilon_{11} \\ \varepsilon_{22} \\ \varepsilon_{33} \\ \gamma_{23} \\ \gamma_{13} \\ \gamma_{12} \end{bmatrix}. \tag{5.37}$$

Rotation about axis 3

Inverse transformation of strain between coordinate systems rotated about axis 3 (Fig. 5.17 – right) is given as

$$\begin{bmatrix} \varepsilon_{xx} \\ \varepsilon_{yy} \\ \varepsilon_{zz} \\ \gamma_{yz} \\ \gamma_{xz} \\ \gamma_{xy} \end{bmatrix} = \begin{bmatrix} \cos^2\theta & \sin^2\theta & 0 & 0 & 0 & -\sin\theta\cos\theta \\ \sin^2\theta & \cos^2\theta & 0 & 0 & 0 & \sin\theta\cos\theta \\ 0 & 0 & 1 & 0 & 0 & 0 \\ 0 & 0 & 0 & \cos\theta & \sin\theta & 0 \\ 0 & 0 & 0 & -\sin\theta & \cos\theta & 0 \\ 2\sin\theta\cos\theta & -2\sin\theta\cos\theta & 0 & 0 & 0 & \cos^2\theta - \sin^2\theta \end{bmatrix} \begin{bmatrix} \varepsilon_{11} \\ \varepsilon_{22} \\ \varepsilon_{33} \\ \gamma_{23} \\ \gamma_{13} \\ \gamma_{12} \end{bmatrix}. \tag{5.38}$$

The following relationship is valid for transformation matrices

$$[\mathbf{T}_\varepsilon(\theta)]^{-1} = [\mathbf{T}_\varepsilon(-\theta)] = [\mathbf{T}_\sigma(\theta)]^{\mathrm{T}}. \tag{5.39}$$

The relations for φ and ψ can be written analogically [59].

5.7 Definition of Loading

The unit cell was loaded by stress (section 5.4) in local coordinate system (123) of the micromodel. The load state in (123) of the micromodel was calculated from the load as defined in global coordinate system (xyz).

5.7.1 Homogenized Material Properties

To obtain homogenized material properties of the micromodel (lamina), the unit cell is loaded according to uniaxial stress (pure tension or pure shear) defined in global coordinate system (xyz) by stresses

$$\begin{aligned}
\boldsymbol{\sigma}^1_{xyz} &= [1,\ 0,\ 0,\ 0,\ 0,\ 0]^{\mathrm{T}}\ \mathrm{MPa},\\
\boldsymbol{\sigma}^2_{xyz} &= [0,\ 1,\ 0,\ 0,\ 0,\ 0]^{\mathrm{T}}\ \mathrm{MPa},\\
\boldsymbol{\sigma}^3_{xyz} &= [0,\ 0,\ 1,\ 0,\ 0,\ 0]^{\mathrm{T}}\ \mathrm{MPa},\\
\boldsymbol{\sigma}^4_{xyz} &= [0,\ 0,\ 0,\ 1,\ 0,\ 0]^{\mathrm{T}}\ \mathrm{MPa},\\
\boldsymbol{\sigma}^5_{xyz} &= [0,\ 0,\ 0,\ 0,\ 1,\ 0]^{\mathrm{T}}\ \mathrm{MPa},\\
\boldsymbol{\sigma}^6_{xyz} &= [0,\ 0,\ 0,\ 0,\ 0,\ 1]^{\mathrm{T}}\ \mathrm{MPa}.
\end{aligned}$$

If local coordinate system (123) is not equal to the global coordinate system (xyz), stress $\boldsymbol{\sigma}^i_{123}$ is given by corresponding equation defined in section 5.6.1 equations (5.32) – (5.34).

Loads corresponding to $\boldsymbol{\sigma}^i_{123}$ are applied to appropriate reference points created during applying periodic boundary conditions described in section 5.4. The stresses $\boldsymbol{\sigma}^i_{123}$ are applied one at a time in a particular loading step.

5.7.2 Tensile Tests

If the unit cell is loaded according to experimental tensile tests, stress in the global coordinate system is given by $\boldsymbol{\sigma}_{xyz} = [\sigma_{xx}, 0, 0, 0, 0, 0]^{\mathrm{T}}$, which corresponds to uniaxial tension, where

$$\sigma_{xx} = \frac{F_x}{A}, \tag{5.40}$$

F_x is the loading force and A is the specimen cross-section. The unit cell is loaded by $\boldsymbol{\sigma}_{123}$ calculated using (5.34), where θ is the fiber orientation of the specimen (Fig. 2.1). The unit cell is loaded in 10 steps up to strength given by averaging the experiments for particular fiber orientation (Fig. 2.4). The corresponding loads are again applied to the reference points.

5.8 Acquisition of FEA Results

Results of FEA are evaluated from strain values obtained from the reference points (section 5.4). The strains were enumerated in local coordinate system by FEA of the micromodel and then transformed to global coordinate system and further processed to obtain data needed for the given analysis.

5.8.1 Homogenized Material Properties

To evaluate the material properties of a lamina, the generalized Hooke's law (4.3) was assumed with compliance matrix $\mathbf{S}$ of anisotropic material (4.16). Response of the micromodel to load defined by 6 different stresses $\boldsymbol{\sigma}^i_{xyz}$ (section 5.40) in 6 steps was obtained by FEA. Components of strain in $\boldsymbol{\varepsilon}^i_{123}$ in local coordinate system (123) were obtained from the displacement (first degree of freedom) value of the particular additional reference node used for applying periodical boundary conditions (in section 5.4).

The strain was transformed to global coordinate system (xyz) by the appropriate relationship (5.36) or (5.37) or (5.38). The homogenized material parameters of the unit cell were obtained from particular steps of the analysis using (4.3) as

$$\boldsymbol{\sigma}_{xyz} = \boldsymbol{\sigma}^1_{xyz} \xrightarrow{\text{FEA}} \boldsymbol{\varepsilon}_{xyz} = \boldsymbol{\varepsilon}^1_{xyz} \quad \begin{cases} E_x = \frac{\sigma_{xx}}{\varepsilon_{xx}}, \\ \nu_{xy} = -\frac{\varepsilon_{yy}}{\varepsilon_{xx}}, \\ \nu_{xz} = -\frac{\varepsilon_{zz}}{\varepsilon_{xx}}, \end{cases} \tag{5.41}$$

$$\boldsymbol{\sigma}_{xyz} = \boldsymbol{\sigma}^2_{xyz} \xrightarrow{\text{FEA}} \boldsymbol{\varepsilon}_{xyz} = \boldsymbol{\varepsilon}^2_{xyz} \quad \begin{cases} E_y = \frac{\sigma_{yy}}{\varepsilon_{yy}}, \\ \nu_{yx} = -\frac{\varepsilon_{xx}}{\varepsilon_{yy}}, \\ \nu_{yz} = -\frac{\varepsilon_{zz}}{\varepsilon_{yy}}, \end{cases} \tag{5.42}$$

$$\boldsymbol{\sigma}_{xyz} = \boldsymbol{\sigma}^3_{xyz} \xrightarrow{\text{FEA}} \boldsymbol{\varepsilon}_{xyz} = \boldsymbol{\varepsilon}^3_{xyz} \quad \begin{cases} E_z = \frac{\sigma_{zz}}{\varepsilon_{zz}}, \\ \nu_{zx} = -\frac{\varepsilon_{xx}}{\varepsilon_{zz}}, \\ \nu_{zy} = -\frac{\varepsilon_{yy}}{\varepsilon_{zz}}, \end{cases} \tag{5.43}$$

$$\boldsymbol{\sigma}_{xyz} = \boldsymbol{\sigma}^4_{xyz} \xrightarrow{\text{FEA}} \boldsymbol{\varepsilon}_{xyz} = \boldsymbol{\varepsilon}^4_{xyz} \quad \begin{cases} G_{yz} = \frac{\tau_{yz}}{\gamma_{yz}}, \end{cases} \tag{5.44}$$

$$\boldsymbol{\sigma}_{xyz} = \boldsymbol{\sigma}^5_{xyz} \xrightarrow{\text{FEA}} \boldsymbol{\varepsilon}_{xyz} = \boldsymbol{\varepsilon}^5_{xyz} \quad \begin{cases} G_{xz} = \frac{\tau_{xz}}{\gamma_{xz}}, \end{cases} \tag{5.45}$$

$$\boldsymbol{\sigma}_{xyz} = \boldsymbol{\sigma}^6_{xyz} \xrightarrow{\text{FEA}} \boldsymbol{\varepsilon}_{xyz} = \boldsymbol{\varepsilon}^6_{xyz} \quad \begin{cases} G_{xy} = \frac{\tau_{xy}}{\gamma_{xy}}. \end{cases} \tag{5.46}$$

The additional constants μ and η defined in (4.17), (4.18) and (4.19) were not calculated.

5.8.2 Tensile Tests

Response of the micromodel to loading defined according to uniaxial stress (pure tension) in global coordinate system (xyz) was evaluated in 10 steps. The strain $\boldsymbol{\varepsilon}_{123}$

evaluated in local coordinate system of the micromodel was transformed to global coordinate system (xyz), whose axis x is the direction of loading according to the experimental tensile tests. The strain $\boldsymbol{\varepsilon}_{xyz}$ was obtained using (5.38) and the resulting stress/strain dependencies $\sigma_x(\varepsilon_x)$ were plotted as graphs.

5.9 Micromodel Sensitivity Analyses

Analyses performed for purposes of investigating the influence of geometrical or parameter variations of the micromodels on results of FEA and time consumption were performed on unit cells with regular fiber distribution. The results of the analyses were used to validate the chosen mesh fineness and material models for the further computations.

First, homogenized material parameters were identified for a basic unit cell and compared with the parameters of a unit cell consisted of 4×7 basic unit cells. The computational time for obtaining the homogenized parameters was compared for both unit cells. Then a sensitivity of the identified material parameters on mesh fineness was determined. The results of the mesh fineness analysis were used for defining the element size in all oncoming analyses. Last, the influence of material parameters variation on FEA results was investigated for validating the chosen material models.

5.9.1 Influence of Regular Unit Cell Size

Homogenized material properties of a basic unit cell (Fig. 5.18 – left) consisting of two fibers and three duplicated were compared with properties of the unit cell **a** (Fig. 5.18 – right) consisting of 56 fibers (and 12 duplicated) made of 4×7 of the basic unit cell. The basic unit cell is the smallest 3D cuboid representative volume element of the hexagonal fiber distribution approximation.

The bigger unit cell consists of 11284 elements (7416 – fibers, 3868 – matrix) and the basic one of 395 elements (260 – fibers, 135 – matrix). Both micromodels with linear material models have the same fiber volume fraction V_f, same thickness a and the same quality of mesh.

The computational time for analysis of material properties in global coordinate system (xyz) in case of the basic unit cell was 15 times shorter in terms of FEA (1 s – basic unit cell, 15 s – unit cell **a**). In terms of the whole procedure shown in Fig. 5.1 and performed automatically by a set of scripts written in *Python*, the analysis time for the basic unit cell is 9 times shorter (21 min – basic unit cell, 193 min – unit cell **a**). The analysis was performed on computer with CPU type Intel Core i7 950 @ 3.07 GHz and 14 GB RAM.

The extreme values of homogenized material properties of the basic unit cell were nearly identical to parameters of unit cell **a** (Tab. 5.3). Only in case of maximum value of Young's moduli in the plane perpendicular to fiber direction the value varied by 1.2 % which can be considered as a numerical error.

We can state, that in the case of unit cells with regular fiber distribution, there is

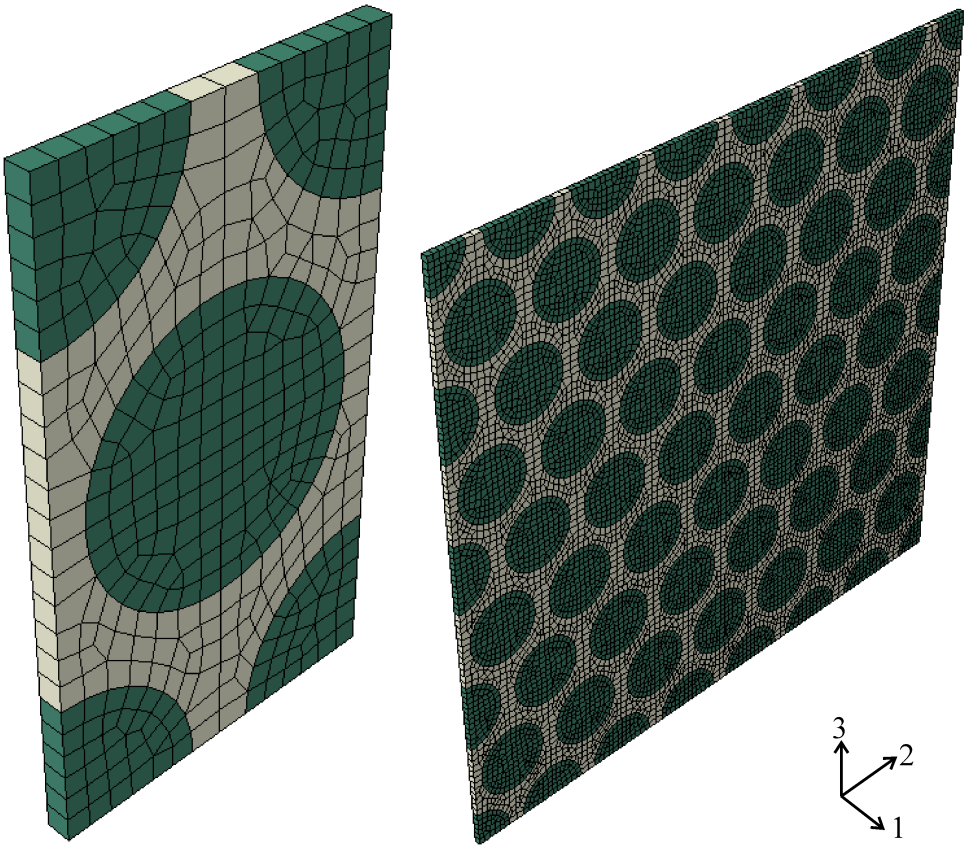

Figure 5.18: Micromodels of unit cells with 2 fibers (left) and 56 fibers (right) with regular fiber distribution.

negligible influence of the number of basic cell repetitions on homogenized material properties of the unit cell. From the point of view of computational time, it is beneficial to use the basic unit cell.

Table 5.3: Selected material properties of unit cell **a** and basic unit cell and comparison of their extreme values of homogenized properties.

	unit cell **a** extremes		basic unit cell extremes		deviation	
$E_{yy,zz}$	7.946	GPa	7.946	GPa	0.0	%
	7.951	GPa	7.950	GPa	1.2	%
G_{yz}	2.666	GPa	2.666	GPa	0.0	%
	2.667	GPa	2.667	GPa	0.0	%
ν_{yz}	0.490		0.490		0.0	%
	0.491		0.491		0.0	%

5.9.2 Influence of Mesh Fineness

Mesh fineness has considerable impact on accuracy of finite element analysis [67]. Hence the influence of mesh fineness of proposed micromodel with linear material models on accuracy of finite element analysis solution was investigated. The sensitivity of fiber volume fraction of the micromodel geometry on the element size was also examined. The element size was defined by the mesh seeding parameter

$$l_{\text{seed}} = \frac{2\pi R_{\text{f}}}{n_{\text{el}}}, \tag{5.47}$$

where n_{el} is the number of elements within the fiber circumference. The seeding parameter also defines the thickness of the micromodel $a = l_{\text{seed}}$.

Mesh element size has influence on the resulting fiber volume fraction V_{f} of the micromodel. A circle in the plane 23 defines the mesh points on the edge of fibers and matrix. The resulting volume of mesh belonging to fiber is smaller than the volume of circle determining the fiber-matrix interface polygon. The circle is circumscribed circle of this polygon (Fig. 5.19).

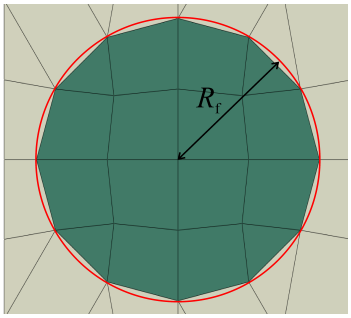

Figure 5.19: Part of micromodel with mesh for $n_{\text{el}} = 12$ elements.

The radius R_{f} of circles defining the fiber area in micromodel geometry was responding to relationship (5.2) for chosen fiber volume fraction $V_{\text{f}} = 60$ %, therefore the resulting fiber volume fraction of the micromodel was always smaller. The desired fiber volume fraction $V_{\text{f}} = 60$ % is an asymptotic value of a function of prescribed fiber volume fraction of the micromodel depending on parameter n_{el} (5.47) defining the mesh fineness (Fig. 5.20).

Elastic material models and loading by uniaxial stress (pure tension or pure shear) is used to determine homogenized material properties of micromodels with different mesh fineness. Inadequate mesh element size caused significant error in the homogenized material properties identified by finite element analysis (Fig. 5.21).

The performed analyses resulted in suitable mesh fineness defined by the number of elements within the fiber circumference $n_{\text{el}} = 36$. For mentioned value, the identified homogenized material properties may be considered as settled (Fig. 5.21). The chosen mesh fineness with seeding parameter given as

$$l_{\text{seed}} = \frac{2\pi R_{\text{f}}}{36} = 0.09$$

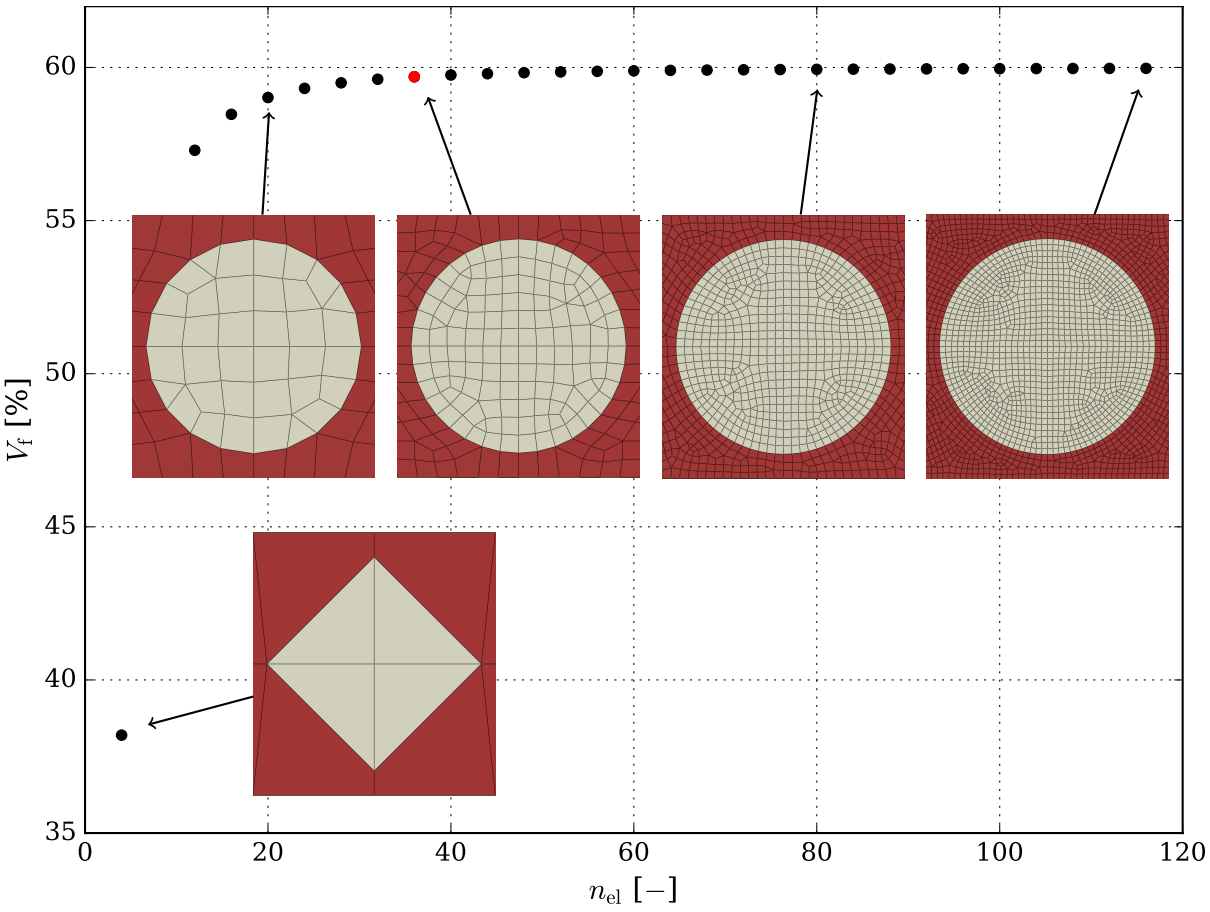

Figure 5.20: Dependency of fiber volume ratio of the micromodel on parameter n_{el} defining the mesh element size (red point corresponds to $n_{el} = 36$).

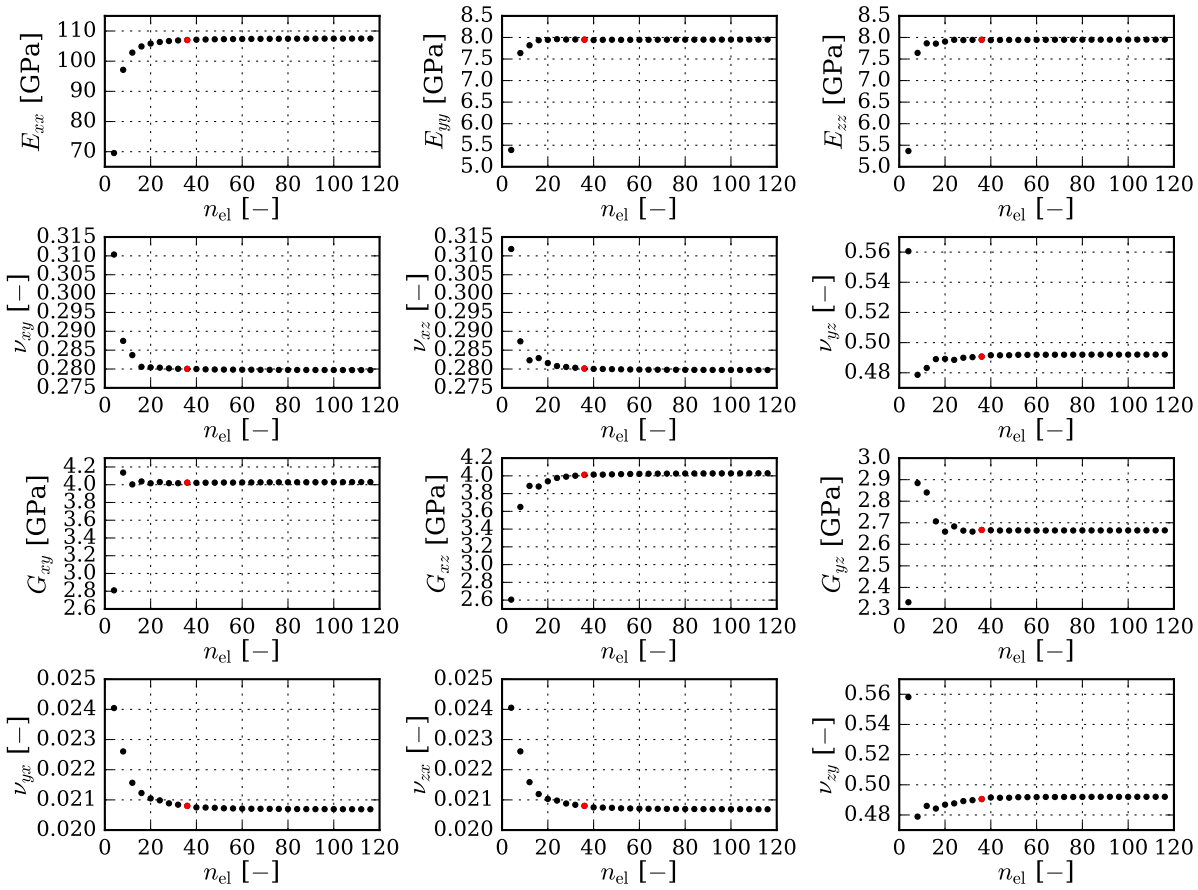

Figure 5.21: Dependency of homogenized properties of the micromodel on parameter n_{el} defining the mesh element size (red point corresponds to $n_{\mathrm{el}} = 36$).

is a compromise between CPU time consumption and accuracy of results. The fiber volume ratio of the micromodel with given mesh is $V_{\mathrm{f}} = 59.7$ % (Fig. 5.18 – right). Chosen mesh fineness was used in the following analyses in case of both types of micromodels – the micromodel with linear material models (section 5.5.1) designed for determining the homogenized material properties of lamina and the micromodel with non-linear material models (section 5.5.2) designed for calculation of numerical stress-strain dependencies.

With given mesh fineness, the model mesh consisted of approximately 12 thousand elements. The exact number of elements and types for micromodels with regular fiber distribution (Fig. 5.5), with clustered fibers (Fig. 5.6) and fibers aligned in a stripe of fibers (Fig. 5.7) are summarized in Tab. 5.4.

5.9.3 Sensitivity of Homogenized Properties

Micromodel with linear material models and regular fiber distribution was subjected to analysis of influence of material parameter variation using a one-at-a-time method (OAT).

Table 5.4: Numbers of elements and their types for micromodels with different geometries.

elements	micromodel geometry			
	regular Fig. 5.5	cluster Fig. 5.6	stripe Fig. 5.7	random Fig. 5.10
all	11284	12182	12396	12217
C3D8	10788	11634	11814	11401
C3D6	496	548	582	816

The influence of material parameter variation on homogenized material properties of the micromodel was investigated. The finite element analyses were performed with material parameters of phases of the micromodel variating in range ±10 % of the values identified in section 5.5.1 (Tab. 5.1). The material parameters were variated with a step of 1 %. Values of homogenized material properties defined using the identified material parameters of micromodel are listed in Tab. 5.5.

Table 5.5: Homogenized material properties of regular unit cell with identified material parameters.

parameter	value	
E_{xx}	107.02	[GPa]
E_{yy}	7.95	[GPa]
E_{zz}	7.95	[GPa]
ν_{xy}	0.28	[–]
ν_{xz}	0.28	[–]
ν_{yz}	0.49	[–]
G_{xy}	4.02	[GPa]
G_{xz}	4.01	[GPa]
G_{yz}	2.67	[GPa]
ν_{yx}	0.02	[–]
ν_{zx}	0.02	[–]
ν_{zy}	0.49	[–]

Effect of the OAT material parameter variations on homogenized properties are coded in Tab. 5.6. Code **0** designates that the homogenized parameter is not affected by the change of given parameter. Codes $+\mathbf{L}$ and $-\mathbf{L}$ mean that the homogenized material is linearly dependent on the material parameter with a positive or negative constant of proportionality, respectively. Codes $+\mathbf{Q}$ and $-\mathbf{Q}$ significate that there is quadratic dependence of the homogenized property on the parameter with a positive or negative coefficient, respectively.

The analyzed dependencies of one at a time change of material parameter of the proposed micromodel on the resulting homogenized material properties are depicted in

Table 5.6: Coded effects of one-at-a-time material parameter change on homogenized material properties (0 – no influence, L – linear dependence, Q – quadratic dependence).

	E_{11}^{f}	E_{22}^{f}	E_{33}^{f}	ν_{12}^{f}	ν_{13}^{f}	ν_{23}^{f}	G_{12}^{f}	G_{13}^{f}	G_{23}^{f}	E_{m}	ν_{m}
E_{xx}	L	0	0	−L	−L	0	0	0	0	L	Q
E_{yy}	L	L	L	−L	L	−L	0	0	L	L	Q
E_{zz}	L	L	L	L	−L	−L	0	0	L	L	Q
ν_{xy}	0	0	0	L	−L	0	0	0	0	0	L
ν_{xz}	0	0	−L	−L	L	0	0	0	0	0	L
ν_{yz}	L	L	−L	−L	−L	L	0	0	−L	−Q	L
G_{xy}	0	0	0	0	0	0	L	L	0	L	−L
G_{xz}	0	0	0	0	0	0	L	L	0	L	−L
G_{yz}	L	L	L	L	0	−L	0	0	L	L	Q
ν_{yx}	−L	L	L	L	−L	−L	−L	0	L	L	L
ν_{zx}	−L	L	L	−L	L	−L	−L	0	L	L	L
ν_{zy}	L	−L	L	−L	−L	L	0	0	−L	−Q	L

Figs. 5.22 to 5.29. For easy comparison, the scales defining the homogenized properties have the same scale for all variating material parameters. Red point in the dependence signifies the homogenized property (Tab. 5.5) of a micromodel with identified material parameters.

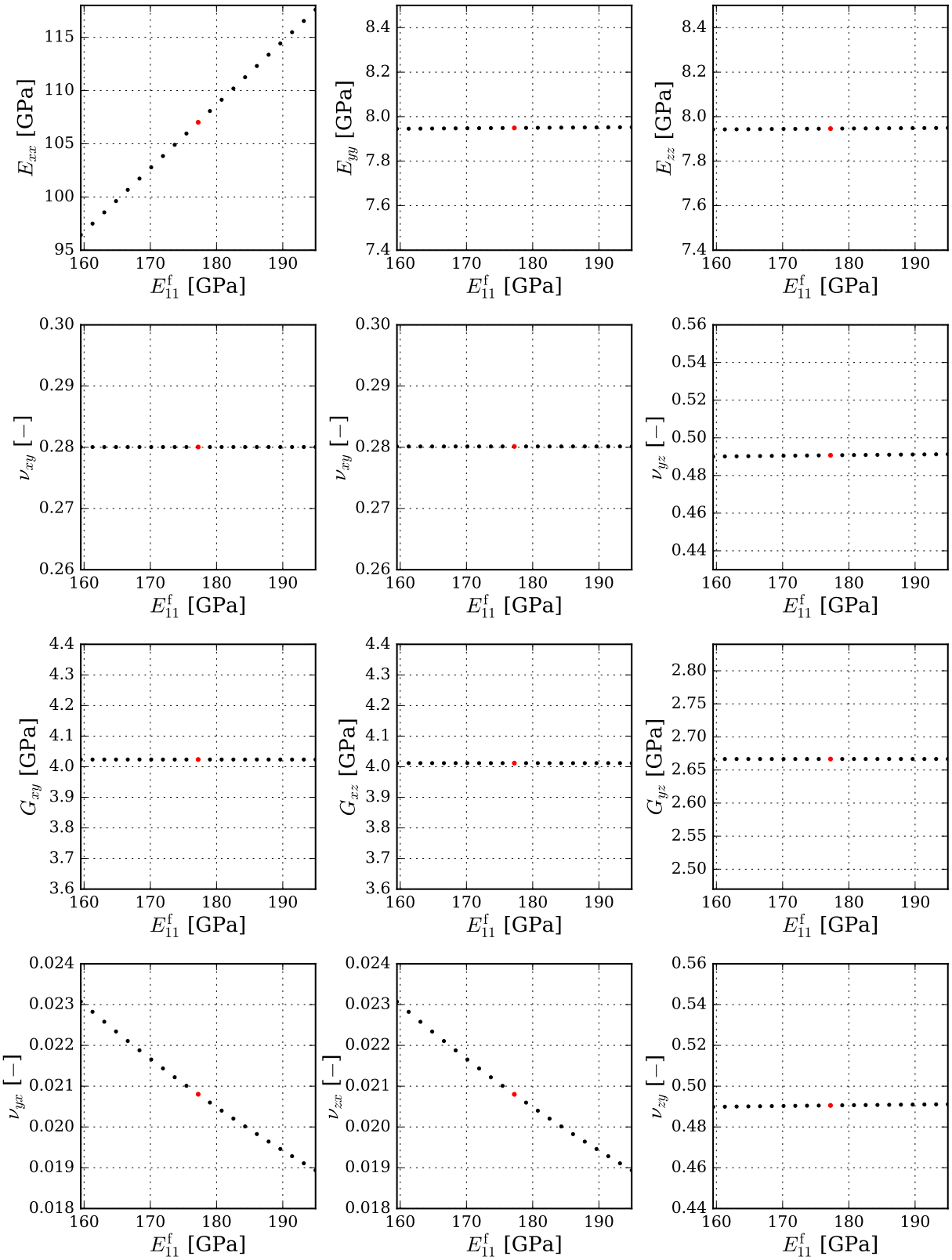

Figure 5.22: Sensitivity of homogenized material properties to variation of Young's modulus of fibers E_{11}^{f}.

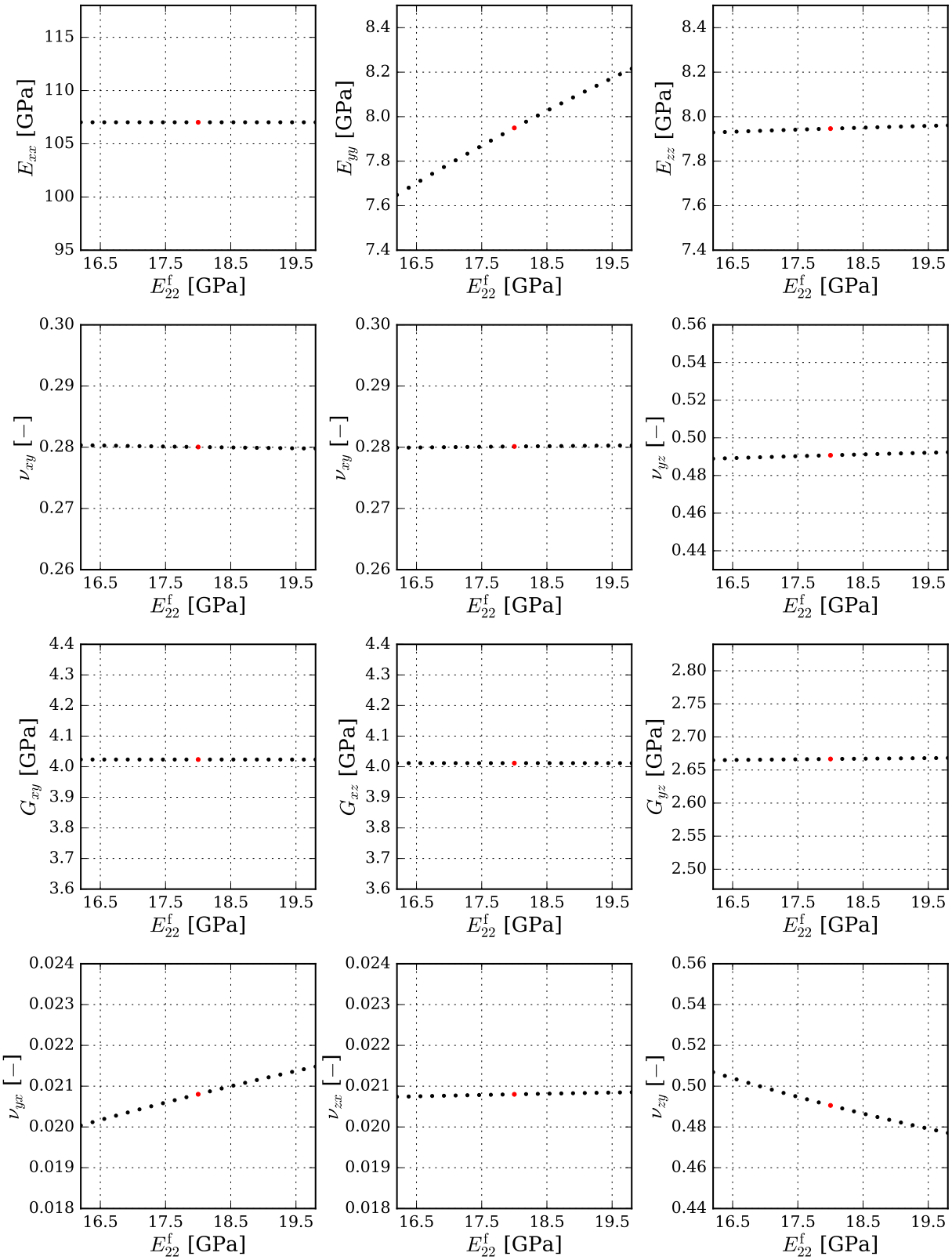

Figure 5.23: Sensitivity of homogenized material properties to variation of Young's modulus of fibers E_{22}^{f}.

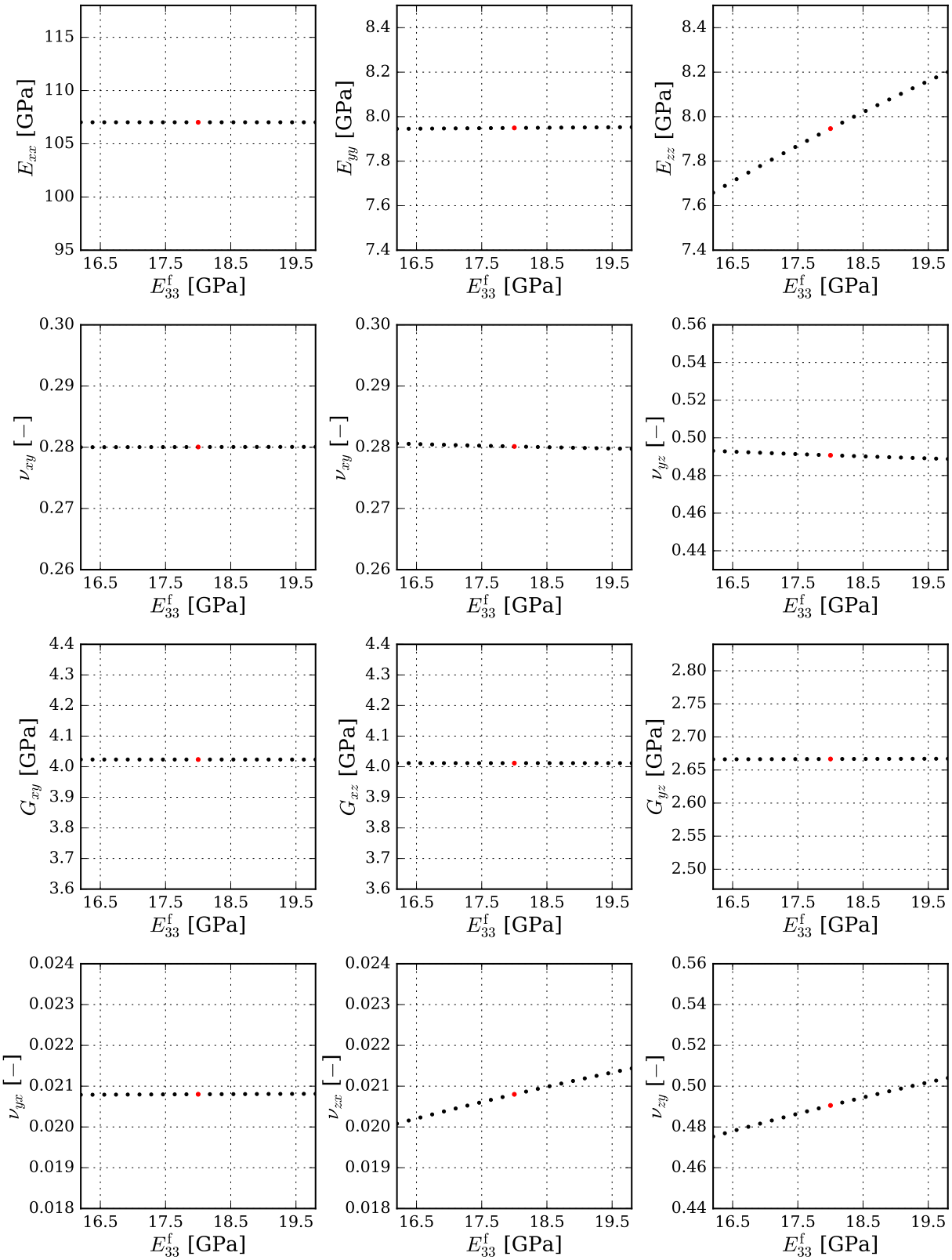

Figure 5.24: Sensitivity of homogenized material properties to variation of Young's modulus of fibers E^{f}_{33}.

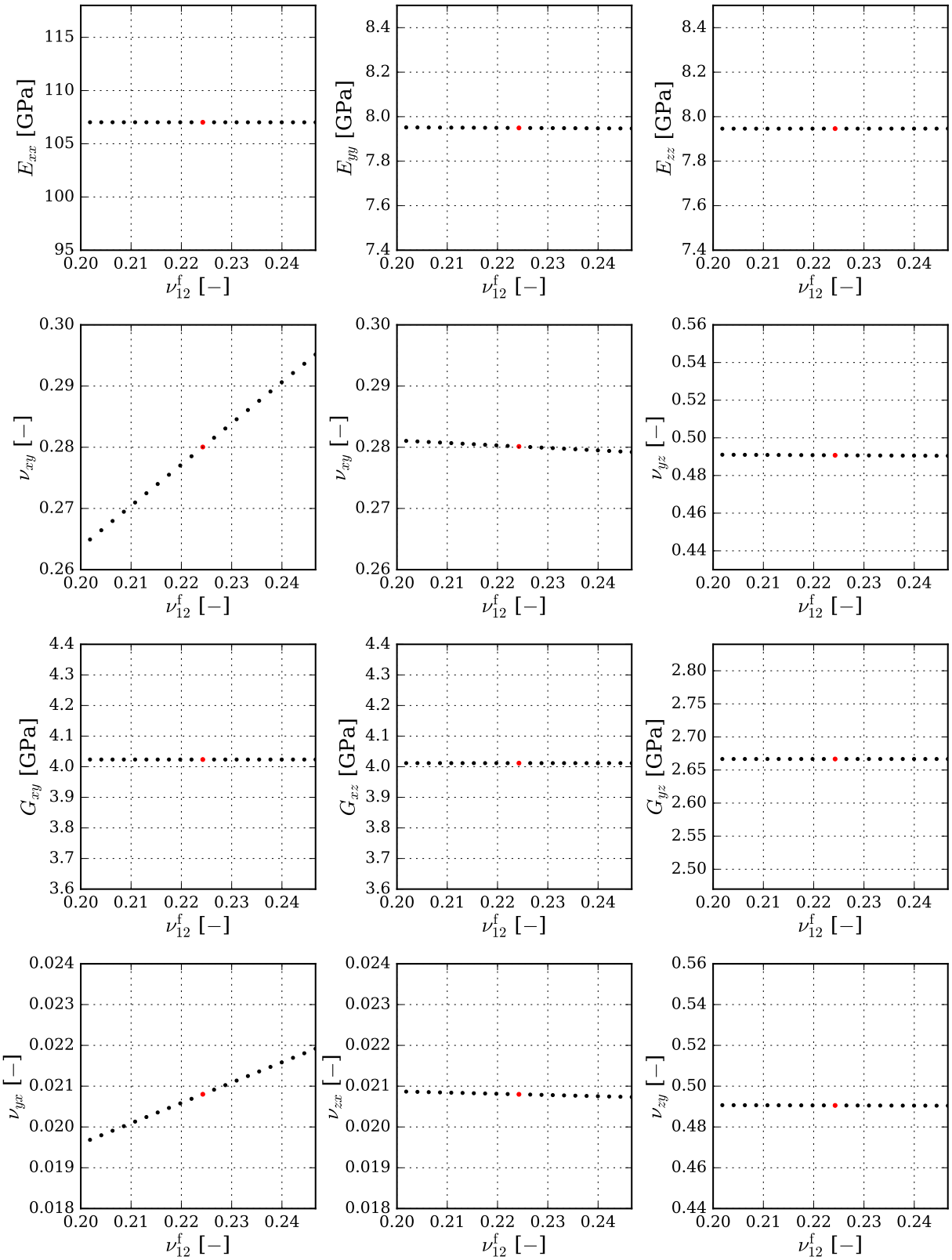

Figure 5.25: Sensitivity of homogenized material properties to variation of Poisson's ratio fibers ν_{12}^{f}.

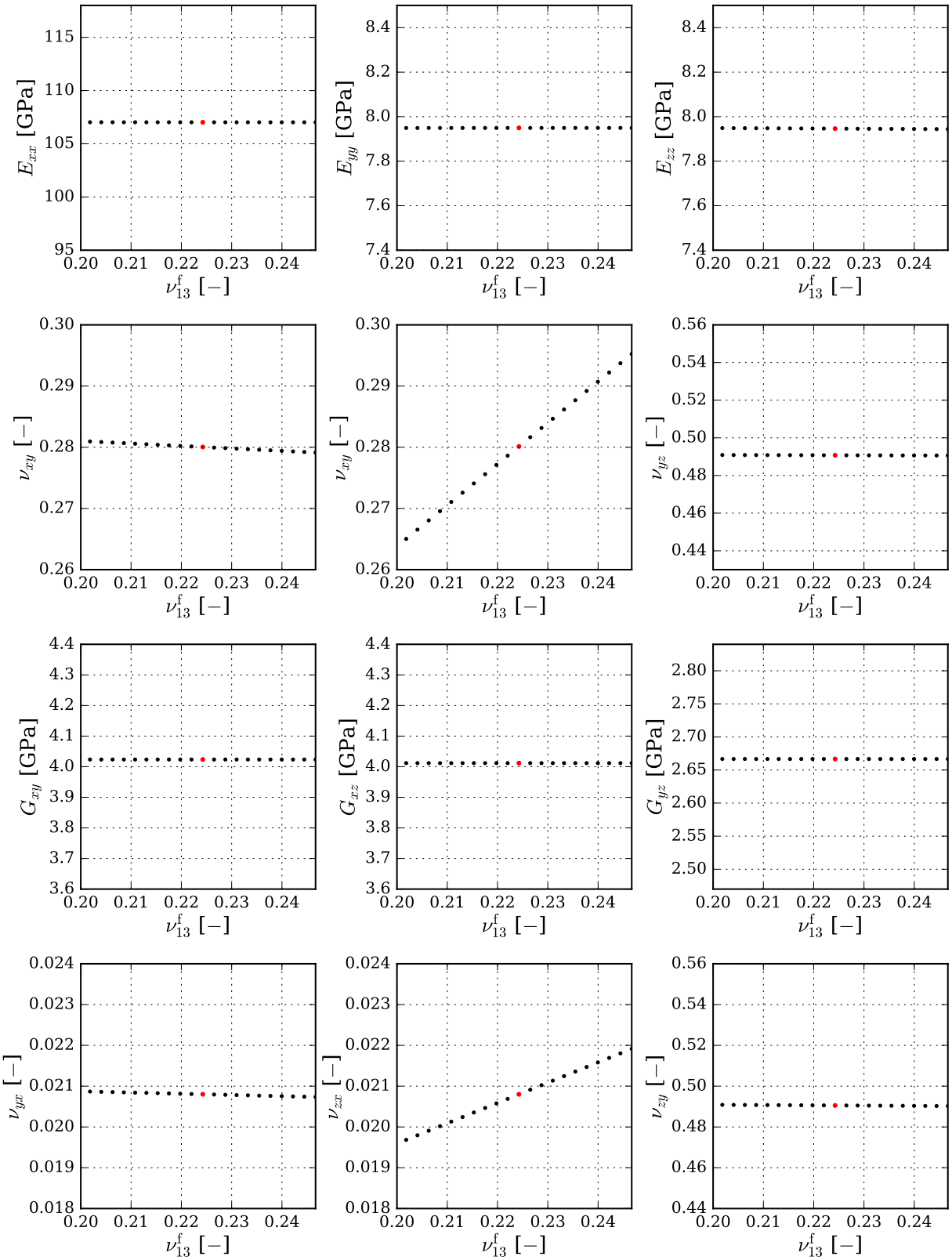

Figure 5.26: Sensitivity of homogenized material properties to variation of Poisson's ratio of fibers ν_{13}^{f}.

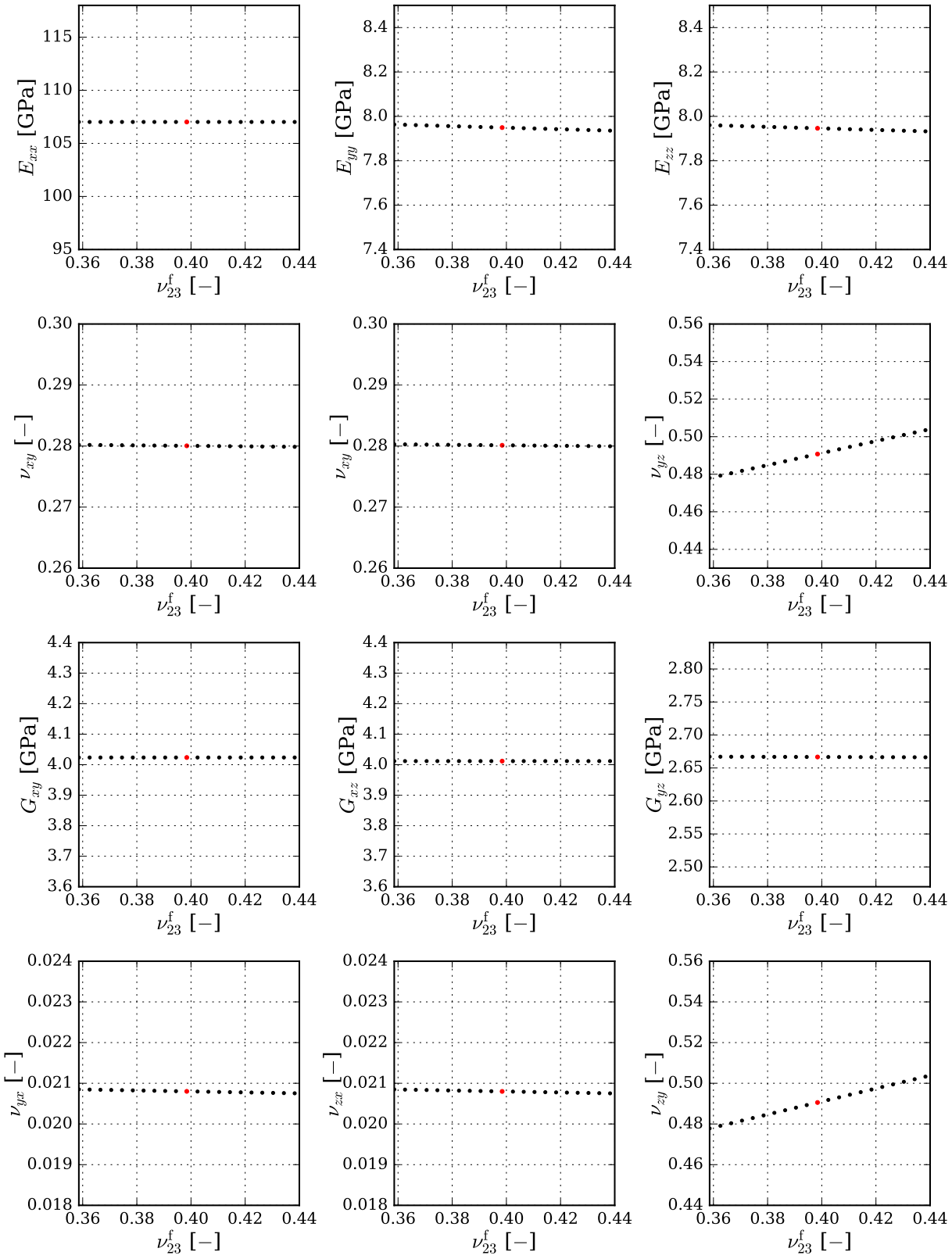

Figure 5.27: Sensitivity of homogenized material properties to variation of Poisson's ratio of fibers ν_{23}^{f}.

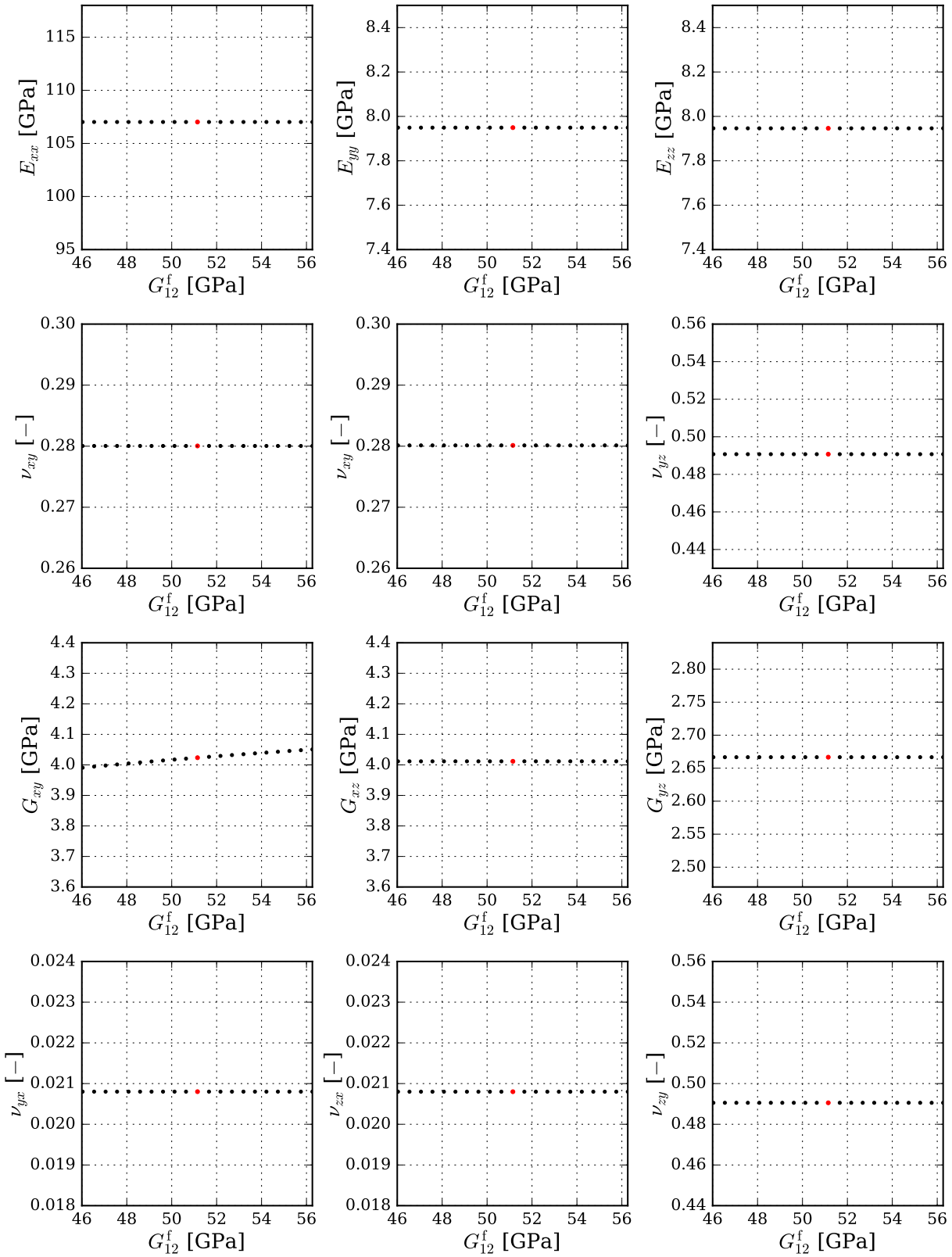

Figure 5.28: Sensitivity of homogenized material properties to variation of shear modulus of fibers G_{12}^{f}.

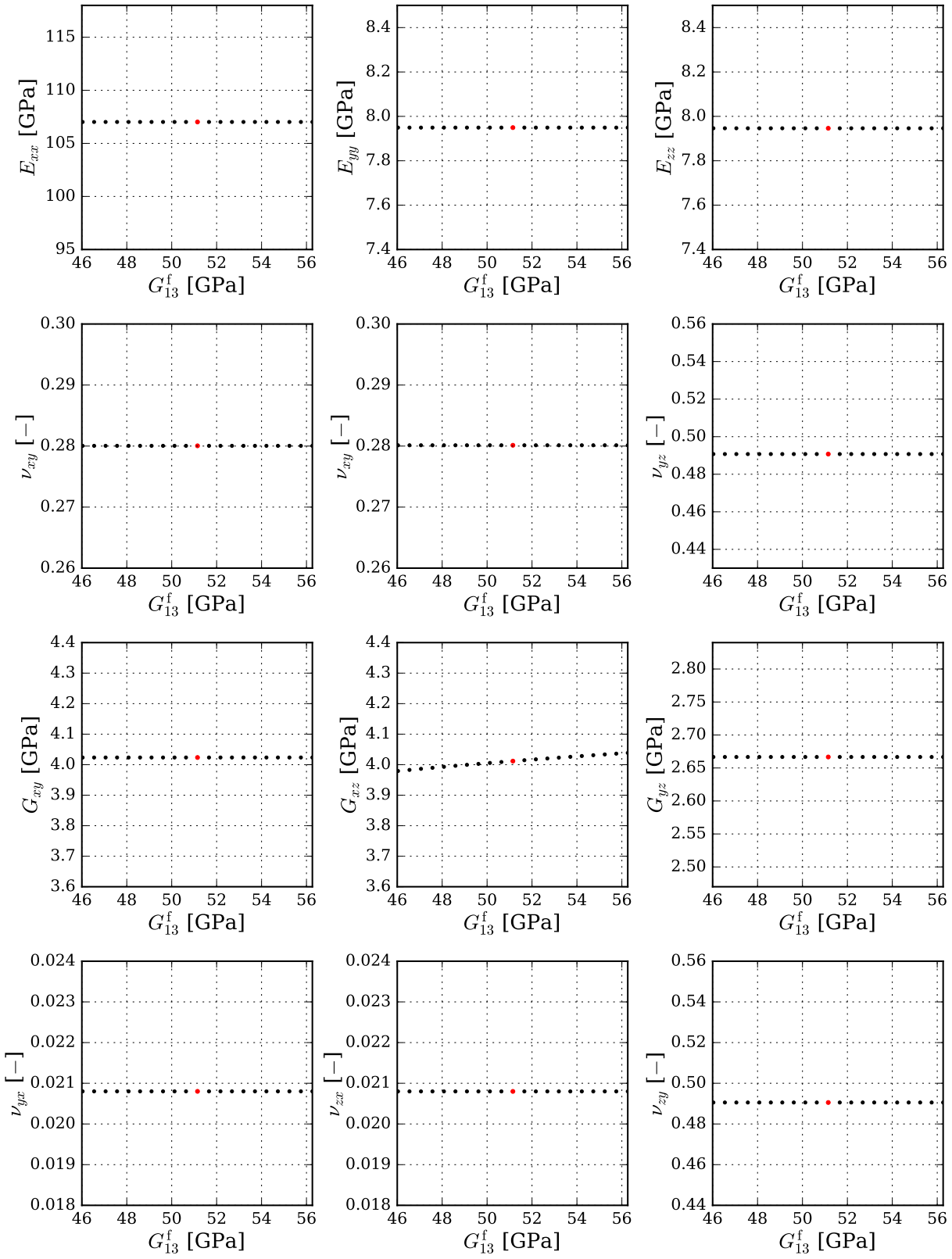

Figure 5.29: Sensitivity of homogenized material properties to variation of shear modulus of fibers G^{f}_{13}.

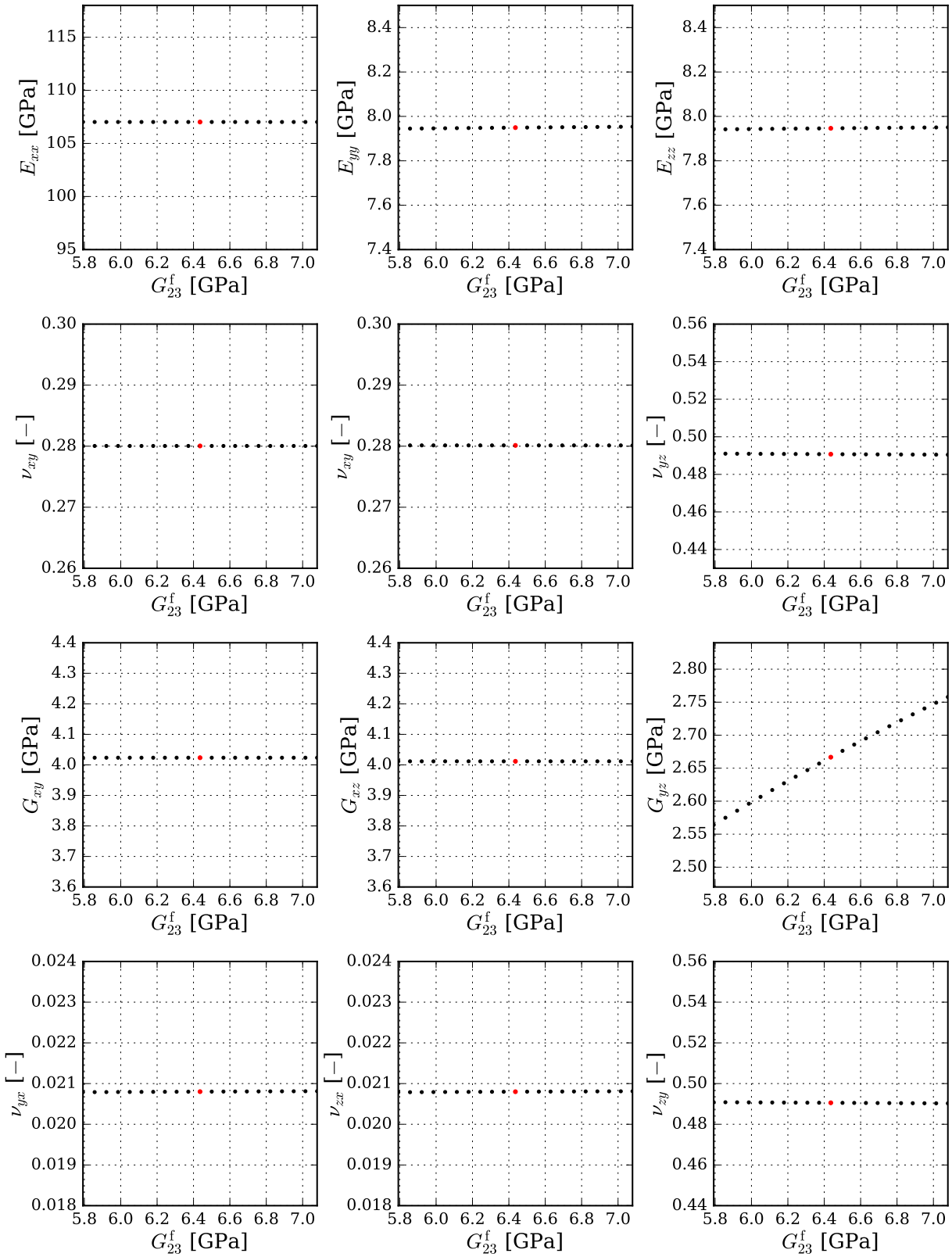

Figure 5.30: Sensitivity of homogenized material properties to variation of shear modulus of fibers G^{f}_{23}.

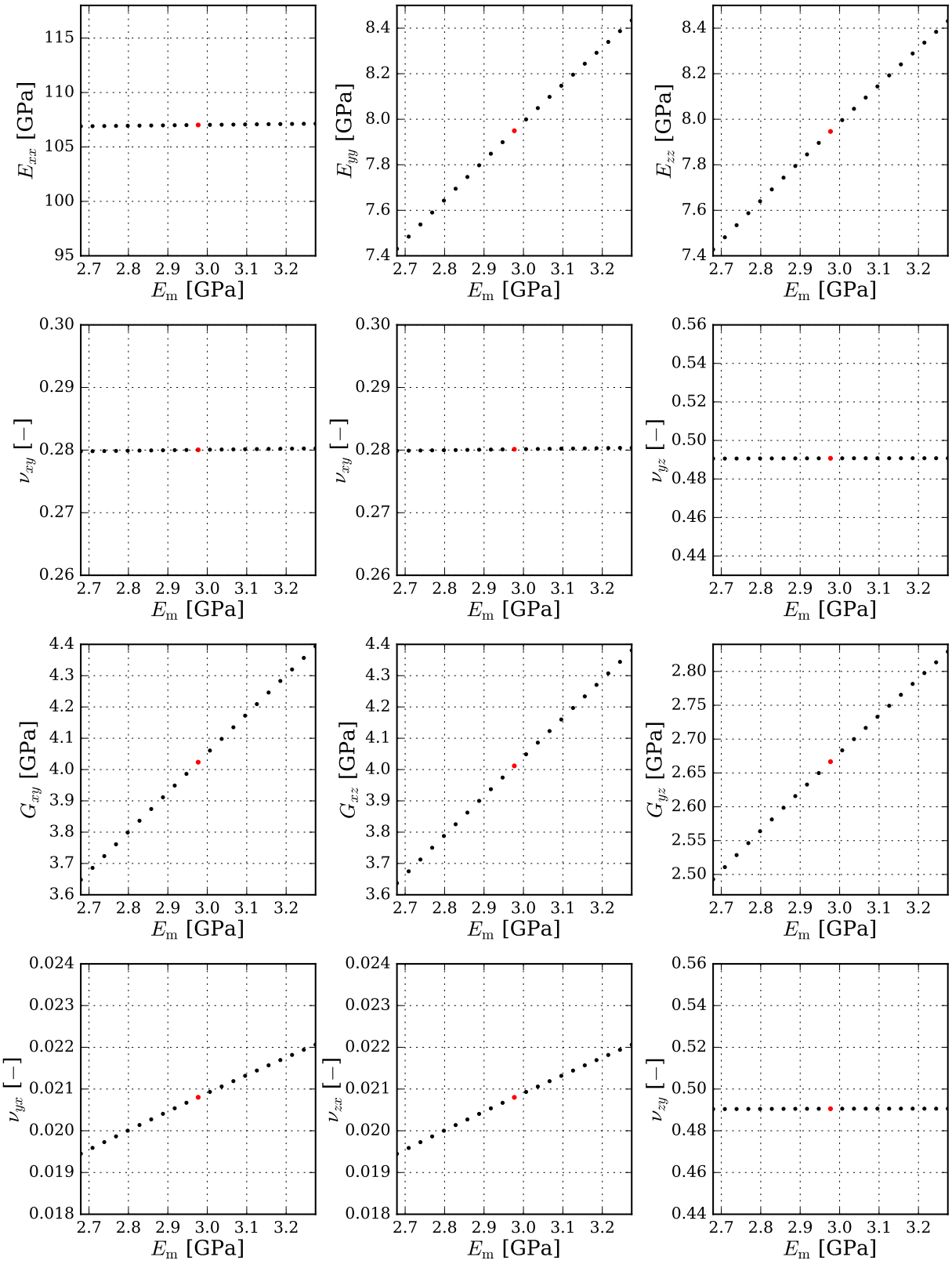

Figure 5.31: Sensitivity of homogenized material properties to variation of Young's modulus of matrix E_{m}.

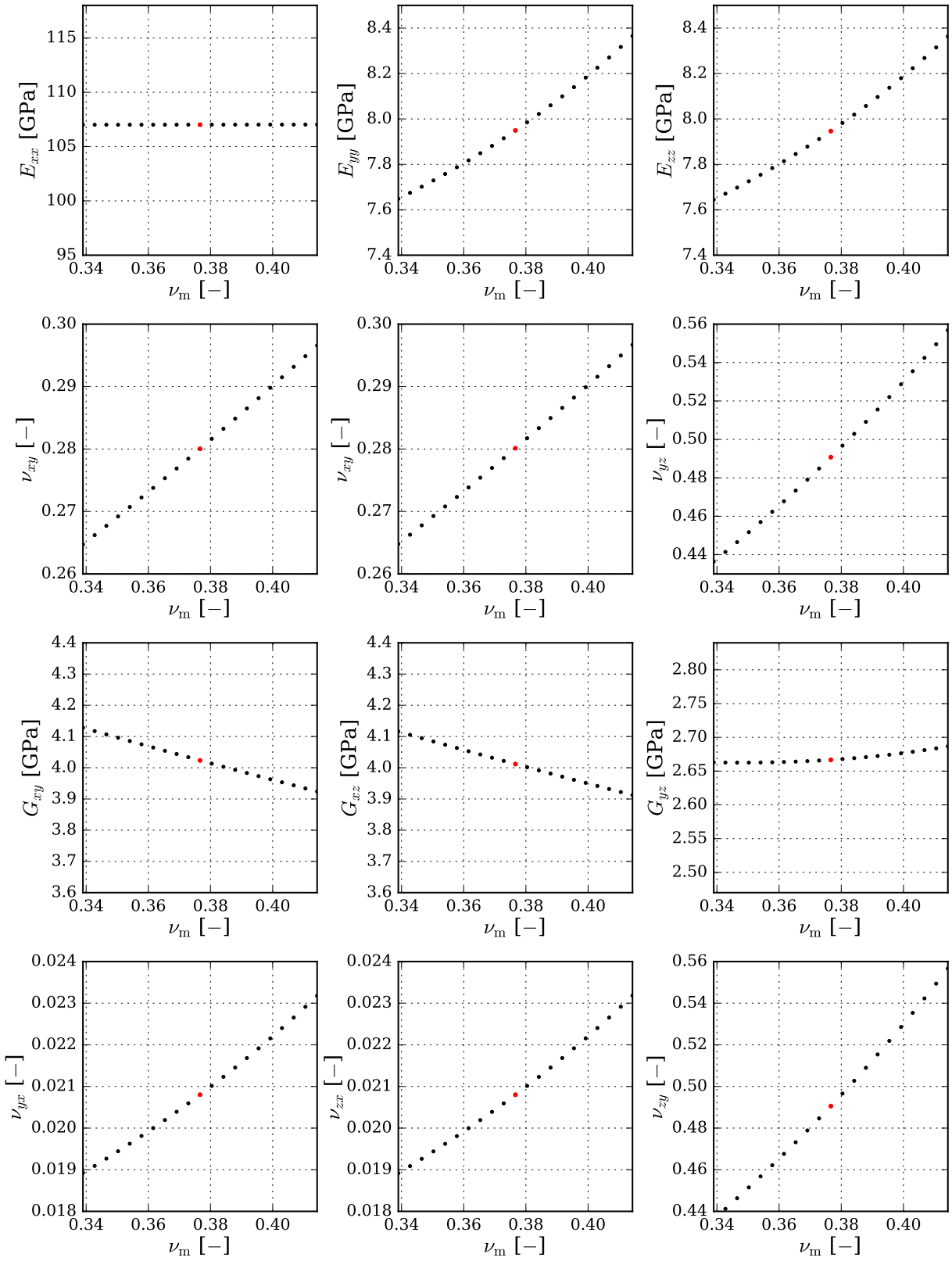

Figure 5.32: Sensitivity of homogenized material properties to variation of Poisson's ratio of matrix ν_{m}.

5.9.4 Sensitivity of Stress/Strain Dependencies

Micromodel with regular fiber distribution and nonlinear material models was subjected to analysis of sensitivity of stress/strain dependencies to material parameter variation using the OAT method. The material parameters were variated in range ± 10 % with a step of 1 % of the values identified in section 5.5.2 and shown in Tab. 5.2.

Results of selected material parameter variations are depicted in Figs. 5.33 to 5.39. Performed analysis gives the information, which stress/strain dependency in terms of fiber orientation θ (Fig. 2.1) is influenced by variation of each material parameter.

All the material parameters have certain influence on the resulting numerically obtained stress/strain dependencies. But the numerically obtained stress/strain dependencies do not significantly change with a particular parameter variation, therefore the proposed material models were assumed to be appropriately sensitive. Suitability of the proposed material models is also proven by the fact, that only a single combination of material parameters of the micromodel phases was found during the calibration process (section 5.5.2). The optimization process always converged to the same minimum of the objective function (5.30). The ability of the micromodel to simulate experimentally obtained stress/strain dependencies (Fig. 5.16) also supports the claim that the material models were proposed appropriately.

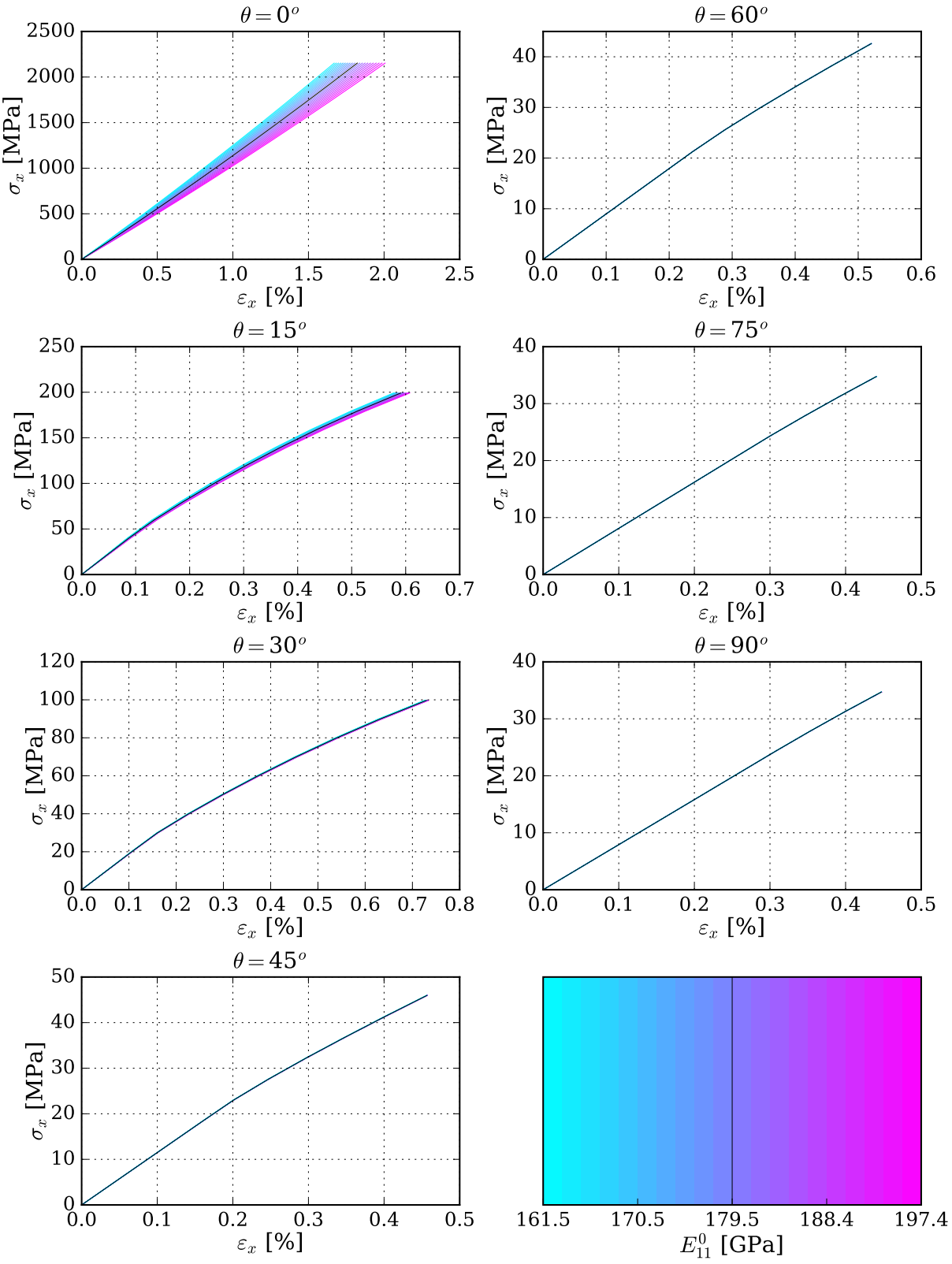

Figure 5.33: Force/displacement dependencies for variating parameter of fiber E_{11}^0 in case of unit cell **a**.

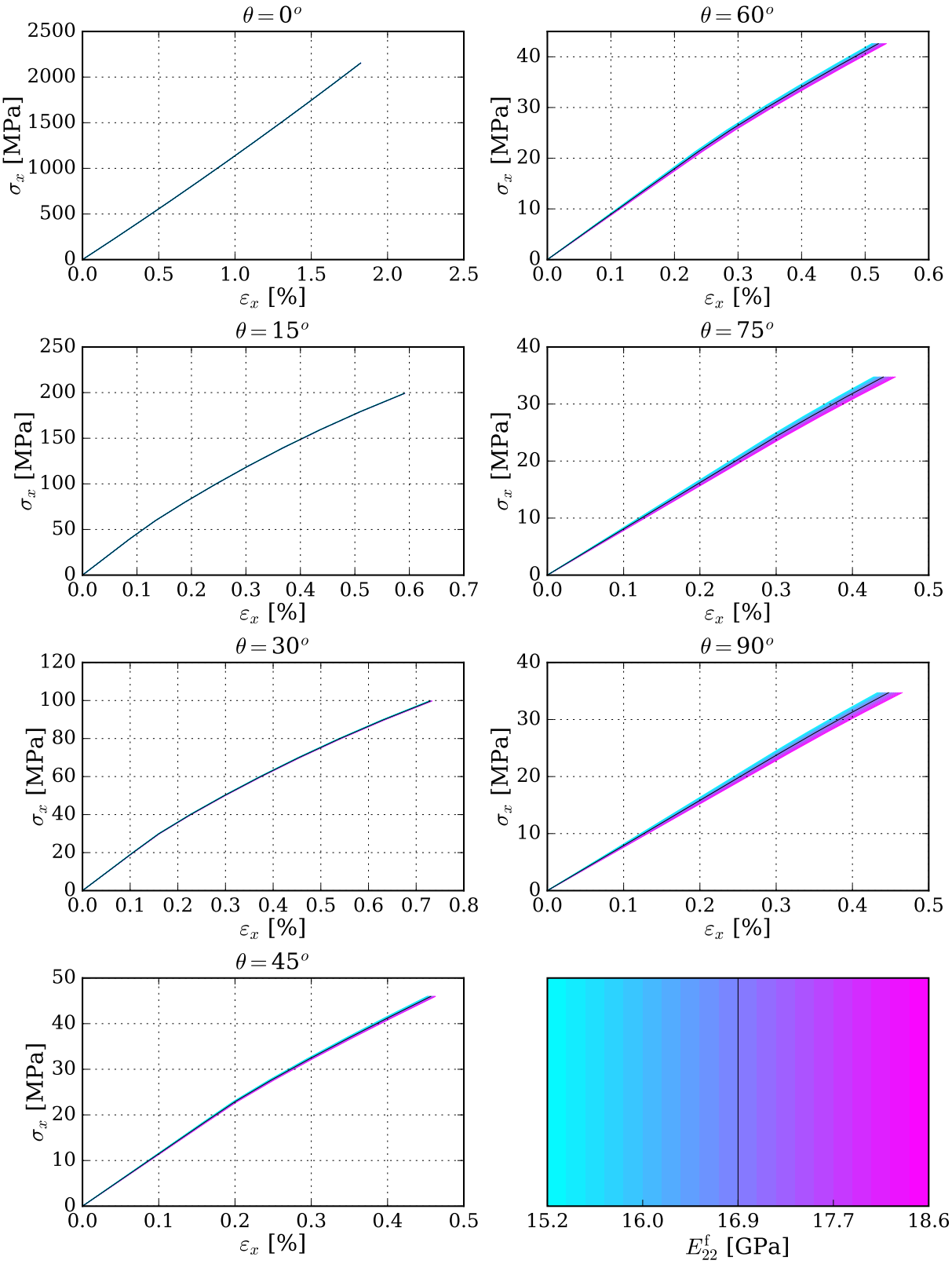

Figure 5.34: Force/displacement dependencies for variating parameter of fiber E_{22}^{f} in case of unit cell **a**.

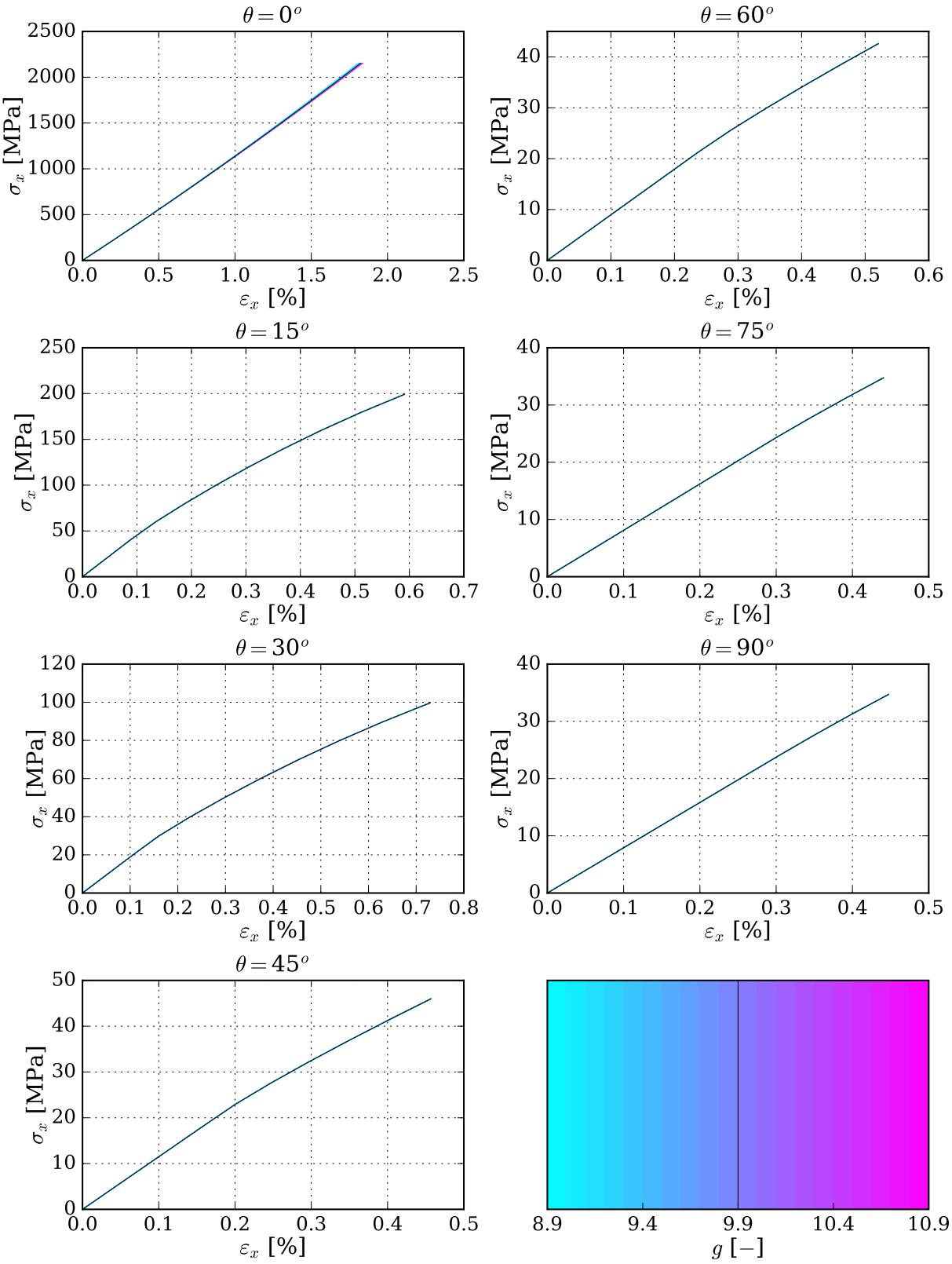

Figure 5.35: Force/displacement dependencies for variating parameter of fiber g in case of unit cell **a**.

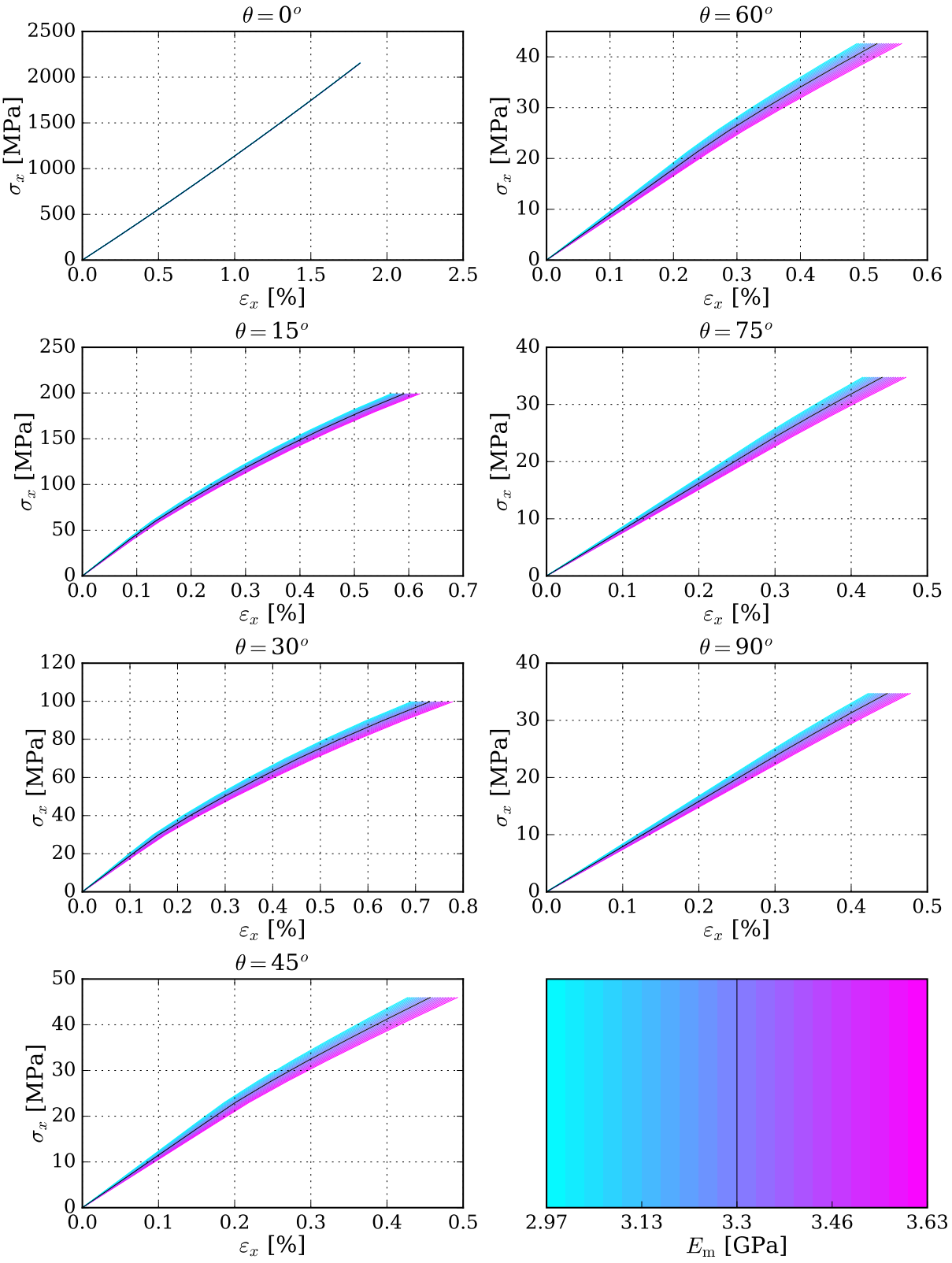

Figure 5.36: Force/displacement dependencies for variating parameter of matrix E_{m} in case of unit cell **a**.

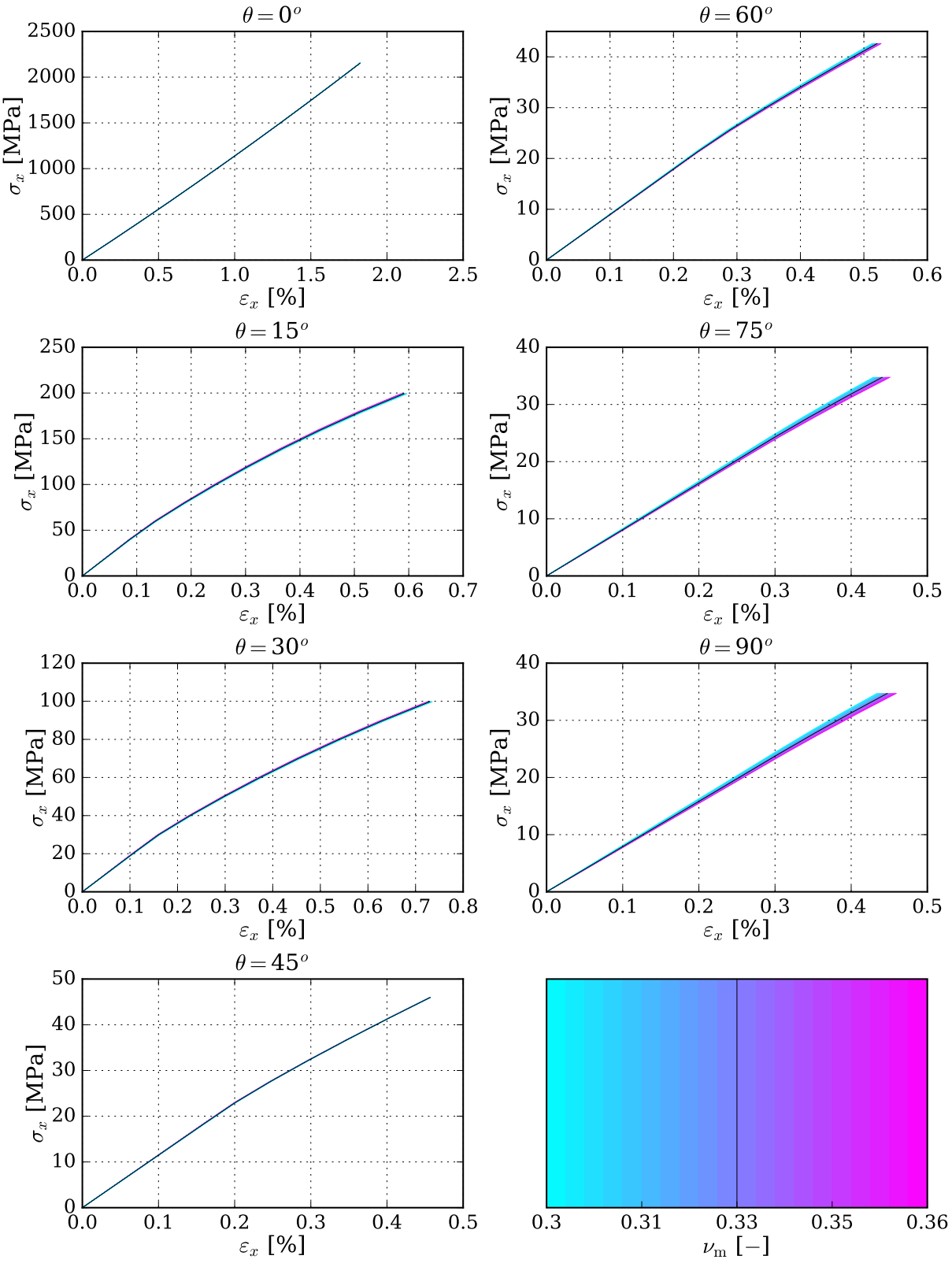

Figure 5.37: Force/displacement dependencies for variating parameter of matrix ν_{m} in case of unit cell **a**.

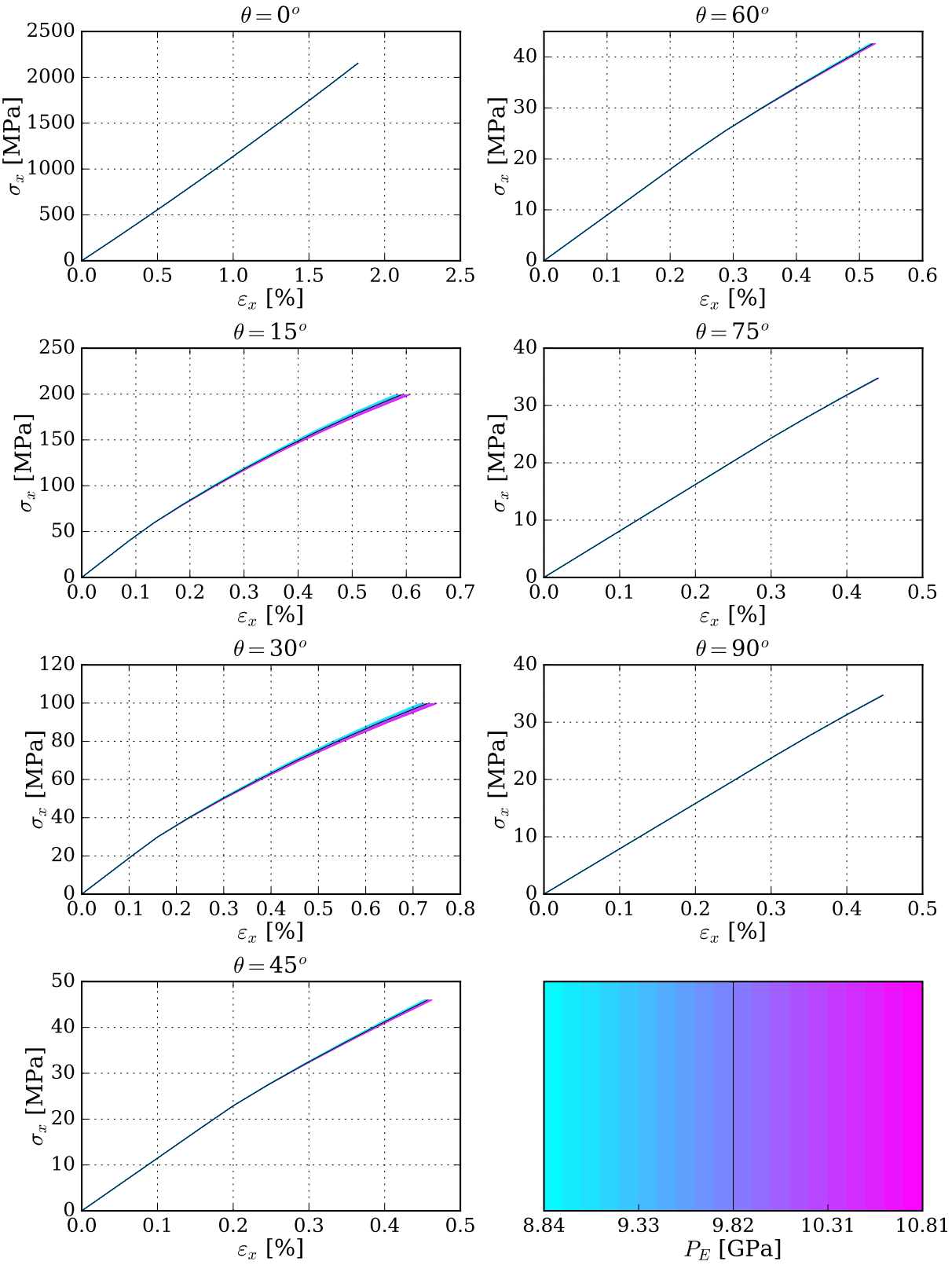

Figure 5.38: Force/displacement dependencies for variating parameter of matrix P_E in case of unit cell **a**.

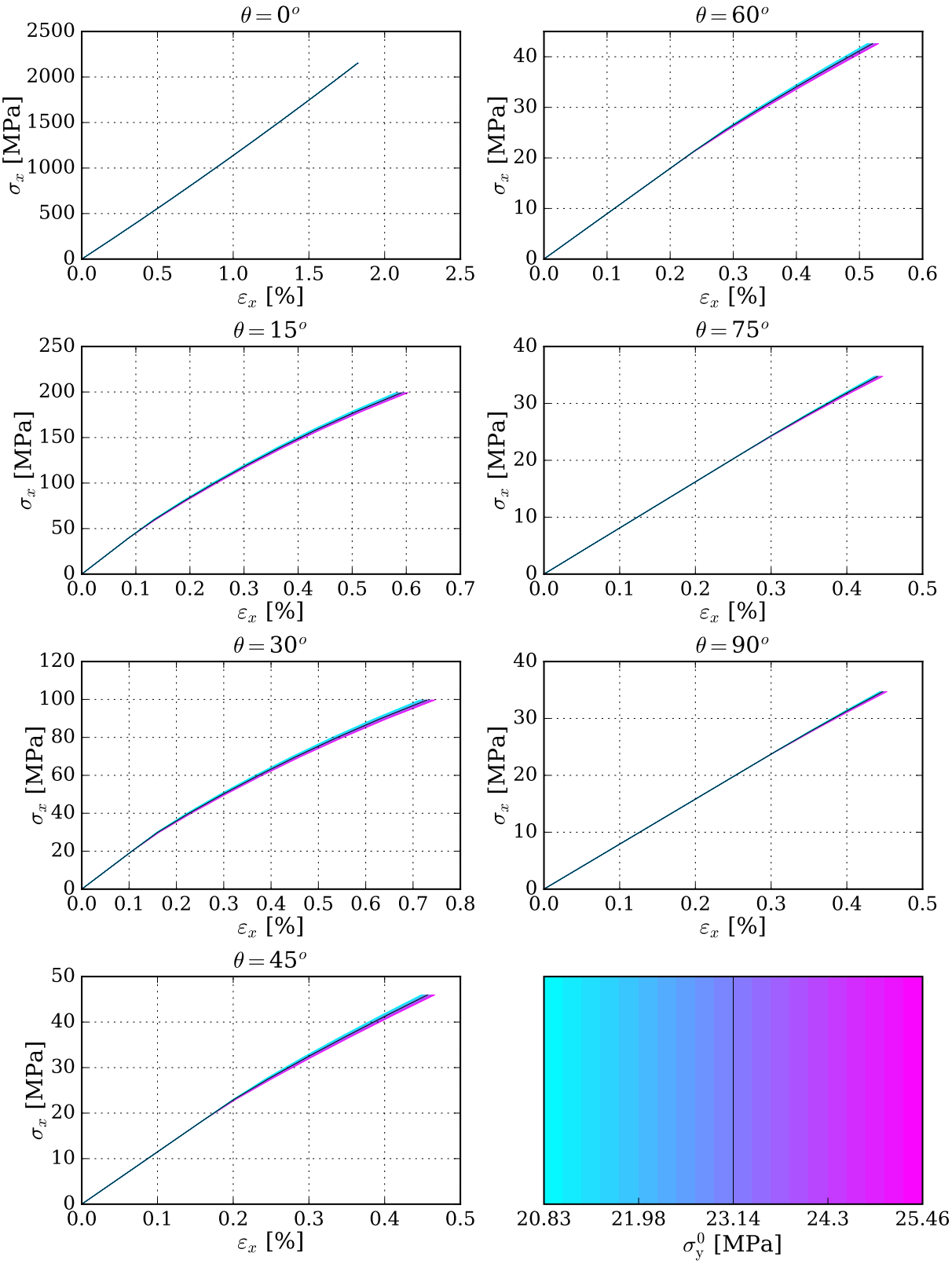

Figure 5.39: Force/displacement dependencies for variating parameter of matrix σ_y^0 in case of unit cell **a**.

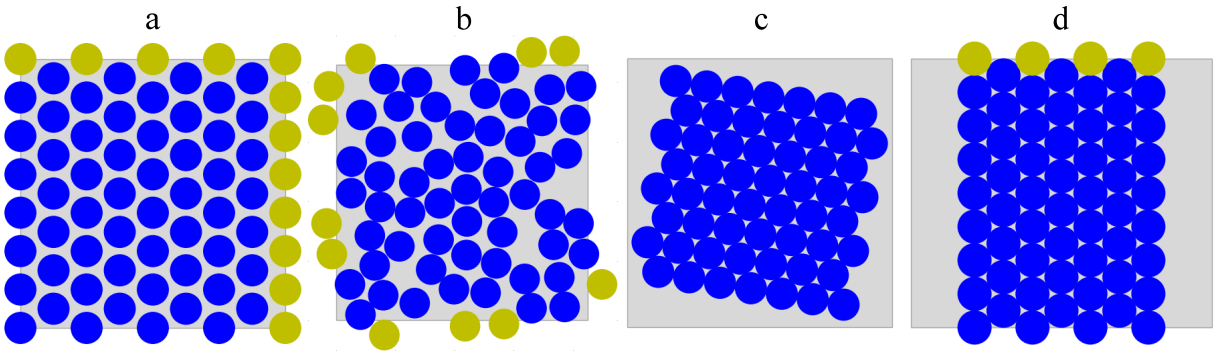

Figure 5.40: Geometries of unit cells subjected to comparison of homogenized material properties in rotated global coordinate systems (xyz).

5.10 Degree of Anisotropy Analysis

Homogenized material properties of unit cells with different geometries were identified to express the degree of anisotropy of proposed micromodels. The homogenized properties were calculated in rotated coordinate systems, extremes of the identified parameters in the plane perpendicular to fibers in case of unit cells with different degrees of irregularity were compared with values of a regular unit cell to obtain the information about isotropy of the unit cells in the plane.

To analyze influence of the degree of irregularity of the micromodel geometry on the homogenized material properties, parameters of two hundred unit cells were identified. The unit cells were proposed to create as widest interval of parameter evaluating the degree of irregularity as possible. Homogenized material parameters of the rotated unit cells subjected to analysis of the degree of anisotropy were included to the graphs of influence of degree of anisotropy on homogenized material properties.

5.10.1 Comparison of Regular and Irregular Cells

Goal of this analysis was to determine degree of anisotropy (section 4.1.3) of micromodels with different geometries. Homogenized material parameters in different directions of the composite material Υ were determined and the influence of degree of irregularity of the unit cell geometry on the homogenized material parameters in the plane perpendicular to fibers was investigated to verify whether it is a plane of isotropy.

Homogenized material properties were identified for 4 unit cells – 1 with regular and 3 with irregular fiber distribution (Fig. 5.40). The analyzed unit cells have different degrees of irregularity Υ differing. The homogenized parameters were identified in global coordinate system (xyz) rotated about axis of local coordinate system (123). Micromodels were loaded in global coordinate system (xyz) rotated about (123) by angles $\varphi, \psi, \theta \in \langle 0°; 360° \rangle$ with a step of 5°.

Unit cell **a** has a regular fiber distribution, therefore the $\Upsilon = 0$. Geometry of unit cell **b** was generated by the algorithm for unit cells with random fiber distribution (Fig. 5.9).

Unit cell **c** was obtained by rotation of the cluster geometry (Fig. 5.6). Unit cell **d** is the unit cell with stripe of fibers created in section 5.2.2 and has the highest degree of irregularity Υ.

Table 5.7: Material properties of unit cell **a**.

	unit cell **a**		
	mean value	extremes	deviation
$E_{yy,zz}$	7.9486 GPa	7.946 GPa 7.951 GPa	–0.03 % 0.03 %
G_{yz}	2.6662 GPa	2.666 GPa 2.667 GPa	–0.01 % 0.03 %
ν_{yz}	0.4905	0.490 0.491	–0.1 % 0.1 %
Υ	0.0		

Table 5.8: Homogenized material properties of micromodels **b**, **c** and **d** and their deviation from mean values of micromodel **a** (Tab. 5.7) and degrees of irregularity of the unit cells.

	unit cell **b**		unit cell **c**		unit cell **d**	
	extremes	deviation	extremes	deviation	extremes	deviation
$E_{yy,zz}$	8.025 GPa 8.197 GPa	1.0 % 3.1 %	7.340 GPa 8.923 GPa	–7.7 % 12.3 %	7.052 GPa 10.544 GPa	–11.3 % 32.7 %
G_{yz}	2.717 GPa 2.751 GPa	1.9 % 3.2 %	2.402 GPa 3.064 GPa	–9.9 % 15.0 %	2.294 GPa 3.260 GPa	–14.0 % 22.3 %
ν_{yz}	0.483 0.493	–1.5 % 0.5 %	0.437 0.536	–10.9 % 9.3 %	0.372 0.558	–24.2 % 13.8 %
Υ	17.84		61.69		66.94	

Unidirectional composite is considered to be transversely isotropic material [27] – Young's modulus, shear modulus and Poisson's ratio in plane yz rotated in 23 should be constant. Homogenized material properties of unit cell **a** are depicted for global coordinate system (xyz) rotated about axis 1 (Fig. 5.43), axis 2 (Fig. 5.41) and axis 3 (Fig. 5.42). Unit cell **a** may be designated as a transversely isotropic material (section 4.1.2), since the plane perpendicular to fiber direction is a plane of isotropy (section 4.1.1). Material properties deviate from the mean values at most 0.1 % (Tab. 5.7). This corresponds with common fact that a plane having at least 3-fold symmetry may be considered as a plane of isotropy [68]. Geometry of the unit cell **a** with hexagonal fiber distribution has even 6 axes of symmetry (two 3-fold symmetry planes).

Homogenized material properties of the unit cells with irregular fiber distributions in global coordinate systems (xyz) rotated about axis 1 are depicted in Fig. 5.44 for UC **b**, Fig. 5.45 for UC **c** and Fig. 5.46 for UC **d**.

Extreme values of material properties of unit cells with irregular fiber distributions were compared to mean values of homogenized material properties of unit cell with regular fiber distribution (Tab. 5.8). Extreme values of **b** deviated in range of -1.5 % to $+3.2$ %, in case of **c** the deviations were -10.9 % to $+15.0$ % and in case of **d** -24.2 % to $+32.7$ %. The extreme values of homogenized material properties in yz deviated more with increasing degree of irregularity Υ. The micromodels with irregular fiber distribution are not transversely isotropic.

Dependencies of homogenized material properties on angle φ (Fig. 5.43 to 5.46) are all 180° periodic.

Examples of distribution of equivalent Von Mises stress in the four analysed unit cells are shown in Appendix D. The contours are plotted for all types of uniaxial stress. It is evident how the degree of irregularity influences the peak values of Von Mises stress, hence the onset of potential non-linear response if modeled (plasticity, damage or strength). The maximum value of equivalent stress increases with increasing value of Υ.

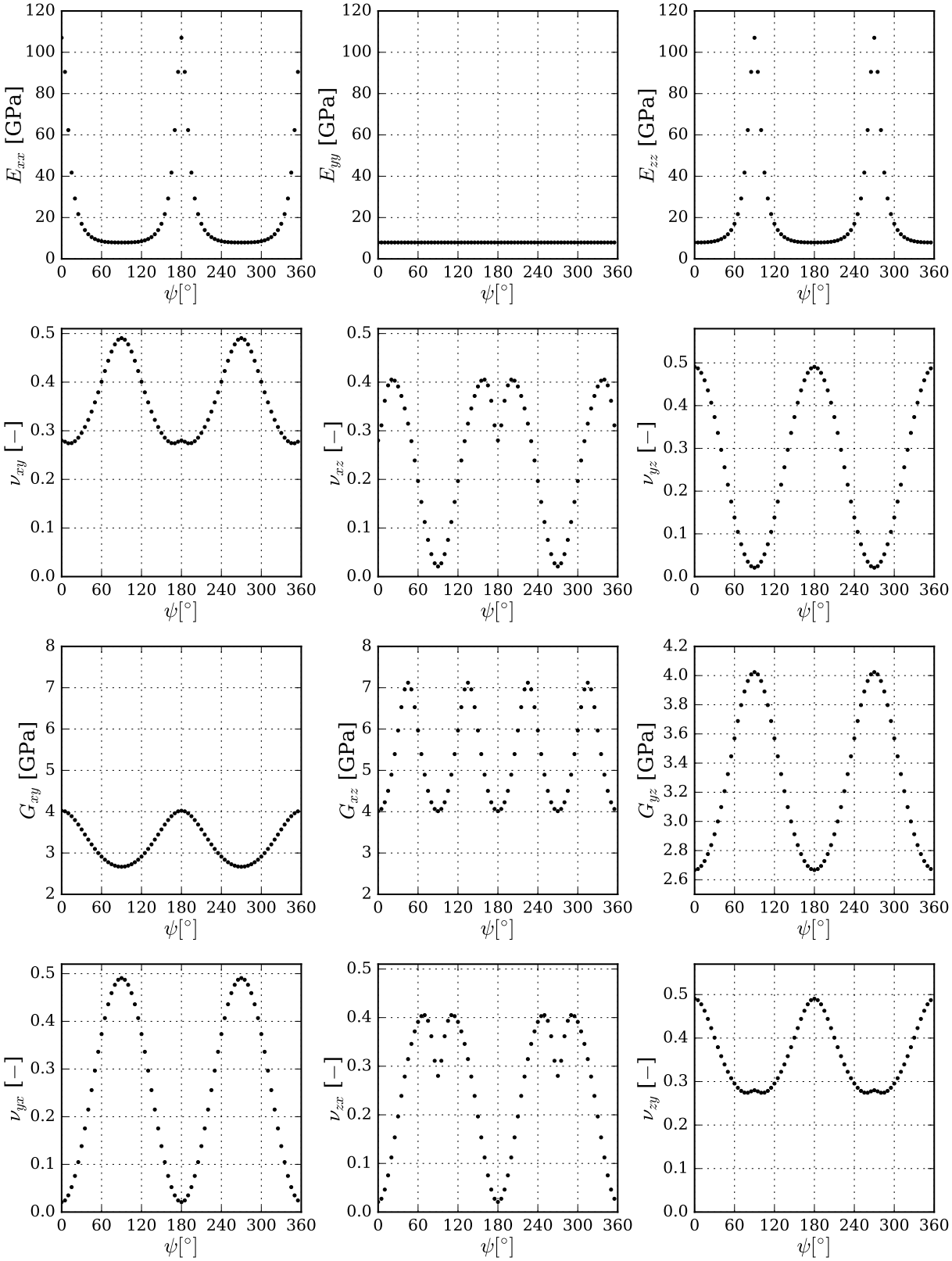

Figure 5.41: Homogenized material properties of unit cell **a** (regular) in coordinate systems rotated about axis 2.

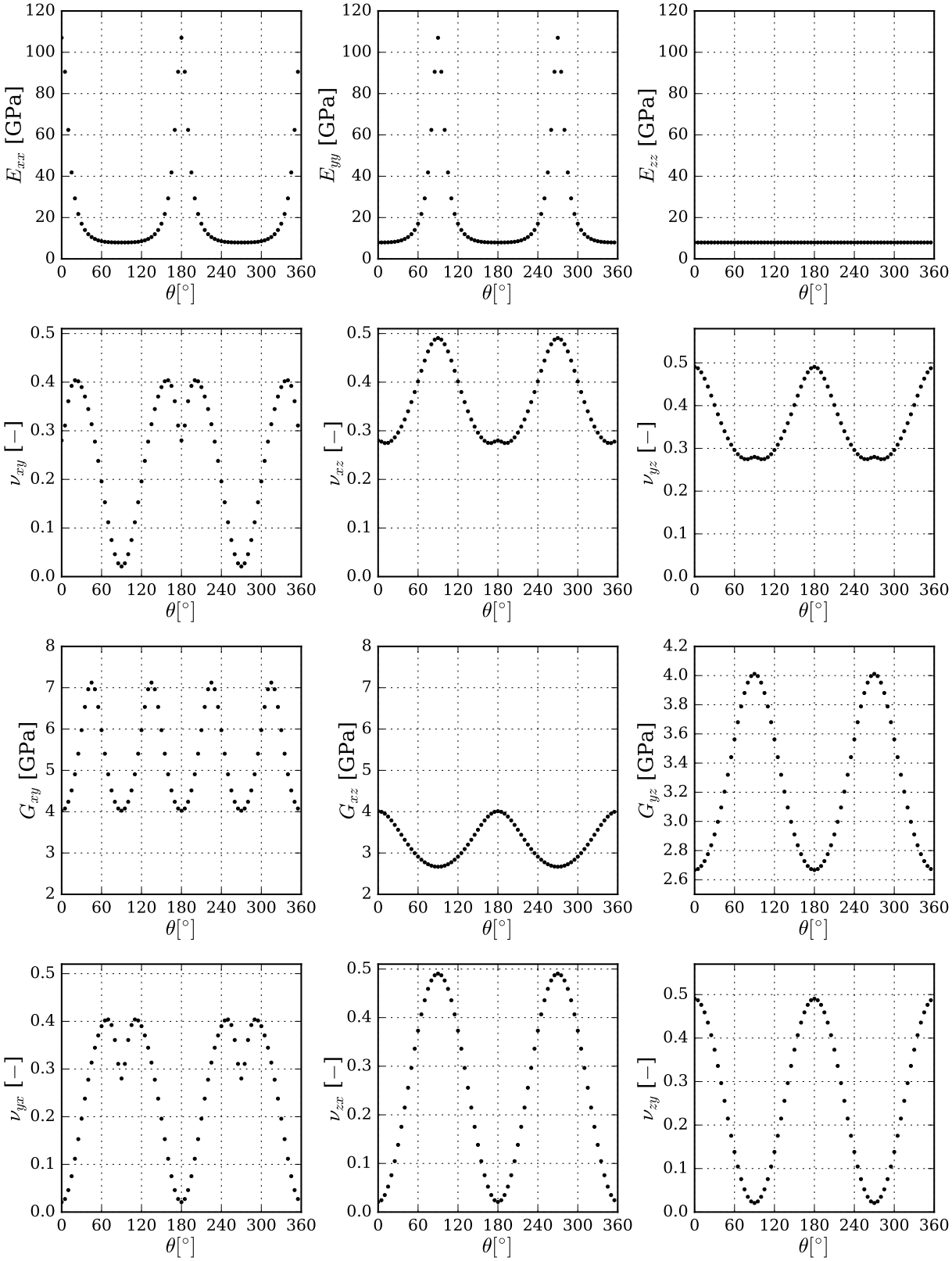

Figure 5.42: Homogenized material properties of unit cell **a** (regular) in coordinate systems rotated about axis 3.

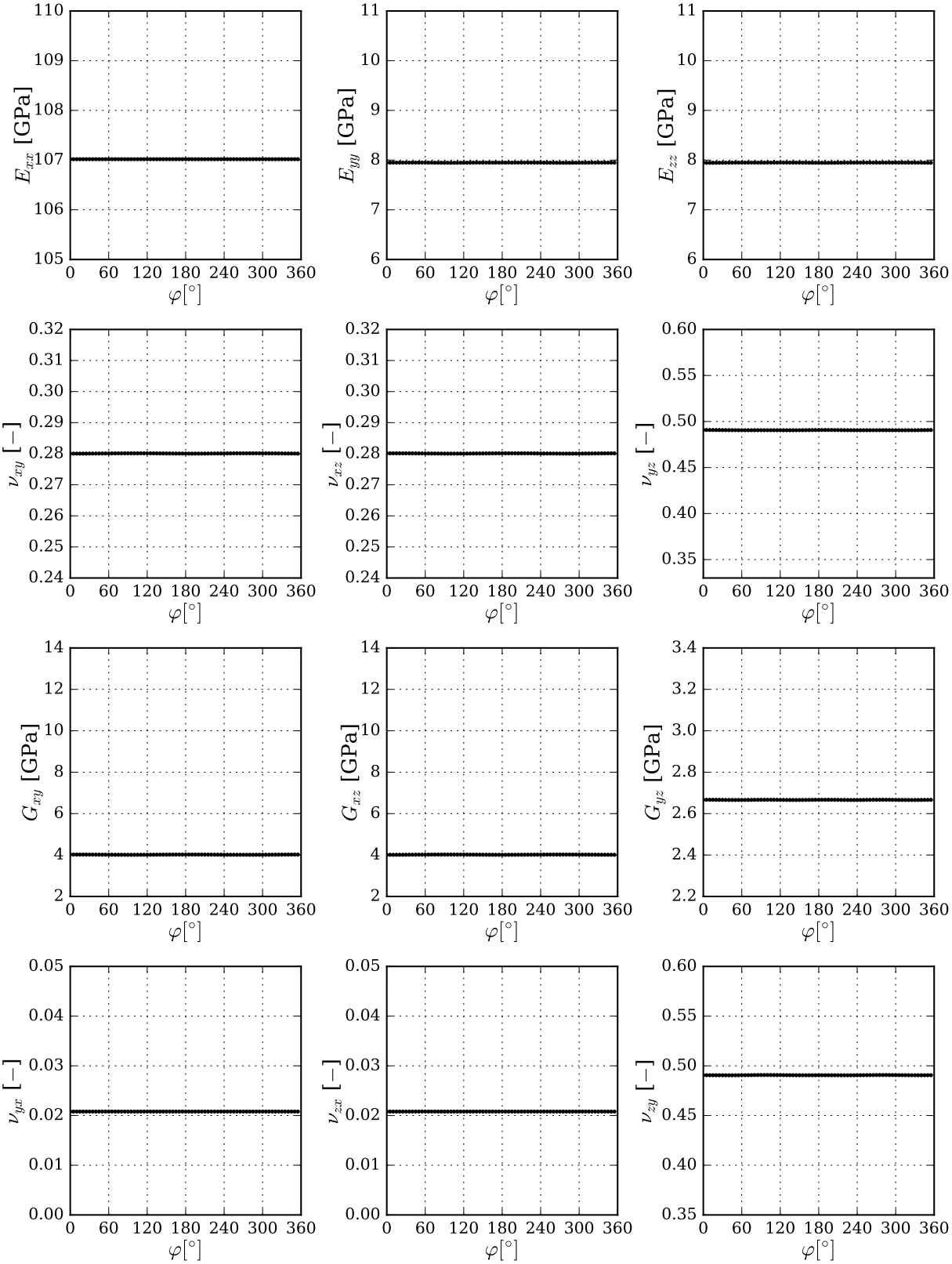

Figure 5.43: Homogenized material properties of unit cell **a** (regular) in coordinate systems rotated about axis 1.

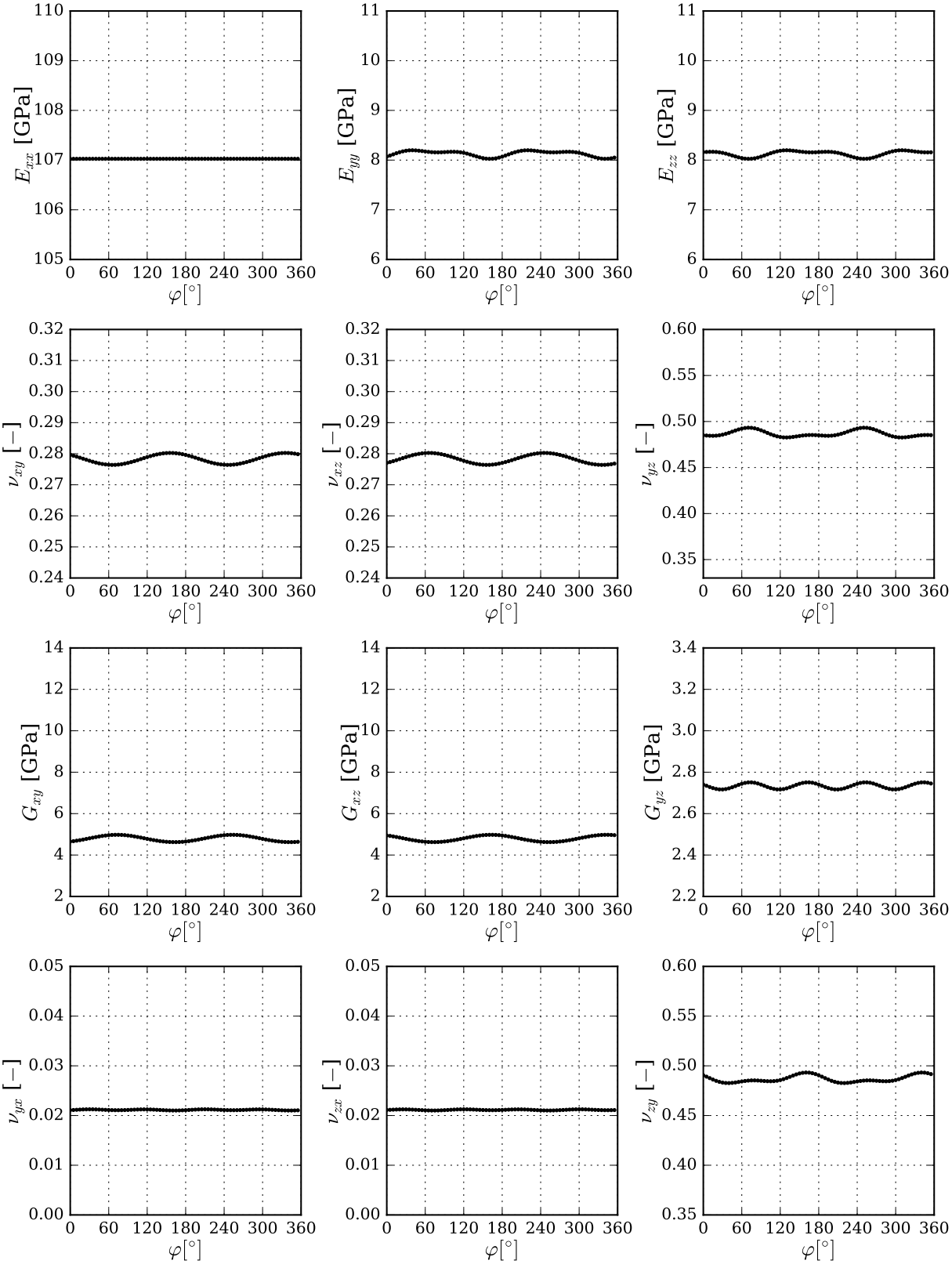

Figure 5.44: Homogenized material properties of unit cell **b** (random) in coordinate systems rotated about axis 1.

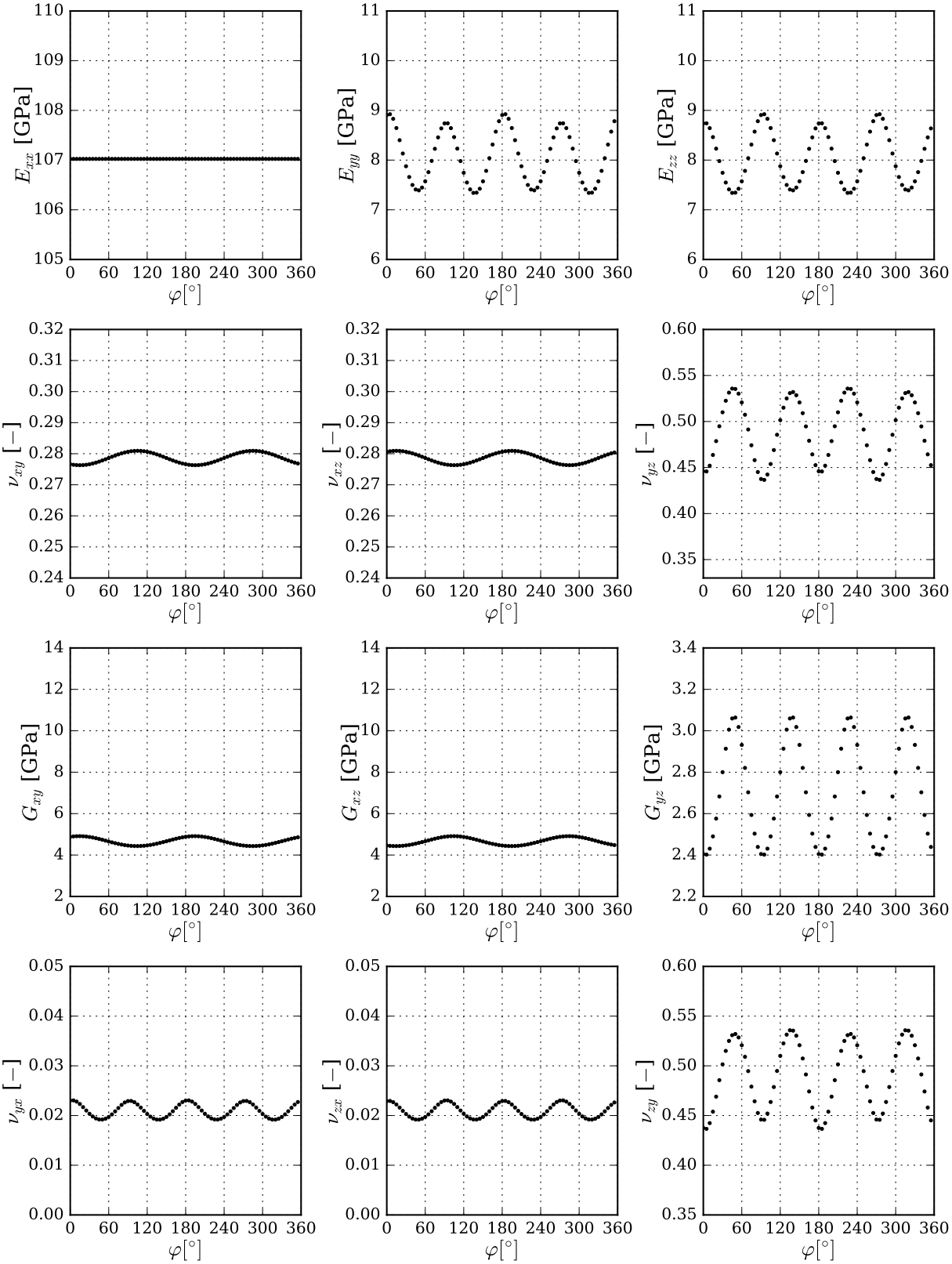

Figure 5.45: Homogenized material properties of unit cell **c** (cluster) in coordinate systems rotated about axis 1.

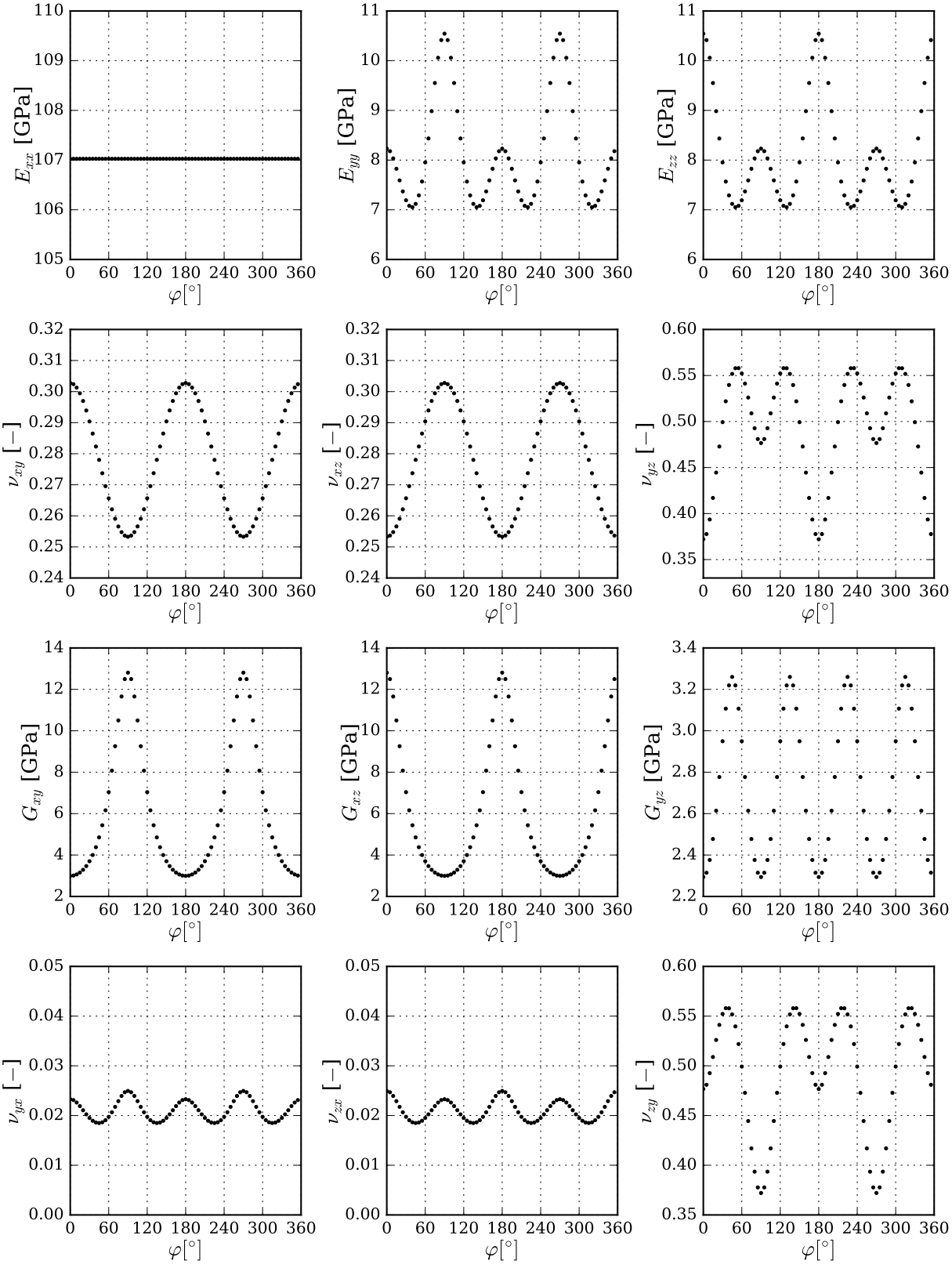

Figure 5.46: Homogenized material properties of unit cell **d** (stripe) in coordinate systems rotated about axis 1.

5.10.2 Random and Manualy Created Cells

Homogenized material properties for 200 micromodels with linear material parameters with different degrees of irregularity were identified. The unit cells had geometries with degrees of irregularity covering the interval $\Upsilon \in \langle 0; 66.9 \rangle$ (Fig. 5.47).

Half of the unit cells were created by the algorithm proposed for generating geometries of unit cells with random fiber distribution (Fig. 5.9). The empty intervals of Υ values were filled by creating additional 100 unit cell geometries manually (e.g. by increasing spaces between selected fibers of cluster unit cell or moving slightly chosen fibers of regular unit cell).

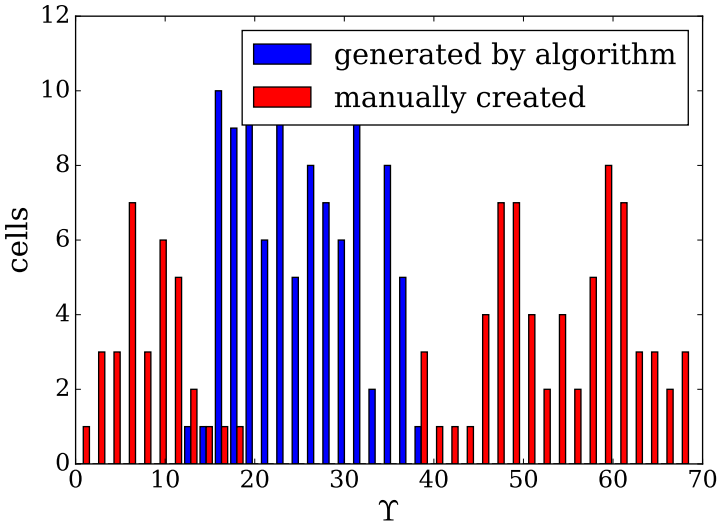

Figure 5.47: Histogram of Υ of cells created by algorithm for generating irregular geometries and manually.

It can be assumed, that the proposed parameter Υ evaluating the degree of irregularity of given geometry affects all identified homogenized material properties except the Young's modulus in fiber direction. Therefore the geometry of the micromodel cross-section has an influence on results of FEA.

All homogenized material properties have a single value for micromodel having geometry with $\Upsilon = 0$. In contrast, the micromodels of highly irregular geometry near the value of $\Upsilon = 66.9$ have dispersed homogenized properties and are highly anisotropic in the yz (23) plane. Yellow dots in Fig. 5.48 are homogenized material parameters of rotated cells **a**, **b**, **c** and **d** (section 5.10.1).

We can state, that a material with low value of Υ, can be with small inaccuracies modelled by a unit cell with regular fiber distribution (**a**). On the other hand, properties of material with high degree of irregularity expressed by Υ can not be obtained by approximating the material geometry by a unit cell with a regular uni cell without assuming the possible inadequacy.

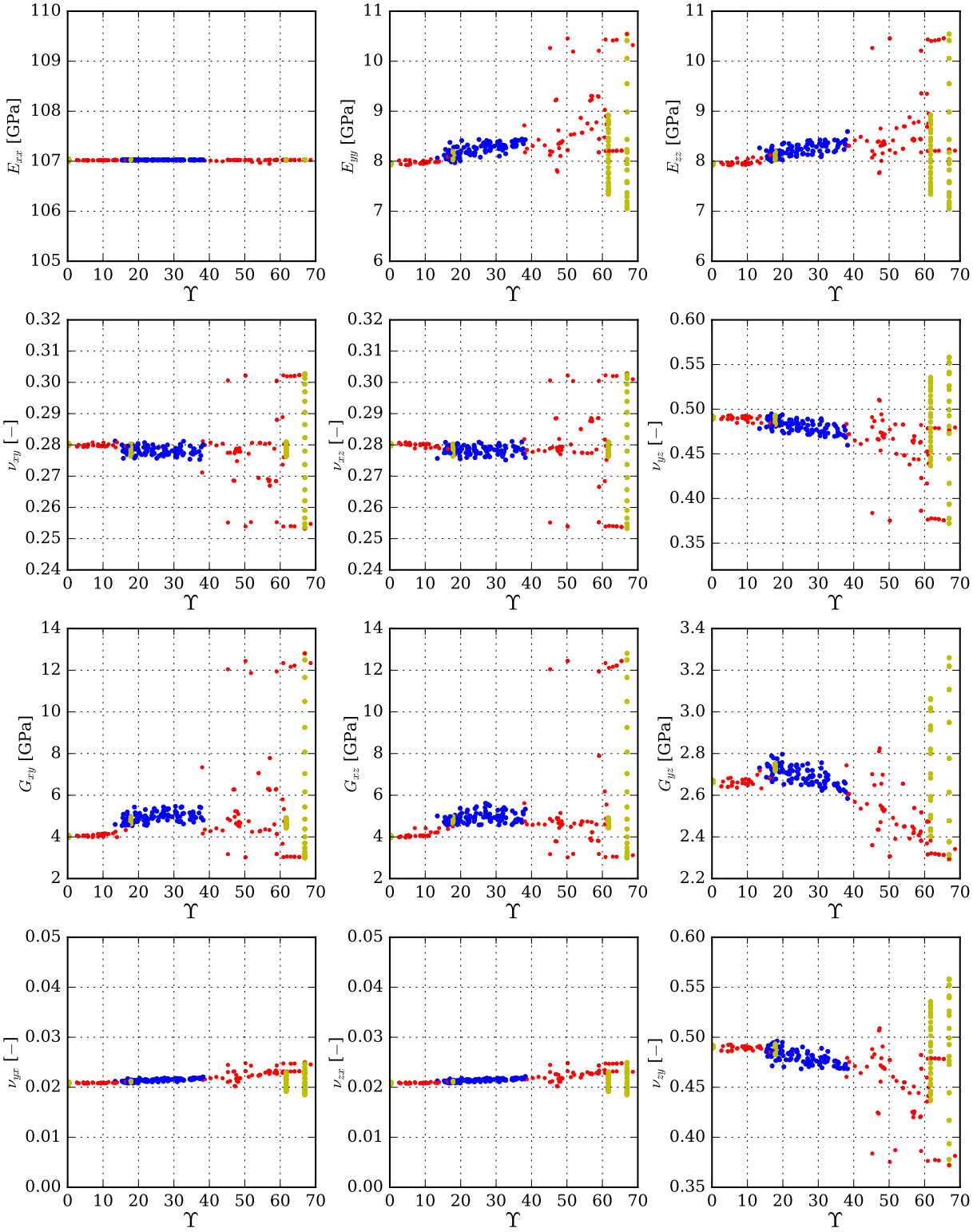

Figure 5.48: Dependency of homogenzed material properties on the value of ϒ (blue - cells generated by algorithm, red - hand made cells, yellow - cells analyzed in section 5.10.1), where unit cell **a** has $\Upsilon = 0$, **b** has $\Upsilon = 17.84$, **c** has $\Upsilon = 61.69$ and **d** has $\Upsilon = 66.94$.

Conclusions

The main result of this work is a quantification of influence of cross-section degree of irregularity on overall behavior and anisotropy of a unidirectional composite. Several steps were performed in order to obtain the analyses results.

Algorithms for automatic fiber detection from images of the composite cross-section were built in *Python*. The images were obtained by scanning electron microscopy. The identified fiber volume fractions were mostly smaller compared to fiber volume fraction given by ground truth data.

One of the main benefits of this dissertation is a script for generating periodical geometries of unit cells with random fiber distribution in the cross-section. The script enables to obtain a periodic geometry similar to a cross-section of a unidirectional composite.

Geometry of unit cell is then built, periodical boundary conditions are prescribed and given combination of linear or nonlinear material models is proposed for the composite substituents of the micromodel. Material parameters of the micromodel were calibrated according to experimental tensile tests. The loadings are chosen with respect to the type of chosen analysis and the results of analysis evaluated, eventually compared to the experimentally obtained data.

A parameter Υ evaluating the degree of irregularity of the cross-section geometry was proposed. It is suitable for evaluating both, the non-periodic geometry of the real composite and the periodic unit cells built for micromodel. Homogenized material parameters of 200 proposed micromodels with geometries spread on the largest found interval of the parameter Υ were identified. A dependence between the parameter Υ and the range of the resulting homogenized parameters was observed. The increasing value of the degree of irregularity evaluated by Υ leads to a wider interval of homogenized material parameters. The degree of irregularity of fiber distribution in the composite cross-section has therefore considerable influence on the overall material behavior and the commonly used approximation by regular fiber distribution can lead to significant inaccuracies in the results.

A tool for analyses of the unidirectional carbon fiber composite considering the irregularities in its cross-section was created. It enables automatic evaluation of the composite geometry from images. Micromodels with geometries with parameters of the identified material geometry are automatically built and finite element analysis performed to identify overall properties or to obtain response of the micromodel in form of stress-strain dependencies in chosen rotated coordinate system. All listed parts of the created auto-

matic tool for performing all the steps leading to results of finite element analysis is driven by scripts built in *Python*. Finite element analysis is performed in *Abaqus/CAE* and the results depicted using *ploTRA*, library of functtions written in *Python*.

In addition, experimental analysis of the influence of specimens width, tab material and length on convenient tensile test process in case of specimens loaded in fiber direction was performed. The analysis resulted in a specific combination of specimen width and tabs material and length. Tensile tests of epoxy resin were also performed and the observed elastoplastic behavior was considered during material models assignment when the micromodels of the composite material were built.

All goals set in the authors dissertation theses were fulfilled in this work.

In future work the material model for matrix could be expanded by the damage of viscoelastic behavior, which would enable more accurate simulation of the cyclic tensile tests. Another option is to consider interface layer between fiber and matrix. It can be modelled using cohesive contact or an additional layer of interface material could be added. The used approach could be applied in case of modelling particle composites with the objective of obtaining the microstructure morphology influence on material anisotropy.

Appendices

Appendix A

Tensile Test Configuration Analysis

A.1 Specimen Preparation

In previous author's work, failures during simple tensile tests (2.2) and cycling tensile testing ocurred in the tab area. The failures of unidirectional long-fiber composite with high-modulus carbon fibers loaded in fiber direction were caused by detachment of tab before the load reached the specimen reached the specimen strength or the specimen failed inside the tabs. According to ASTM standard test method D 3039/D 3039 M [44], the force introduction into the tested material are supposed to be reexamined (section 2.1).

Therefore, specimens (Fig. 2.2, Tab. 2.2) with failure modes marked with first character **G** – grip/tab, failure areas marked with second character **I** – inside grip/tab and failure locations marked with third character **A** – grip/tab should be eliminated. In this work the aim was to produce the biggest possible fraction of failures in gage section (second character **G**) in a sample population subjected to simple tensile tests or cyclic tensile tests. 60 specimen configurations were proposed to find the best combination of specimen geometries and tab materials and geometries (Tab. A.1).

Table A.1: Specimens and tabs properties.

specimen width	[mm]	5, 10, 15, 20, 25
tab length	[mm]	36, 56, 76
tab material		aluminium, steel, tested material, glass fiber textile

First, plates for each set of tab geometry and material configuration were cut from a composite laminate made of eight layers of unidirectional composite material Hexply 913C-HTS(12k)-5-40. Tab material of required length was glued to the plates with an epoxy adhesive Spabond 345 with slow hardener. This adhesive combination was chosen for its high shear strength (38 MPa on steel) and the possibility of curing at room temperature [69].

The tabs were applied using a steel clamping device (Fig. A.1) developed to attain even and a thin layer of adhesive between the tabs and composite. After a minimum of

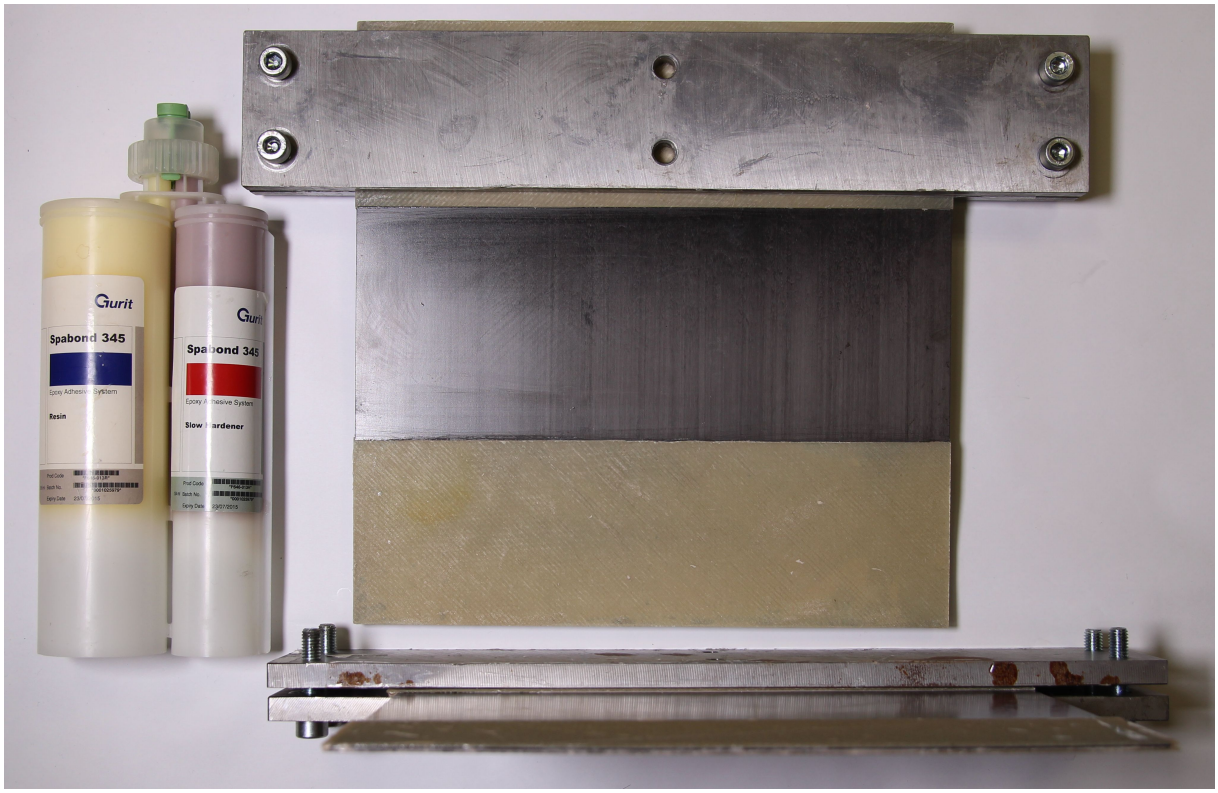

Figure A.1: Plates with steel clamping device and adhesive.

28 days of curing at room temperature the plates with applied tabs (examples of used tab materials – Fig. A.2a, examples of cut lengths – Fig. A.2b) were cut by water jet into desired specimen widths (Fig. A.4).

There were 180 specimens manufactured in this part of work – three specimens for each combination of specimen width (5 types), tab material (4 types) and tab length (3 types) configuration. Designation of the specimens is depicted in Fig. A.3. One specimen from each configuration group was subjected to simple tensile test and two to cyclic tensile test. Specimens were made of material 0.66 mm thick, distance between tabs was 100 mm.

A.1.1 Simple Tensile Tests

Specimens were loaded by simple tension with speed of 2 mm/min defined for the testing machine crosshead. The tensile force increased until the specimen failed. Data obtained from the test – loading force, gage length (50 mm) extension and time – were exported into *.TRA data files. Data were processed by a library of functions *ploTRA* in *Python*. Specimens which were subjected to simple tensile tests and reached their strength are sorted in Tabs. A.2, A.3 and A.4 according to used tab material.

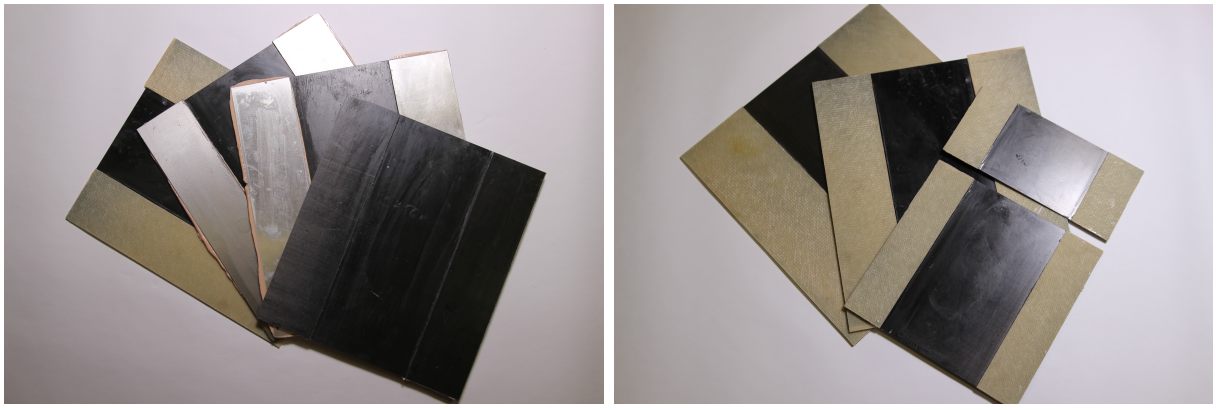

(a) Plates with all tab materials. **(b)** Plates with different tab lengths.

Figure A.2: Plates before specimen cutting.

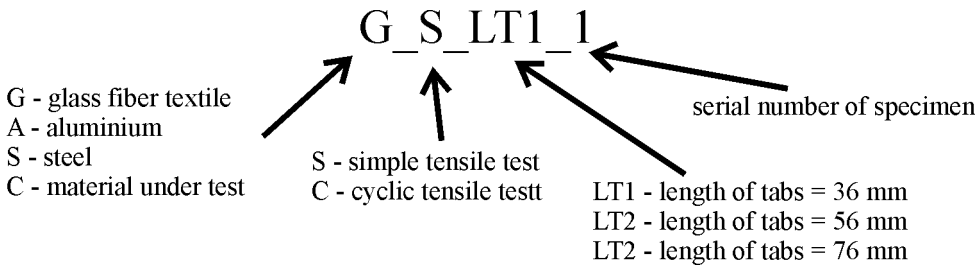

Figure A.3: Designation of specimens.

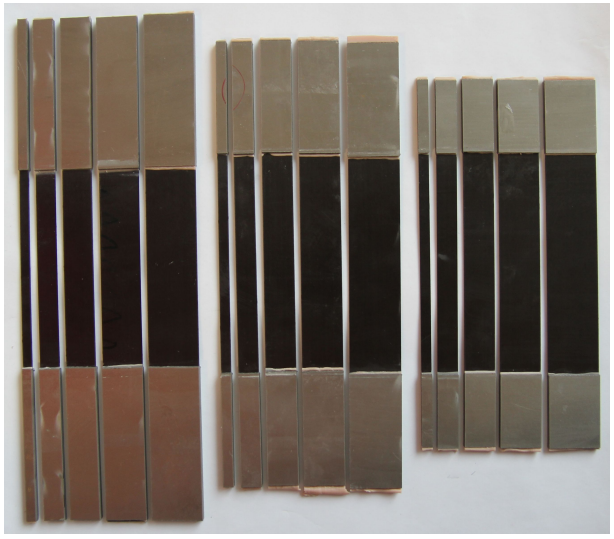

Figure A.4: Specimens with 76 mm, 56 mm and 36 mm long tabs made of steel.

Table A.2: Geometrical and material parameters of specimens subjected to simple tensile tests with tabs made of glass fiber textile.

specimen	width [mm]	$F_{\max}$ [N]	$\sigma_{\max}$ [MPa]
G_S_LT1_1	24.9	24067.3	1462.1
G_S_LT1_2	19.9	18823.3	1431.0
G_S_LT1_3	15.5	16378.4	1601.0
G_S_LT1_4	10.0	9605.0	1461.2
G_S_LT1_5	5.0	5025.2	1538.2
G_S_LT2_1	25.0	20138.2	1221.5
G_S_LT2_2	20.4	17501.9	1299.9
G_S_LT2_3	15.0	14675.3	1484.3
G_S_LT2_4	10.0	10668.1	1621.2
G_S_LT2_5	5.0	4802.3	1469.9
G_S_LT3_1	25.0	21397.9	1299.4
G_S_LT3_2	20.0	15399.5	1166.6
G_S_LT3_3	15.0	15962.1	1612.3
G_S_LT3_4	10.0	10500.8	1592.6
G_S_LT3_5	4.9	5098.3	1566.9

A.1.2 Cyclic Tensile Tests

Specimens were cyclically loaded and unloaded with test speed of 5 mm/min defined by the testing machine crosshead. Each loading part of a cycle ended when the extension of gage length reached a prescribed value. This value was $\Delta l = 0.01$mm in the first cycle and increased in every following cycle by 0.01 mm up to the specimen failure. After reaching this value, unloading started until the force dropped to 100 N (to avoid buckling). The loading/unloading process on a time scale is shown in Fig. A.5. Specimens which were subjected to cyclic tensile tests and were loaded until failure are sorted in Tabs. A.5, A.6 and A.7 according to tab material.

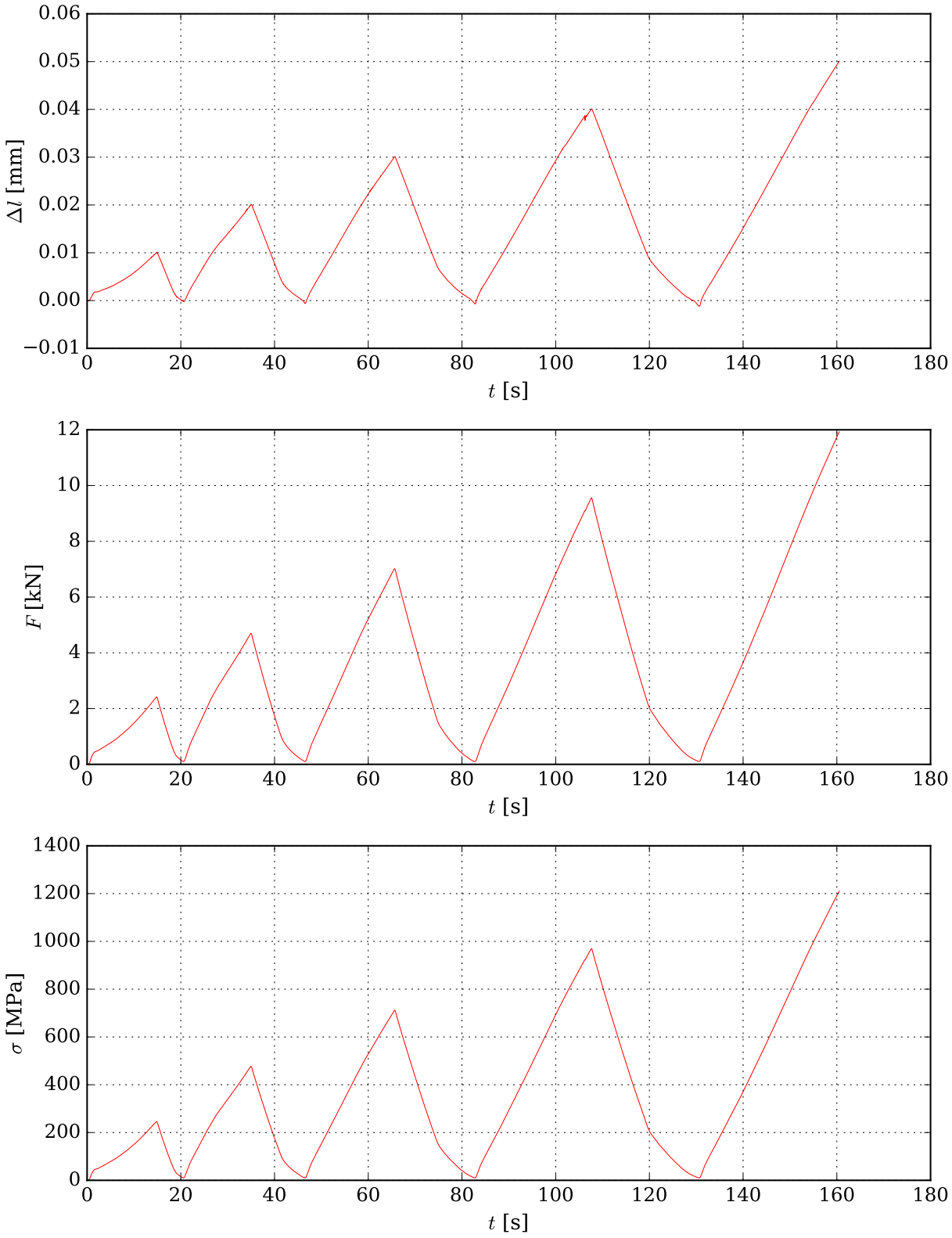

Figure A.5: Data for specimen G_C_LT2_5 obtained from cyclic tensile test and processed by *ploTRA*.

Table A.3: Geometrical and material parameters of specimens subjected to simple tensile tests with tabs made of aluminium.

specimen	width [mm]	$F_{\max}$ [N]	$\sigma_{\max}$ [MPa]
A_S_LT1_1	24.9	25897.6	1573.3
A_S_LT1_2	20.0	17008.1	1285.9
A_S_LT1_3	15.0	11394.9	1151.0
A_S_LT1_4	10.0	8891.5	1348.6
A_S_LT1_5	4.8	3174.1	997.8
A_S_LT2_1	24.9	18962.5	1153.9
A_S_LT2_2	20.1	20111.2	1516.0
A_S_LT2_3	15.0	15263.8	1545.9
A_S_LT2_4	10.8	11795.5	1656.3
A_S_LT2_5	5.0	4533.1	1370.9
A_S_LT3_1	25.0	19280.2	1166.6
A_S_LT3_2	20.0	19966.5	1515.6
A_S_LT3_3	15.0	14536.5	1464.4
A_S_LT3_4	10.0	9881.0	1497.1
A_S_LT3_5	5.0	4754.8	1440.9

Table A.4: Geometrical and material parameters of specimens subjected to simple tensile tests with tabs made of steel.

specimen	width [mm]	$F_{\max}$ [N]	$\sigma_{\max}$ [MPa]
S_S_LT1_1	25.1	23598.5	1425.1
S_S_LT1_2	20.0	16248.7	1229.1
S_S_LT1_3	15.0	11651.7	1174.6
S_S_LT1_4	10.0	7632.9	1154.2
S_S_LT1_5	5.0	4113.5	1239.1
S_S_LT2_1	25.1	19186.9	1156.8
S_S_LT2_2	20.1	19340.0	1459.3
S_S_LT2_3	15.1	14400.1	1449.7
S_S_LT2_4	10.1	10496.0	1576.1
S_S_LT2_5	5.1	3877.5	1161.1
S_S_LT3_1	25.1	23140.6	1396.9
S_S_LT3_2	19.9	15409.6	1172.1
S_S_LT3_3	15.0	9748.5	983.4
S_S_LT3_4	10.1	10190.1	1531.7
S_S_LT3_5	4.9	3959.1	1219.2

Table A.5: Geometrical and material parameters of specimens subjected to cyclic tensile tests with tabs made of glass fiber textile.

specimen	width [mm]	$F_{\max}$ [N]	$\sigma_{\max}$ [MPa]
G_C_LT1_1	25.0	19845.9	1205.2
G_C_LT1_2	25.1	23871.3	1439.3
G_C_LT1_3	19.9	21240.9	1615.6
G_C_LT1_4	19.9	18158.1	1380.4
G_C_LT1_5	15.0	16042.4	1621.5
G_C_LT1_6	15.0	14573.8	1472.1
G_C_LT1_7	10.0	10118.8	1531.6
G_C_LT1_8	10.0	9777.4	1481.4
G_C_LT1_9	5.0	5169.3	1572.7
G_C_LT1_10	5.0	5180.0	1579.2
G_C_LT2_1	25.0	25697.4	1560.5
G_C_LT2_2	25.0	18595.3	1127.4
G_C_LT2_3	20.1	19989.2	1508.3
G_C_LT2_4	20.4	14967.3	1112.7
G_C_LT2_5	14.9	11928.5	1210.5
G_C_LT2_6	15.0	14553.2	1474.0
G_C_LT2_7	10.0	9743.8	1482.3
G_C_LT2_8	10.0	9387.0	1425.1
G_C_LT2_9	5.0	4891.7	1494.3
G_C_LT2_10	5.0	5271.9	1604.0
G_C_LT3_1	24.9	22723.4	1382.2
G_C_LT3_2	24.9	23168.8	1409.8
G_C_LT3_3	20.0	17569.1	1330.3
G_C_LT3_4	20.0	16789.5	1275.1
G_C_LT3_5	15.0	15187.7	1536.2
G_C_LT3_6	15.0	14893.9	1505.4
G_C_LT3_7	10.0	9971.7	1510.9
G_C_LT3_8	10.1	10456.1	1576.4
G_C_LT3_9	5.0	5313.2	1610.1
G_C_LT3_10	4.9	4118.6	1286.7

Table A.6: Geometrical and material parameters of specimens subjected to cyclic tensile tests with tabs made of aluminium.

specimen	width [mm]	$F_{\max}$ [N]	$\sigma_{\max}$ [MPa]
A_C_LT1_1	25.0	22820.9	1382.0
A_C_LT1_2	25.1	26753.8	1616.3
A_C_LT1_3	20.1	13333.9	1004.6
A_C_LT1_4	20.1	18455.2	1393.9
A_C_LT1_5	15.0	10174.1	1028.4
A_C_LT1_6	15.0	10920.2	1100.9
A_C_LT1_7	10.0	8293.7	1259.1
A_C_LT1_8	10.0	8704.2	1316.2
A_C_LT1_9	4.9	2786.0	865.0
A_C_LT1_10	4.8	1553.7	494.6
A_C_LT2_1	25.0	20690.6	1253.5
A_C_LT2_2	25.0	23539.1	1425.5
A_C_LT2_3	20.0	16973.5	1283.9
A_C_LT2_4	20.0	18687.8	1413.6
A_C_LT2_5	15.0	15619.1	1581.9
A_C_LT2_6	15.0	16497.5	1666.4
A_C_LT2_7	10.0	8752.2	1326.1
A_C_LT2_8	10.0	10191.3	1541.1
A_C_LT2_9	5.0	5428.3	1631.9
A_C_LT2_10	5.0	4865.6	1468.5
A_C_LT3_1	25.0	19078.4	1156.7
A_C_LT3_2	25.0	18730.3	1134.7
A_C_LT3_3	20.1	15208.4	1149.3
A_C_LT3_4	20.0	17342.2	1311.8
A_C_LT3_5	15.0	11083.6	1119.6
A_C_LT3_6	15.0	10690.7	1077.7
A_C_LT3_7	10.0	7453.1	1129.3
A_C_LT3_8	10.0	8449.5	1276.4
A_C_LT3_9	5.0	5004.5	1504.5
A_C_LT3_10	5.0	4536.3	1369.2

Table A.7: Geometrical and material parameters of specimens subjected to cyclic tensile tests with tabs made of steel.

specimen	width [mm]	$F_{\max}$ [N]	$\sigma_{\max}$ [MPa]
S_C_LT1_1	25.1	20137.6	1216.1
S_C_LT1_2	25.0	22698.3	1374.0
S_C_LT1_3	20.1	17754.4	1340.3
S_C_LT1_4	20.1	16827.7	1266.0
S_C_LT1_5	15.0	11811.2	1193.1
S_C_LT1_6	15.0	12250.7	1234.1
S_C_LT1_7	10.0	8815.8	1330.4
S_C_LT1_8	10.1	7183.7	1083.0
S_C_LT1_9	5.0	3966.9	1199.7
S_C_LT1_10	5.0	4539.8	1375.7
S_C_LT2_1	25.1	24749.8	1491.6
S_C_LT2_2	25.2	19599.5	1179.8
S_C_LT2_3	20.1	18445.1	1391.8
S_C_LT2_4	20.2	17387.7	1307.4
S_C_LT2_5	15.1	15489.3	1557.3
S_C_LT2_6	15.1	13485.0	1355.8
S_C_LT2_7	10.1	9262.1	1390.8
S_C_LT2_8	10.1	9811.2	1479.2
S_C_LT2_9	5.1	4586.5	1370.6
S_C_LT2_10	5.1	4603.9	1373.1
S_C_LT3_1	25.1	19348.5	1169.8
S_C_LT3_2	25.5	20171.7	1197.6
S_C_LT3_3	19.9	17810.4	1359.5
S_C_LT3_4	19.9	17921.1	1363.1
S_C_LT3_5	15.1	12734.6	1281.2
S_C_LT3_6	15.0	13024.1	1314.7
S_C_LT3_7	10.1	9864.2	1481.2
S_C_LT3_8	10.1	9156.6	1380.5
S_C_LT3_9	5.0	3830.4	1153.8
S_C_LT3_10	5.0	4301.8	1298.4

A.2 Configuration Analysis

A.2.1 The Failure Mode Aspect

All the tested specimens were captured right after end of the test in the test machine by a digital camera and failure modes were subsequently determined from the obtained images. Specimens, which reached their strength failed by longitudinal splitting failure mode – **L** (Fig. A.6a) or explosive failure mode – **X** (Fig. A.6b), or the combination of the explosive and longitudinal splitting modes – **M** (Fig. A.6c) ocurred (Fig. 2.2). The initial failure area was impossible to determine with the available technologies, due to the fast sequence of failures. Record of the test by a camera with high frequency image capture would be necessary to determine the initial failure. While the cracking of specimens was brittle and the initial failure caused further failures, the failure was mostly multiple – **M**. In case of pure longitudinal splitting mode, the specimens failed mainly in the gage area – **G**.

From the failure mode aspect, the specimens configurations were equal. Failures between tabs did not occur and no tabs were detached, therefore the chosen adhesive may be considered as suitable for the used materials and test type.

A.2.2 The Specimen Manufacturing Aspect

The 5 mm wide specimens are excessively sensitive to vibrations when cutted by water jet. The tables were vibrating during the cutting process and these specimens have visibly uneven edges.

During the manufacturing process, manipulation with the plates (Fig. A.2a) was uncomfortable for the manufacturer due to the weight of the steel used for the tabs. Fracture of one plate with steel tabs ocurred during application of the steel tabs. Steel tabs of thickness 1.6 mm are too heavy for the brittle and 0.6 mm thin unidirectional composite material.

A.2.3 The Testing Procedure Aspect

During the loading process, tabs made of material under test (carbon/epoxy unidirectional long-fiber composite with fibers oriented in the loading direction) were sliding between the grips, therefore the loading force did not exceed 1700 N. The tabs made of material under test are in this case undesirable for used grips.

During the loading process of specimens with aluminium tabs, displacement and force values unpredictably dropped (Fig. A.7). This may be caused by slipping between the grips and grip holder when the 1.5 mm thick aluminium tab might have deformed under the clamping pressure.

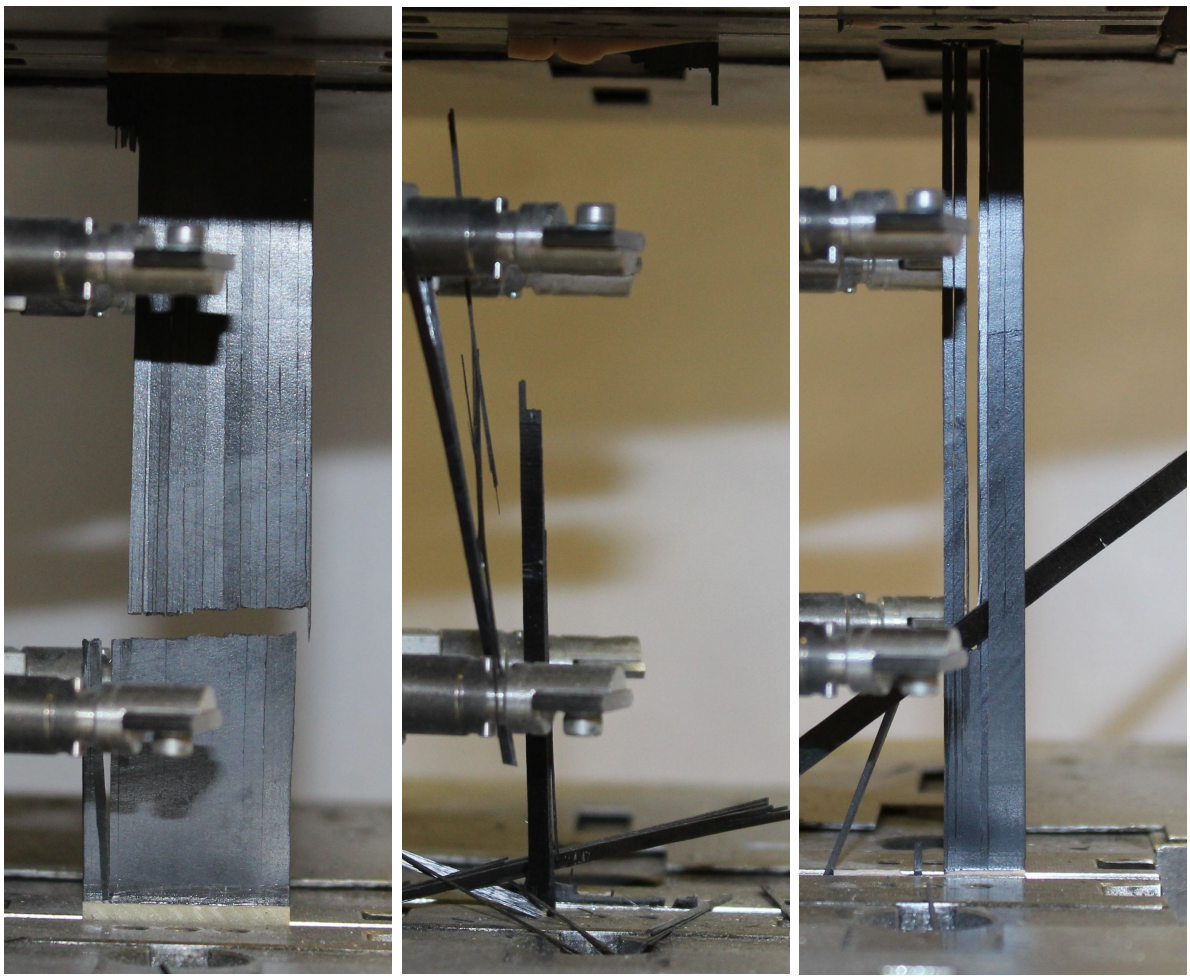

(a) Longitudinal failure mode. **(b)** Explosive failure mode. **(c)** Mixed failure mode.

Figure A.6: Three types of typical failures for the tested specimens.

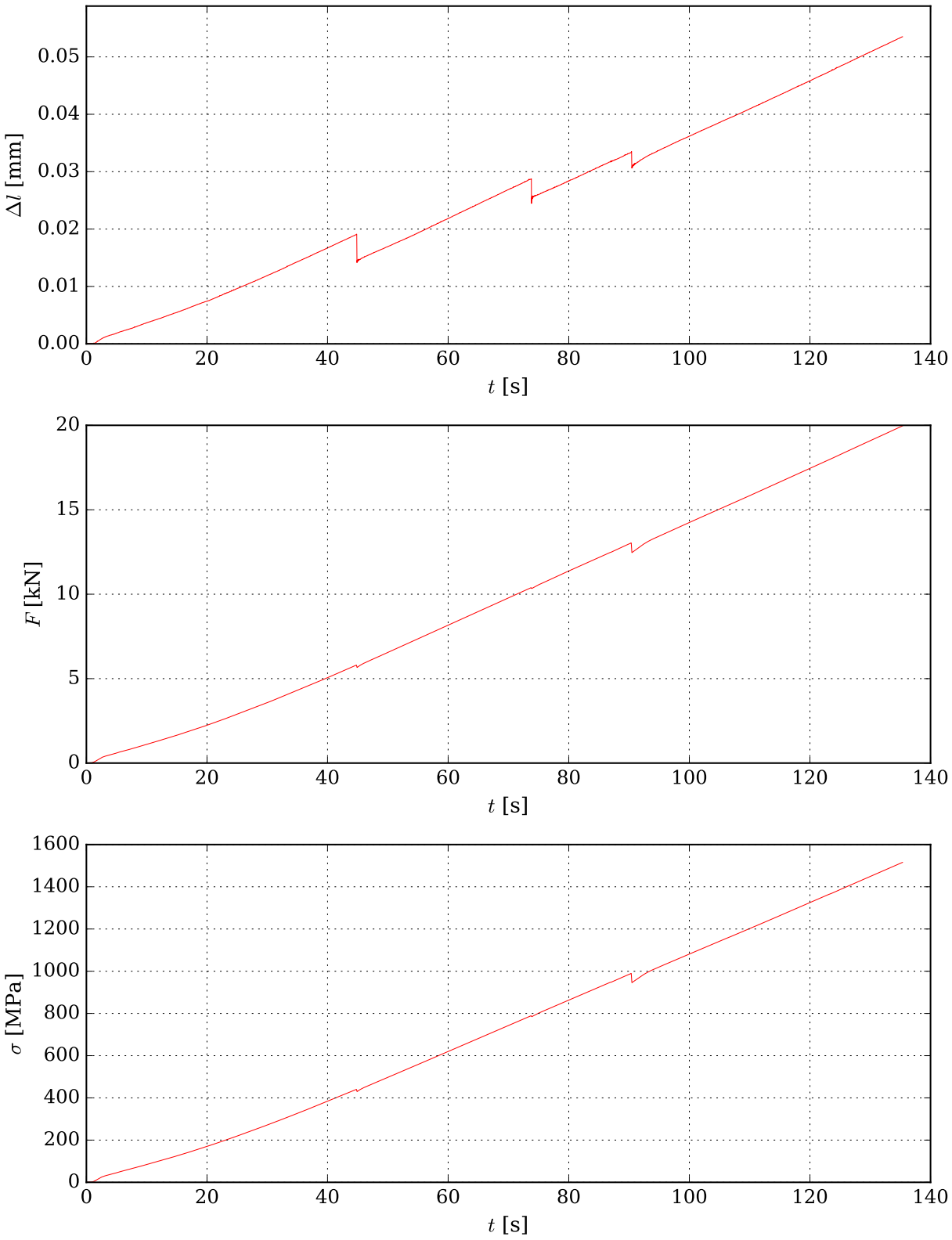

Figure A.7: Displacement-time, force-time and stress-time dependencies for specimens with aluminium tabs and simple tensile tests (A_S_LT3_2).

A.2.4 The Strength Aspect

The strengths of specimens subjected to simple tensile tests (Tabs. A.2, A.3 and A.4) and cyclic tensile tests (Tabs. A.5, A.6 and A.7) were averaged in groups with the same tab material (Tab. A.8), tab lengths (Tab. A.9) and specimen widths (Tab. A.10). Strength arithmetic means $\overline{\sigma}_{\max}$ and strength medians $\tilde{\sigma}_{\max}$ were determined for each group of specimens for simple tensile tests and cyclic tensile tests.

The average values of strengths of the specimen groups in this analysis are neither sensitive to the type of test (simple tensile test vs. cyclic tensile test) nor to the definition of average value (arithmetic mean $\overline{\sigma}_{\max}$ vs. median $\tilde{\sigma}_{\max}$). The highest strengths were reached for 10 mm wide specimen with glass fiber laminate tabs of length 56 mm.

Table A.8: Strengths of specimen groups with same tab materials.

tab material	simple tensile tests		cyclic tensile tests	
	$\overline{\sigma}_{\max}$ [MPa]	$\tilde{\sigma}_{\max}$ [MPa]	$\overline{\sigma}_{\max}$ [MPa]	$\tilde{\sigma}_{\max}$ [MPa]
aluminium	1378.9	1440.9	1276.1	1297.9
steel	1288.6	1229.1	1317.0	1335.4
glass fiber laminate	1455.2	1469.9	1444.0	1481.9

Table A.9: Strengths of groups of specimens with same tab lengths.

tab length [mm]	simple tensile tests		cyclic tensile tests	
	$\overline{\sigma}_{\max}$ [MPa]	$\tilde{\sigma}_{\max}$ [MPa]	$\overline{\sigma}_{\max}$ [MPa]	$\tilde{\sigma}_{\max}$ [MPa]
36	1338.1	1348.6	1299.1	1335.4
56	1409.5	1459.3	1416.3	1425.3
76	1375.0	1440.9	1321.7	1313.3

Table A.10: Strengths of groups of specimens with same width.

specimen width [mm]	simple tensile tests		cyclic tensile tests	
	$\overline{\sigma}_{\max}$ [MPa]	$\tilde{\sigma}_{\max}$ [MPa]	$\overline{\sigma}_{\max}$ [MPa]	$\tilde{\sigma}_{\max}$ [MPa]
5	1333.8	1370.9	1347.3	1374.4
10	1493.2	1531.7	1388.9	1408.0
15	1385.2	1464.4	1351.7	1335.3
20	1341.7	1299.9	1322.6	1335.3
25	1317.3	1299.4	1317.9	1313.8

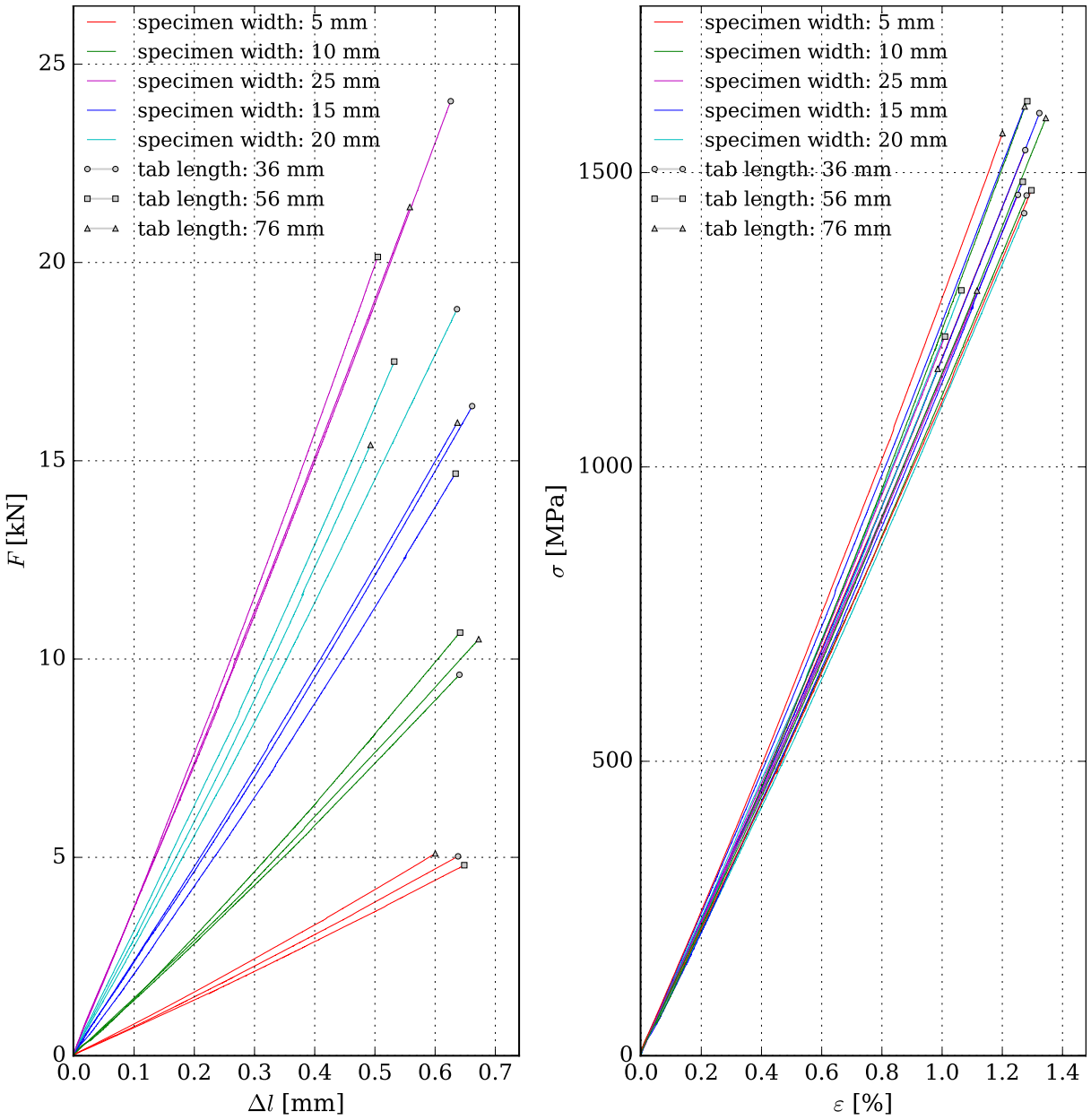

Figure A.8: Force/displacement and stress/strain dependencies for specimens with glass fiber textile tabs and simple tensile tests.

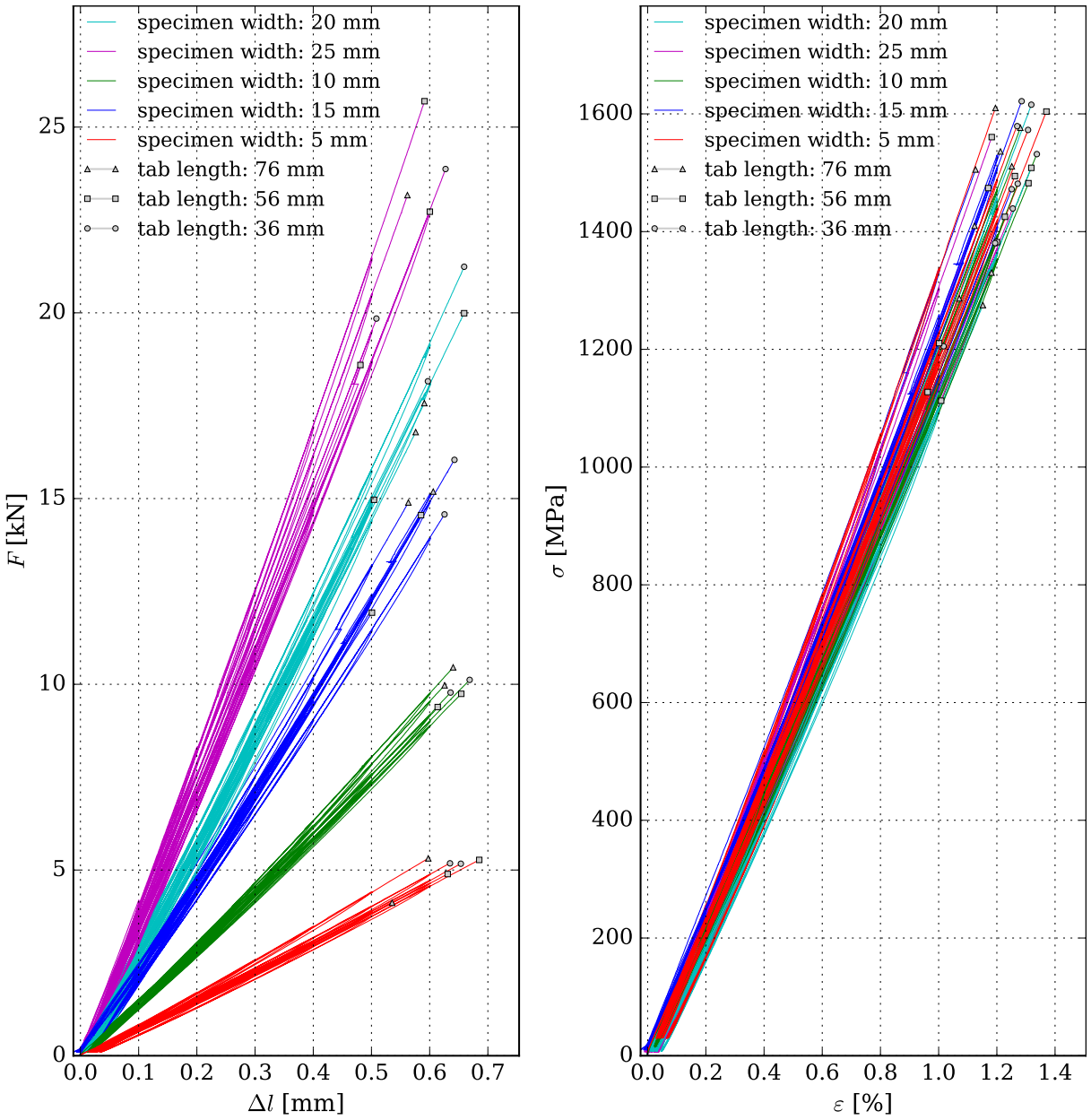

Figure A.9: Force/displacement and stress/strain dependencies for specimens with glass fiber textile tabs and cyclic tensile tests.

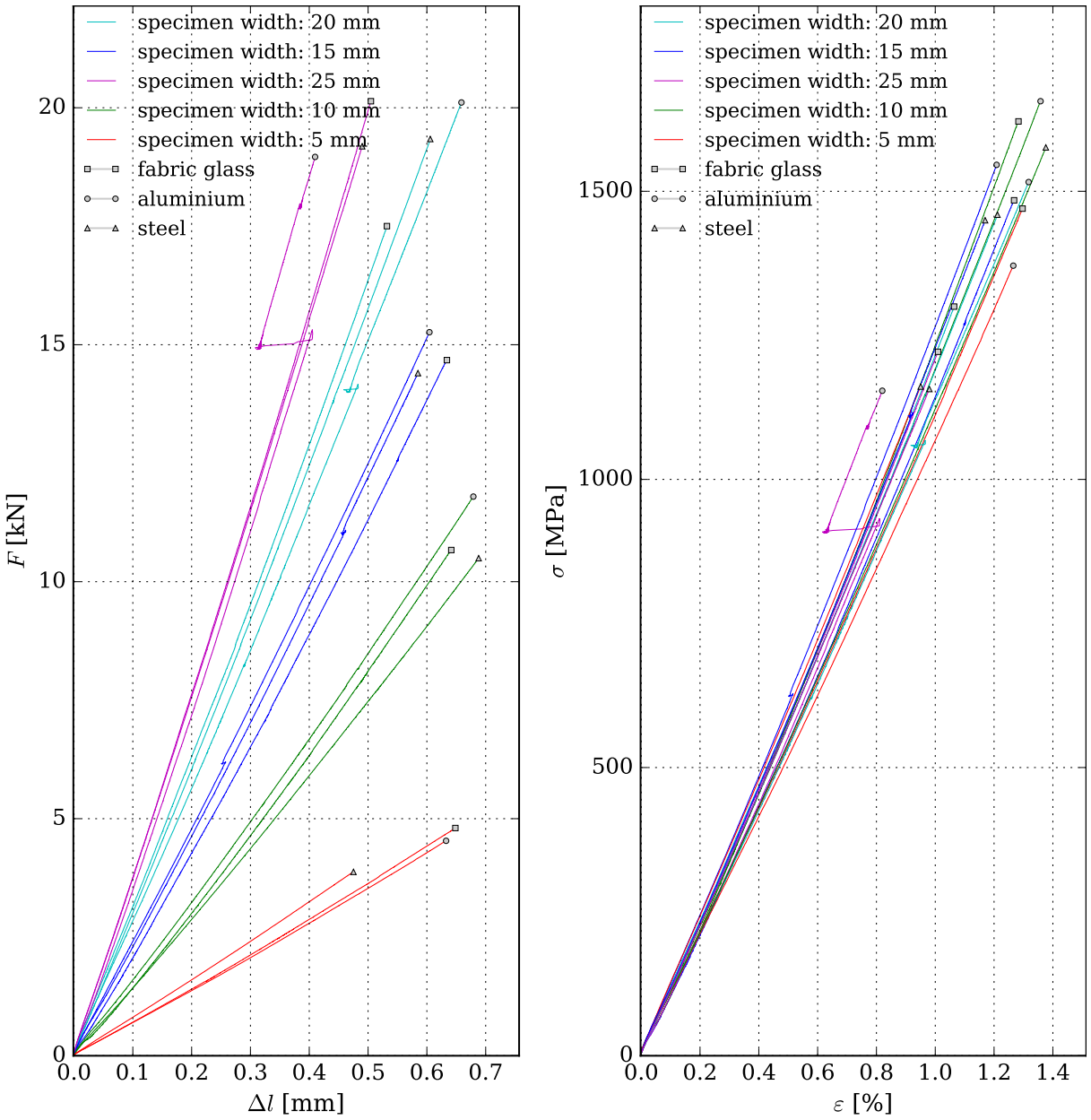

Figure A.10: Force/displacement and stress/strain dependencies for specimens with 56 mm long tabs and simple tensile tests.

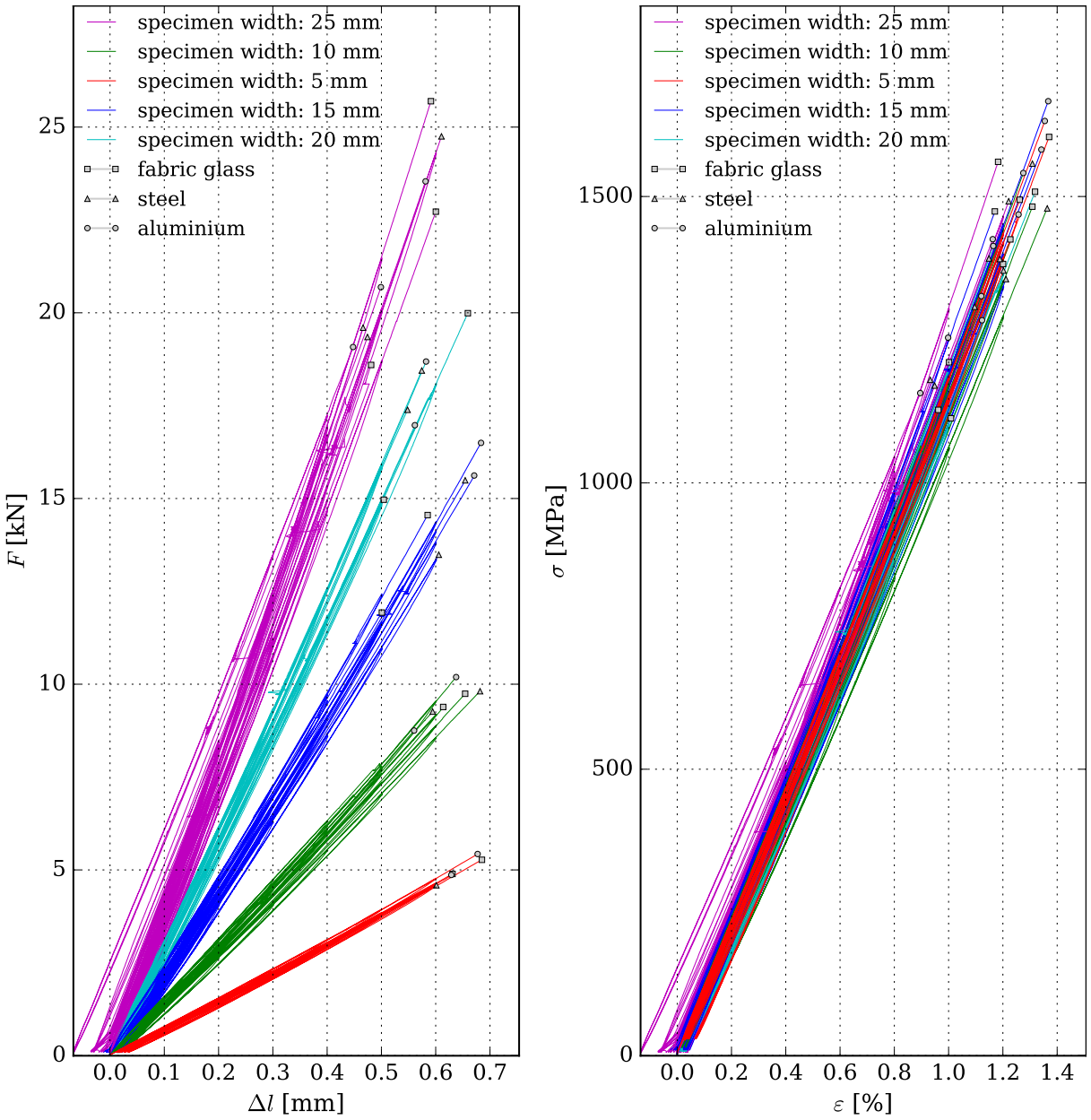

Figure A.11: Force/displacement and stress-train dependencies for specimens with 56 mm long tabs and cyclic tensile tests.

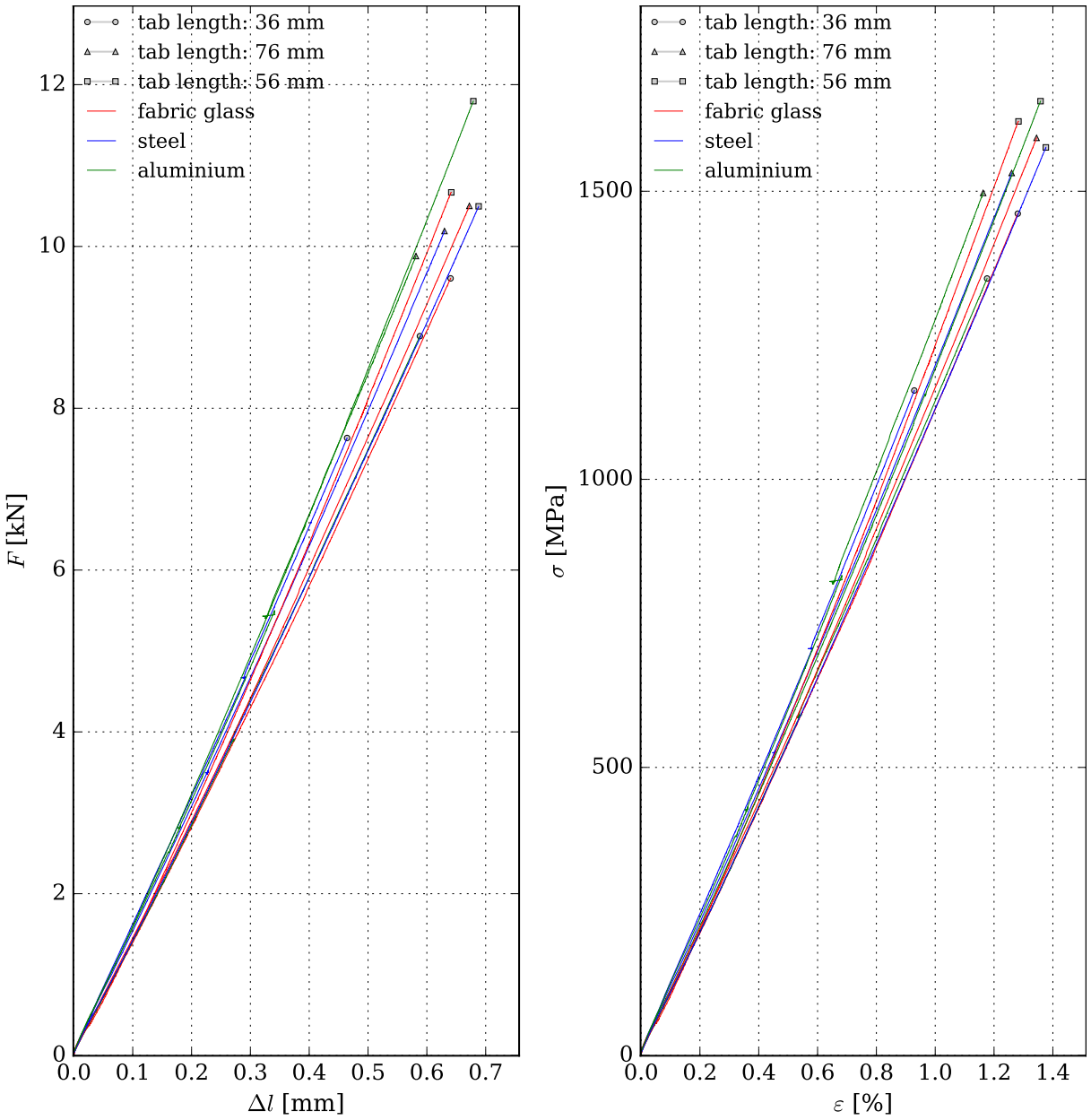

Figure A.12: Force/displacement and stress/strain dependencies for 10 mm wide specimens and simple tensile tests.

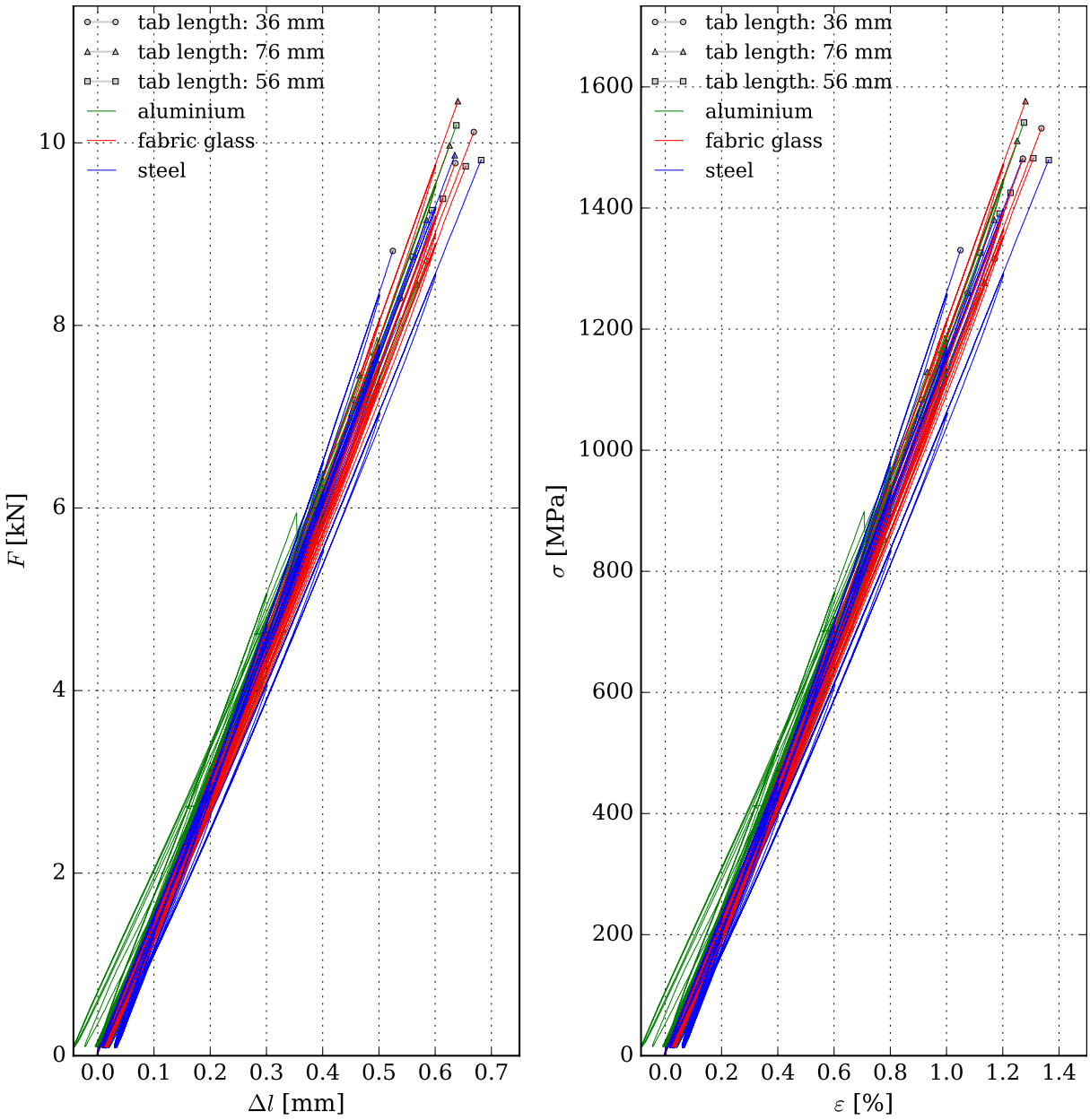

Figure A.13: Force/displacement and stress/strain dependencies for 10 mm wide specimens cyclic tensile tests.

Appendix B

SEM Images

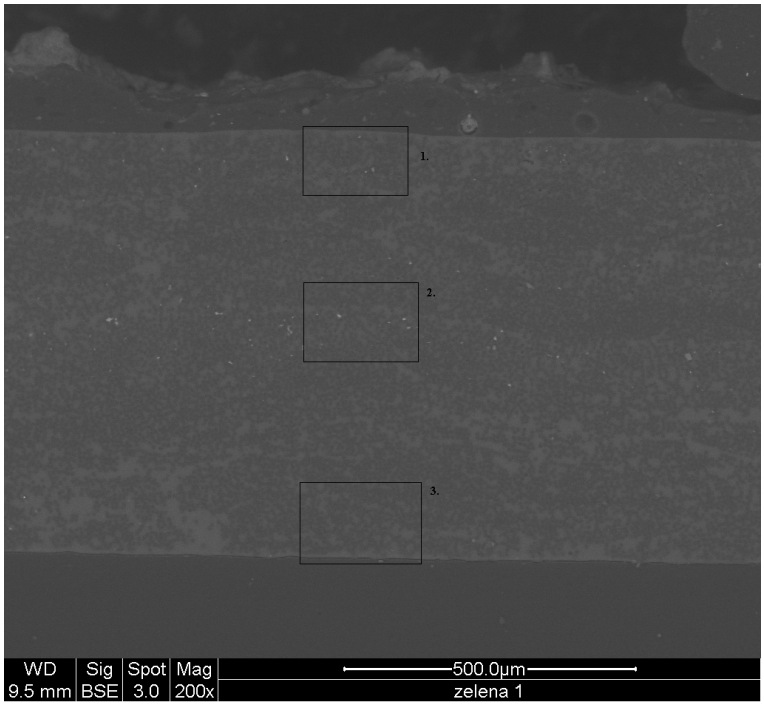

(a) Scheme of image positions in the cross-section of composite specimen number 1 with magnification 200.

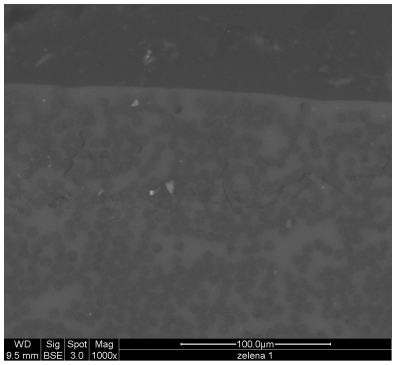

(b) Part 1, magnified 1000×

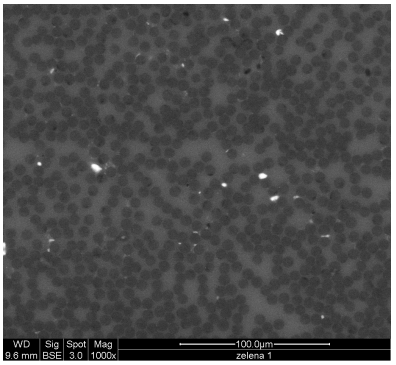

(c) Part 2, magnified 1000×

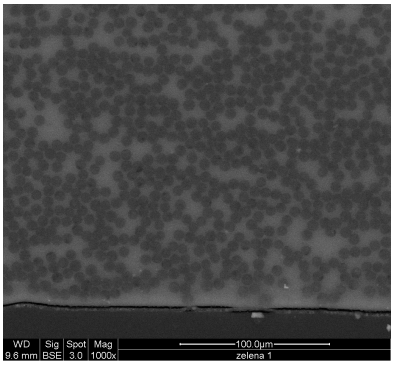

(d) Part 3, magnified 1000×

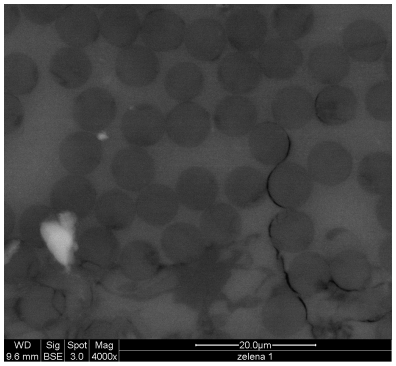

(e) Part 1, magnified 4000×

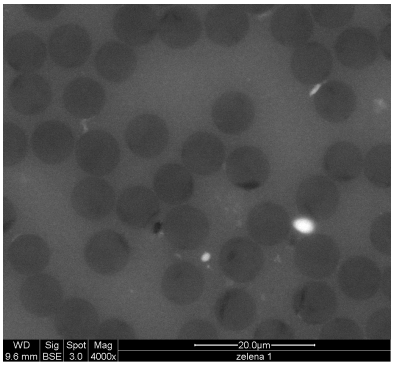

(f) Part 2, magnified 4000×

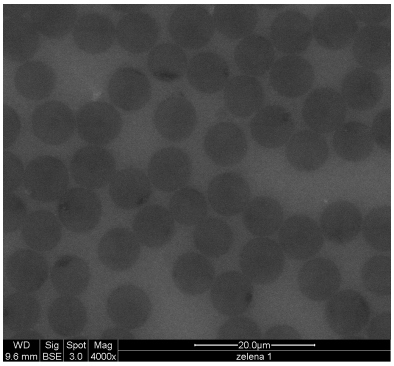

(g) Part 3, magnified 4000×

Figure B.1: Images of cross-section of specimen number 1.

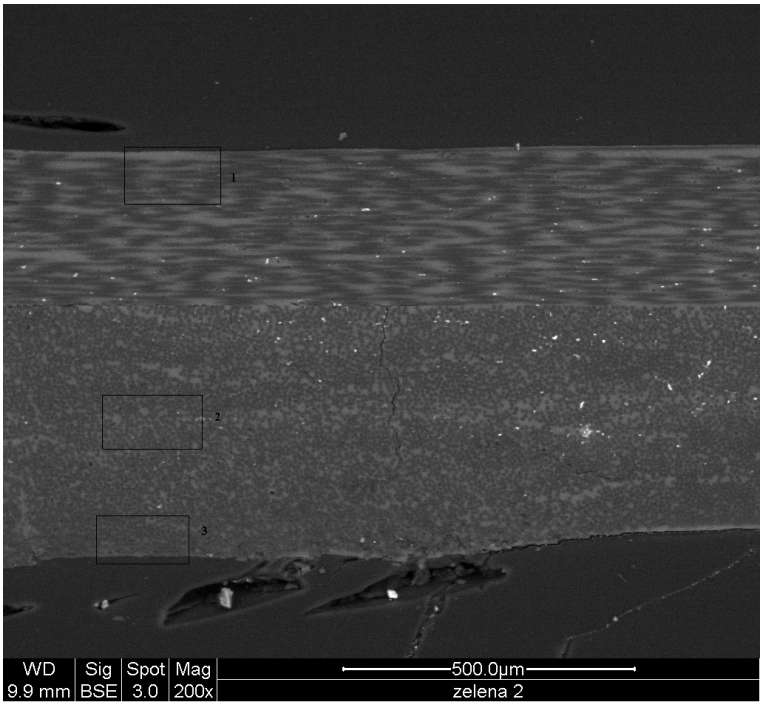

(a) Scheme of image positions in the cross-section of composite specimen number 2 with magnification 200.

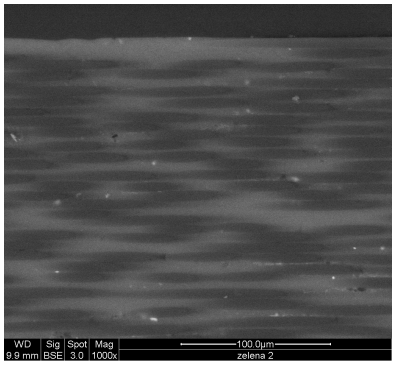

(b) Part 1, magnified 1000×

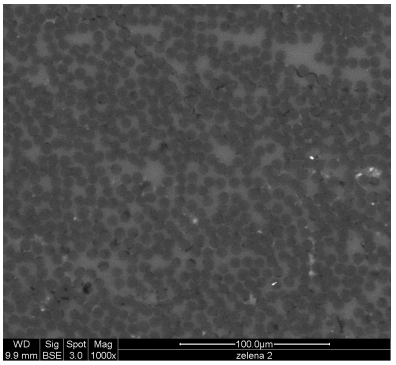

(c) Part 2, magnified 1000×

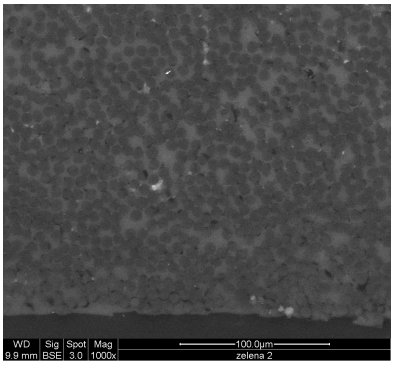

(d) Part 3, magnified 1000×

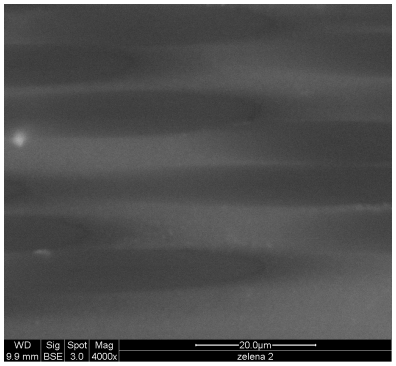

(e) Part 1, magnified 4000×

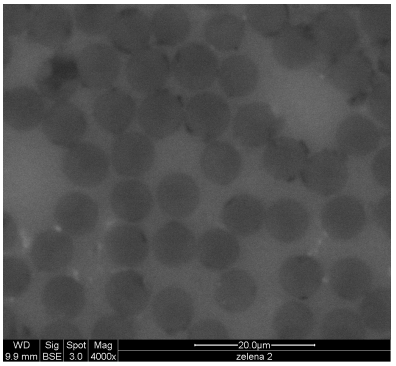

(f) Part 2, magnified 4000×

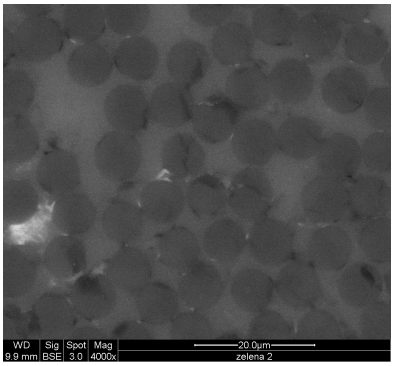

(g) Part 3, magnified 4000×

Figure B.2: Images of cross-section of specimen number 2.

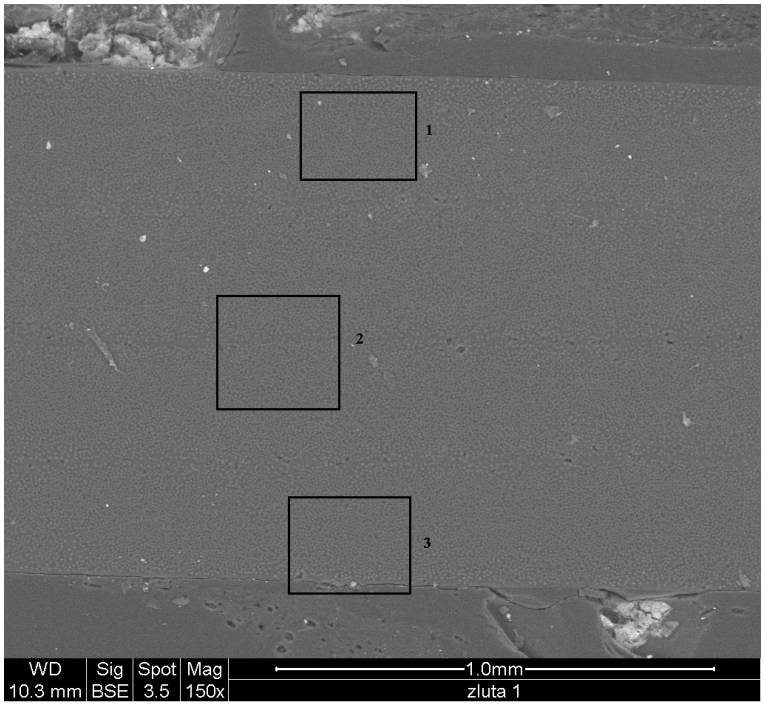

(a) Scheme of image positions in the cross-section of composite specimen number 3 with magnification 150.

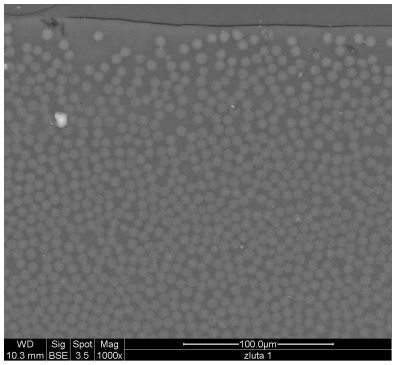

(b) Part 1, magnified 1000×

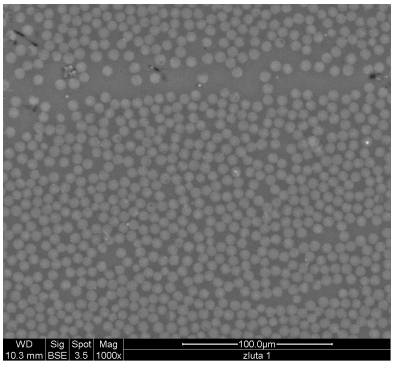

(c) Part 2, magnified 1000×

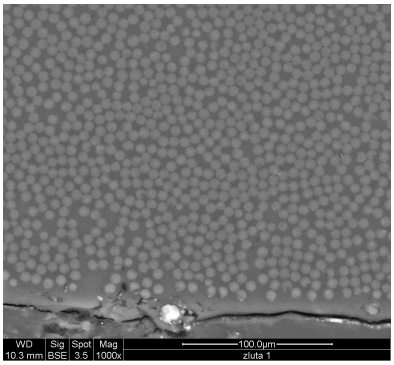

(d) Part 3, magnified 1000×

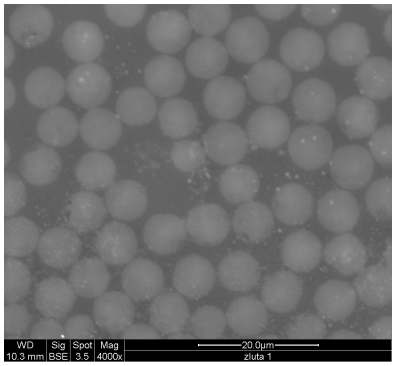

(e) Part 1, magnified 4000×

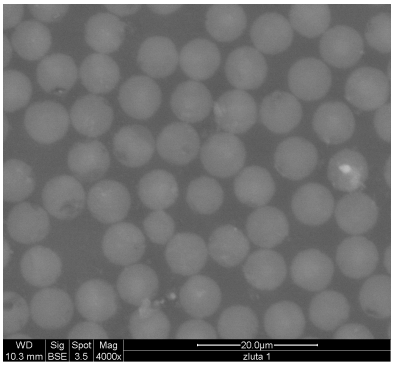

(f) Part 2, magnified 4000×

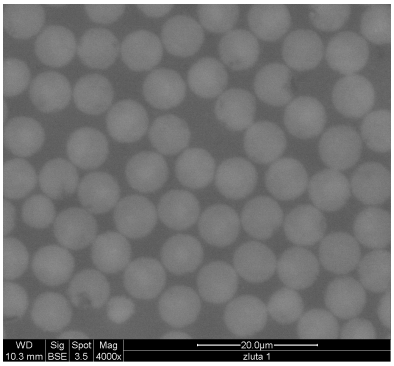

(g) Part 3, magnified 4000×

Figure B.3: Images of cross-section of specimen number 3.

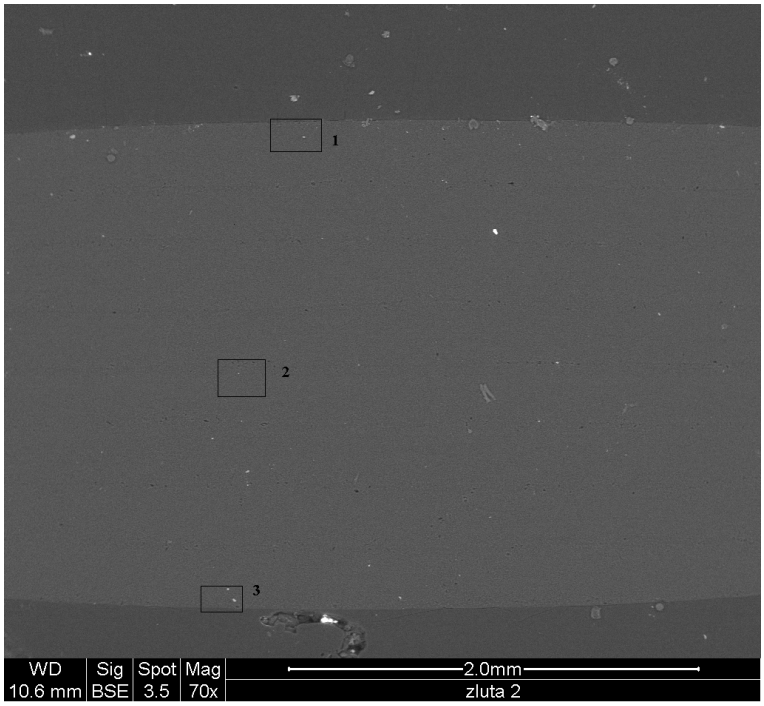

(a) Scheme of image positions in the cross-section of composite specimen number 4 with magnification 70.

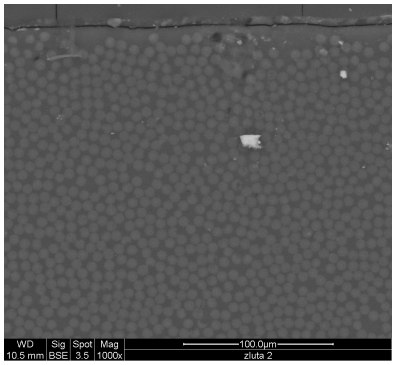

(b) Part 1, magnified 1000×

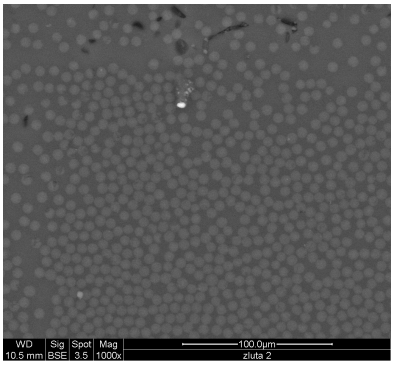

(c) Part 2, magnified 1000×

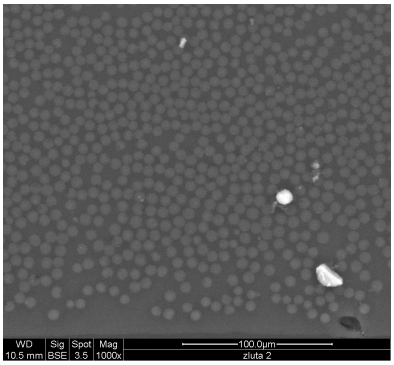

(d) Part 3, magnified 1000×

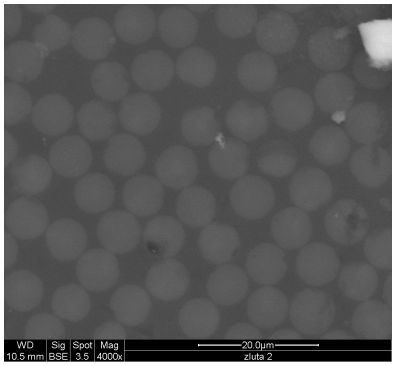

(e) Part 1, magnified 4000×

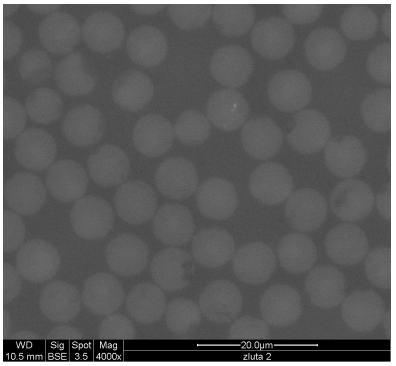

(f) Part 2, magnified 4000×

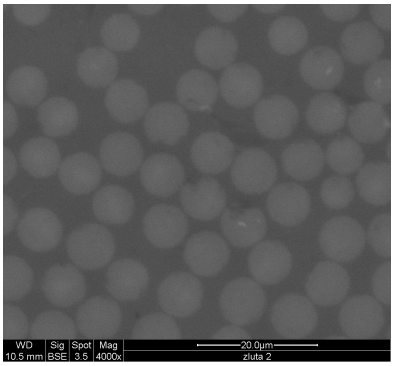

(g) Part 3, magnified 4000×

Figure B.4: Images of cross-section of specimen number 4.

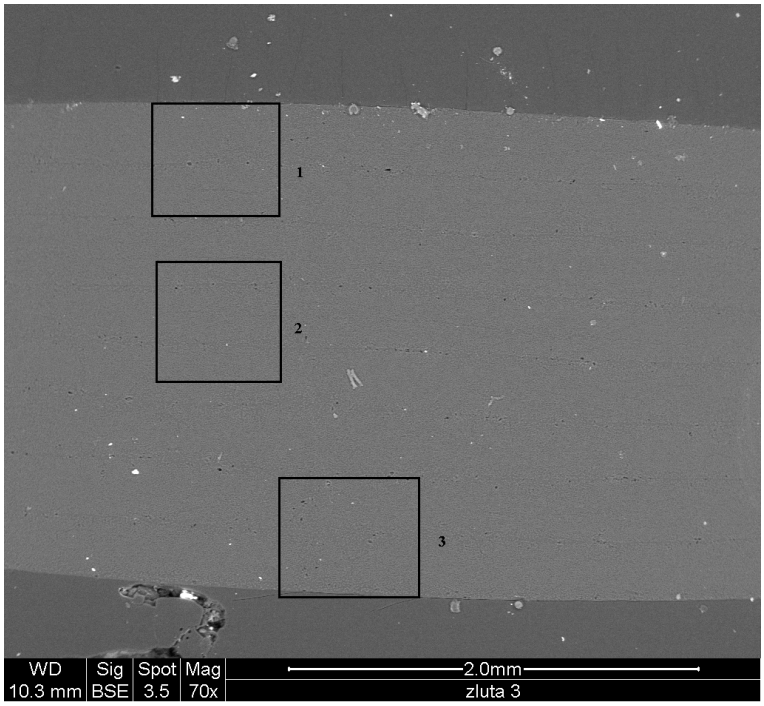

(a) Scheme of image positions in the cross-section of composite specimen number 5 with magnification 70.

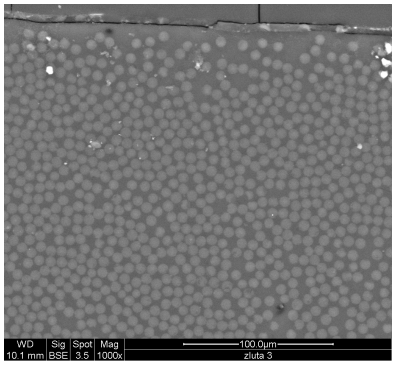

(b) Part 1, magnified 1000×

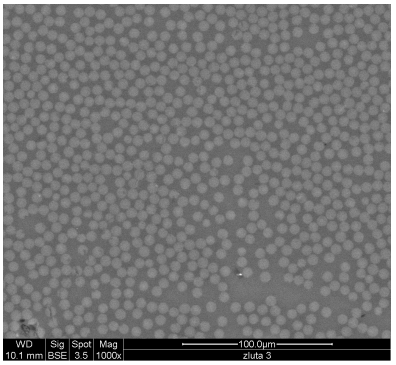

(c) Part 2, magnified 1000×

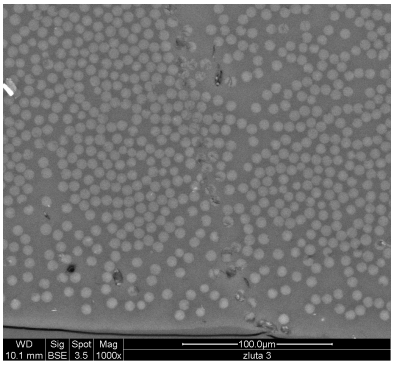

(d) Part 3, magnified 1000×

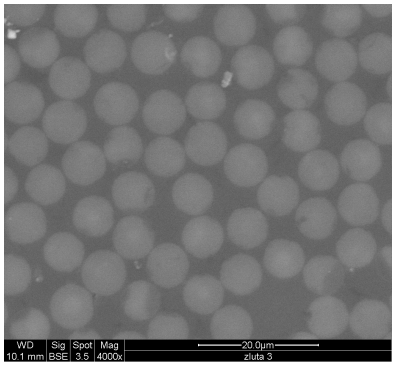

(e) Part 1, magnified 4000×

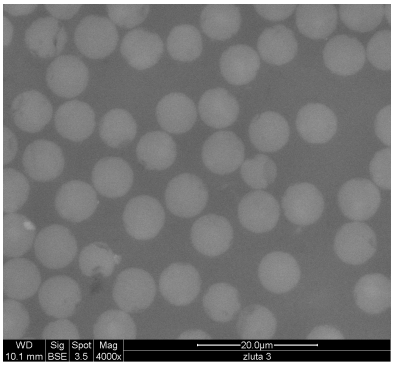

(f) Part 2, magnified 4000×

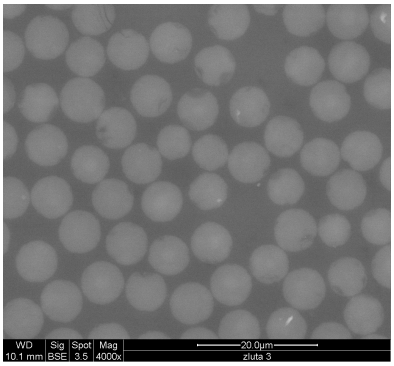

(g) Part 3, magnified 4000×

Figure B.5: Images of cross-section of specimen number 5.

Appendix C

Epoxy

To obtain experimental data for further improvement of material models of carbon/epoxy composite (section 5.5), uniaxial cyclic static tests are performed on low-molecular weight epoxy resin CHS-EPOXY 520 hardened with CHS-P 11. The specimen were prepared and tests performed according to ASTM standard D638-10. Experimental data were processed using *Python* and function library *ploTRA*. A one-dimensional elasto-plastic model with damage was proposed and the corresponding material properties identified using *optiSLang*.

C.1 Experiments

C.1.1 Specimen Manufacturing

Specimens were manufactured according to standard test method ASTM D638-10: Tensile Properties of Plastics [70]. The low molecular epoxy resin CHS-EPOXY 520 was mixed with hardener CHS-P 11 in the weight ratio given by manufacturer – 100:11. Air bubbles, which ocurred in the viscous mixture when blending the two components, were removed by placing the liquid mixture (resin) for 10 minutes into a vacuum desiccator. The presence of the air bubbles is highly undesirable, since they are stress concentrators in the material and they reduce the effective cross-section.

The resin free from bubbles was poured into a perspex three-part mould. The mould consisted of two plates and a spacer, which defined the resulting epoxy tab thickness. All three parts of mould were coated by 4 layers of a separator and bolted together.

Epoxy plate cured in the form at room temperature was detached from the form parts approximately 10 hours after mixing. Rectangular epoxy plates had dimensions approximately 245×135 mm, and its thickness of 3.94 mm was given by the chosen central (distance) part of mould. Bone-shaped specimens (Fig. C.1) were cut with water jet after another week of curing at room temperature. The process of specimen manufacturing, such as the chosen material, separator, curing duration, mould type, air bubbles vacuuing, etc. was discussed with Ing. Jan Klesa Ph.D. from the Department of Aerospace Engineering, CTU.

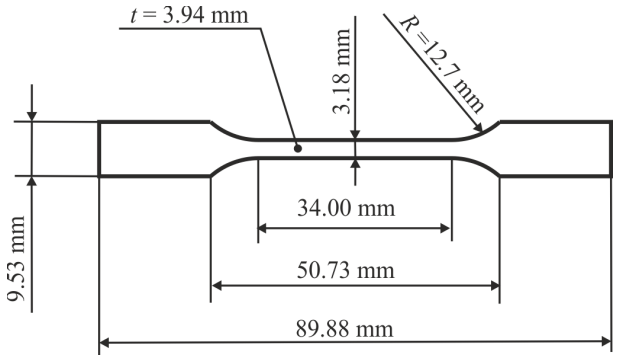

Figure C.1: Dimensions of epoxy specimens.

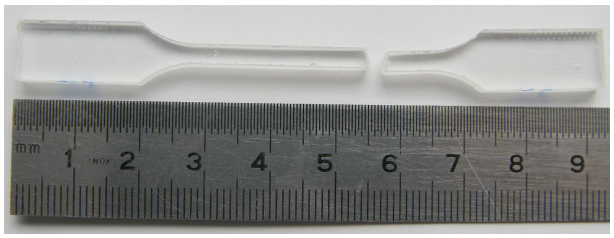

Figure C.2: Cracked specimen.

C.1.2 Cyclic Tensile Tests

Specimens were divided into 3 groups according to their curing time:

- 7 days – red color in graphs
- 152 days – green color in graphs
- 255 days – blue color in graphs

The experimental tests were performed on test machine ZWICK ROELL/Z050 with clip-on biaxial extensometer BTC-EXACLBI.001. The specimens were subjected to uniaxial tensile cyclic loading at room temperature. Unloading in each cycle started when gage area elongation exceeded a multiple of $\Delta l = 0.02$ mm. Loading in the corresponding cycle started when tensile force decreased under 30 % of force at the start of the unloading.

C.2 Effects of Curing Time

Specimens were subjected to the cyclic tensile loading until failure. The fracture was always brittle and no necking ocurred. Image of a cracked specimen with rupture is shown in Fig. C.2.

Experimental data obtained from the cyclic tensile tests are depicted in form of stress-strain dependencies in Fig. C.3. The data were further processed using *Python*. Maxima – $\mathrm{P}^{\max}$, and minima – $\mathrm{P}^{\min}$ of the loading cycles and the cross points – $\mathrm{P}^{\mathrm{int}}$ (Fig. C.4)

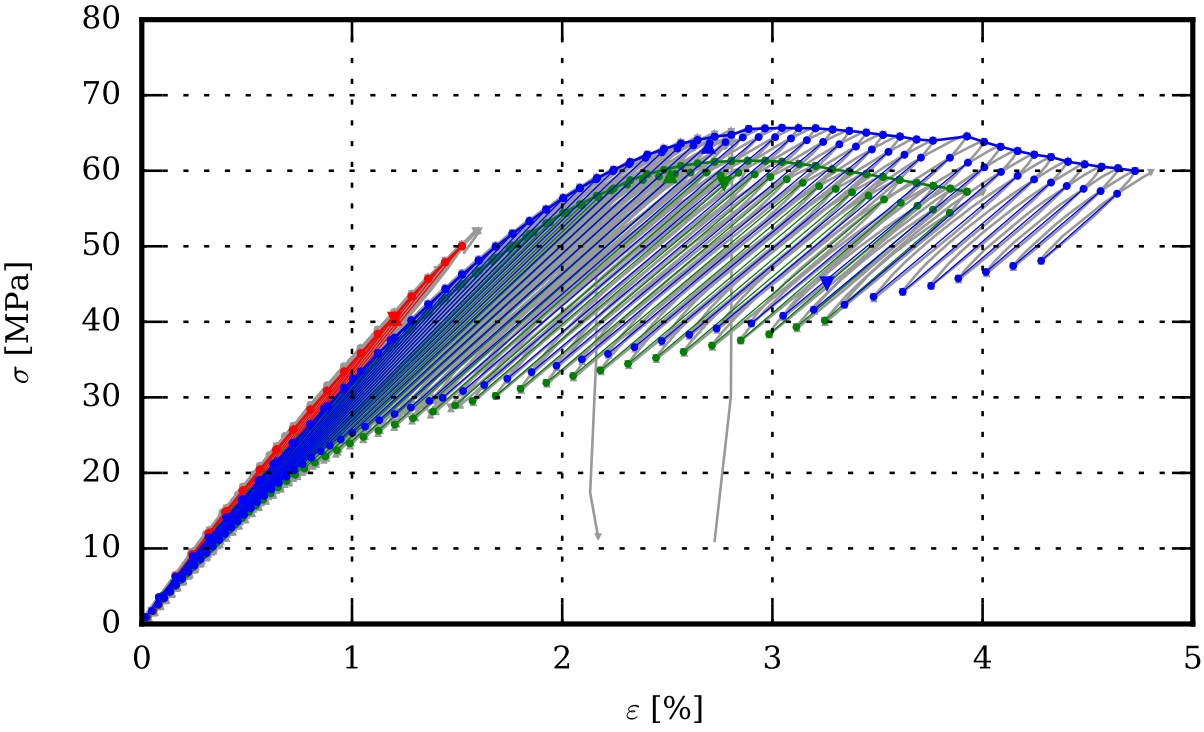

Figure C.3: Experimentally obtained stress-strain dependencies for 7 days (red), 152 days (green) and 255 days (blue) cured epoxy.

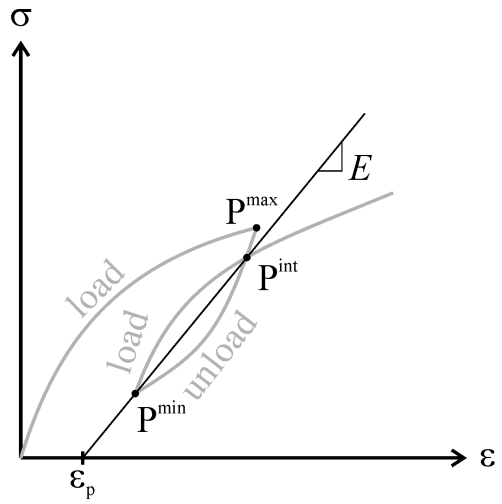

Figure C.4: One cycle of the stree-strain dependency and principle of Young's modulus identification.

were found. Tangents of the cycles, which can be considered as Young's moduli E, are identified as the slope of a line connecting given cycle intersection and minimum points ($\mathrm{P}^{\mathrm{int}}$ and $\mathrm{P}^{\mathrm{min}}$).

The epoxy showed damage behavior, since the value of Young's modulus E was a decreasing function of the reached maximal strain. Young's modulus is depicted as a function of strain ε (Fig. C.5 – left), corresponding to the maximum point $\mathrm{P}^{\mathrm{max}}$ of the particular cycle. In case of the specimens cured for 152 and 255 days, the values of the cycle tangents slightly increased just before failure.

The material also showed plastic behavior, dependency of strain-plastic strain is shown in Fig. C.5 – right. The plastic strain ε_{p} was evaluated for each cycle as intersection of the cycle tangent (line through points $\mathrm{P}^{\mathrm{int}}$ and $\mathrm{P}^{\mathrm{min}}$) and the strain axis ($\sigma = 0$). The strain values ε are the strains at the $\mathrm{P}^{\mathrm{max}}$ points, where unloading for each cycle begins.

Model for elasto-plastic and damage behavior of the epoxy resin to simulate one dimensional pure tensile, compressive or shear test was proposed in *Python*. The proposed material model with identified properties is described in authors work [7].

The experimentally obtained stress-strain dependencies show, that curing of the tested epoxy significantly changes the material behavior. The specimens from material with longer curing time had higher values of achieved maximum stresses $\sigma_{\max}$ and maximum strains $\varepsilon_{\max}$. Averaged data within the groups of tested specimens are summarized in Tab. C.1.

In case of curing of the tested epoxy at room temperature, we can assume, that the material undergoes significant molecular changes effecting the overall behavior of the resin. The longer cured material withstands more cycles, it becomes strengthened and ductility increases.

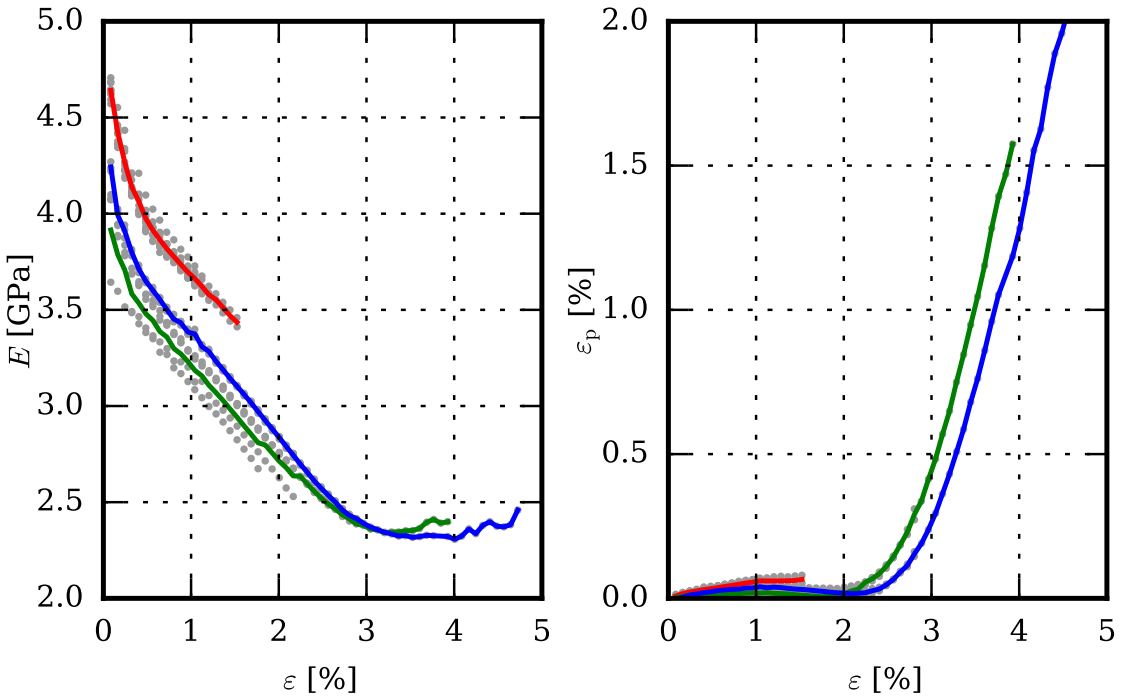

Figure C.5: Young's modulus-strain(left) and plastic strain-strain (right) dependencies of 7 days (red), 152 days (green) and 255 days (blue) cured epoxy.

Table C.1: Averaged data for specimens with different curing times.

curing time t [days]	number of specimens	max. stress $\overline{\sigma}_{\max}$ [MPa]	max. strain $\overline{\varepsilon}_{\max}$ [%]	achieved cycles
7	10	40.50	1.20	14
152	5	59.37	2.77	32
255	3	63.28	3.26	40

Appendix D

Influence of Irregularity

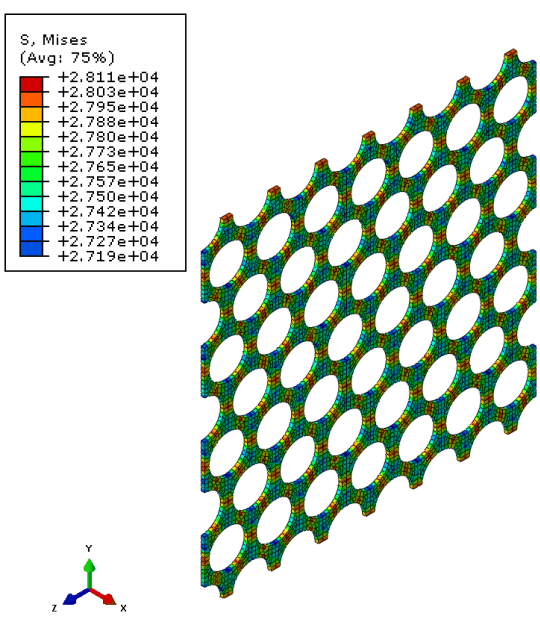

(a) $\boldsymbol{\sigma}_{123} = [1, 0, 0, 0, 0, 0]^{\mathrm{T}}$ MPa

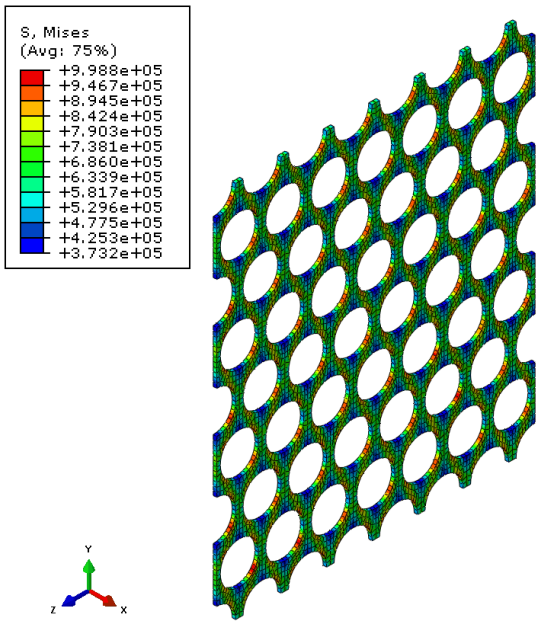

(b) $\boldsymbol{\sigma}_{123} = [0, 1, 0, 0, 0, 0]^{\mathrm{T}}$ MPa

Figure D.1: Equivalent von Mises stress on matrix elements of regular unit cell **a** loaded by uniaxial stress.

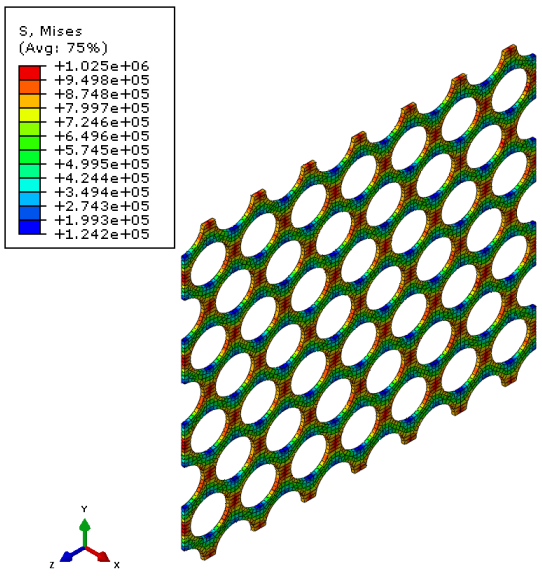

(a) $\boldsymbol{\sigma}_{123} = [0, 0, 1, 0, 0, 0]^{\mathrm{T}}$ MPa

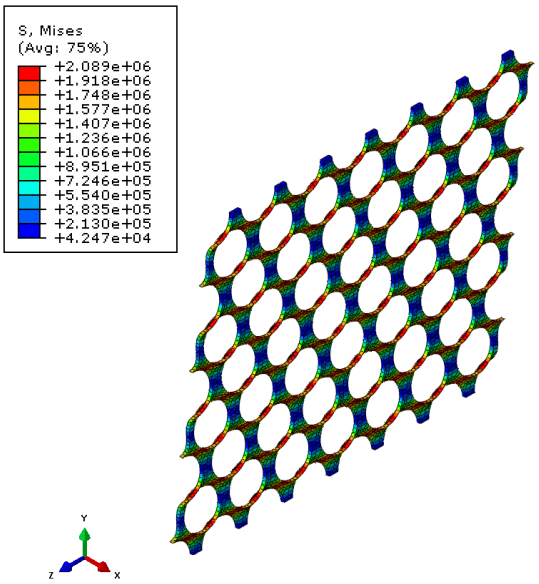

(b) $\boldsymbol{\sigma}_{123} = [0, 0, 0, 1, 0, 0]^{\mathrm{T}}$ MPa

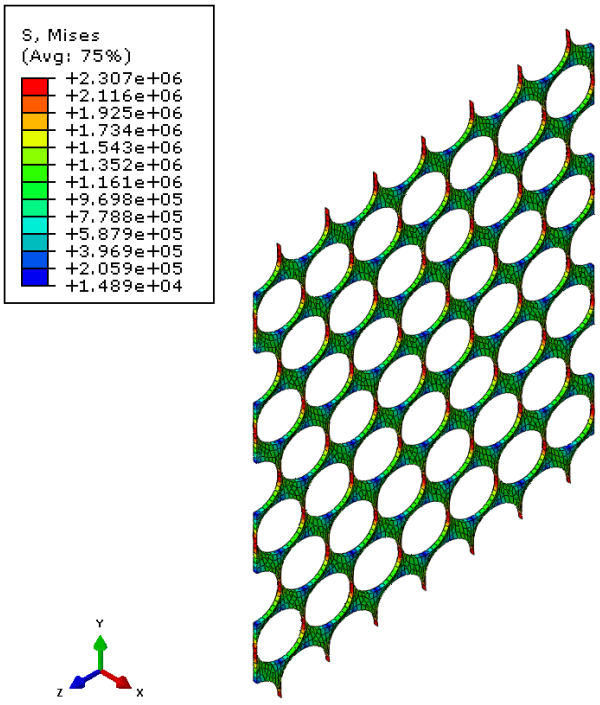

(c) $\boldsymbol{\sigma}_{123} = [0, 0, 0, 0, 1, 0]^{\mathrm{T}}$ MPa

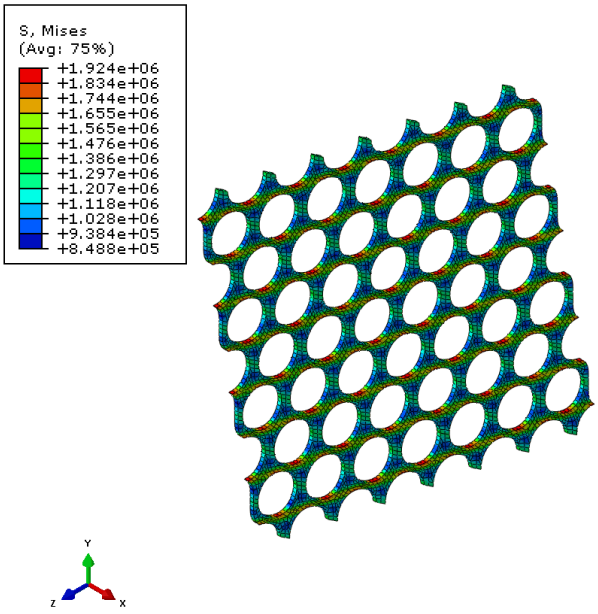

(d) $\boldsymbol{\sigma}_{123} = [0, 0, 0, 0, 0, 1]^{\mathrm{T}}$ MPa

Figure D.2: Equivalent von Mises stress on matrix elements of regular unit cell **a** loaded by uniaxial stress.

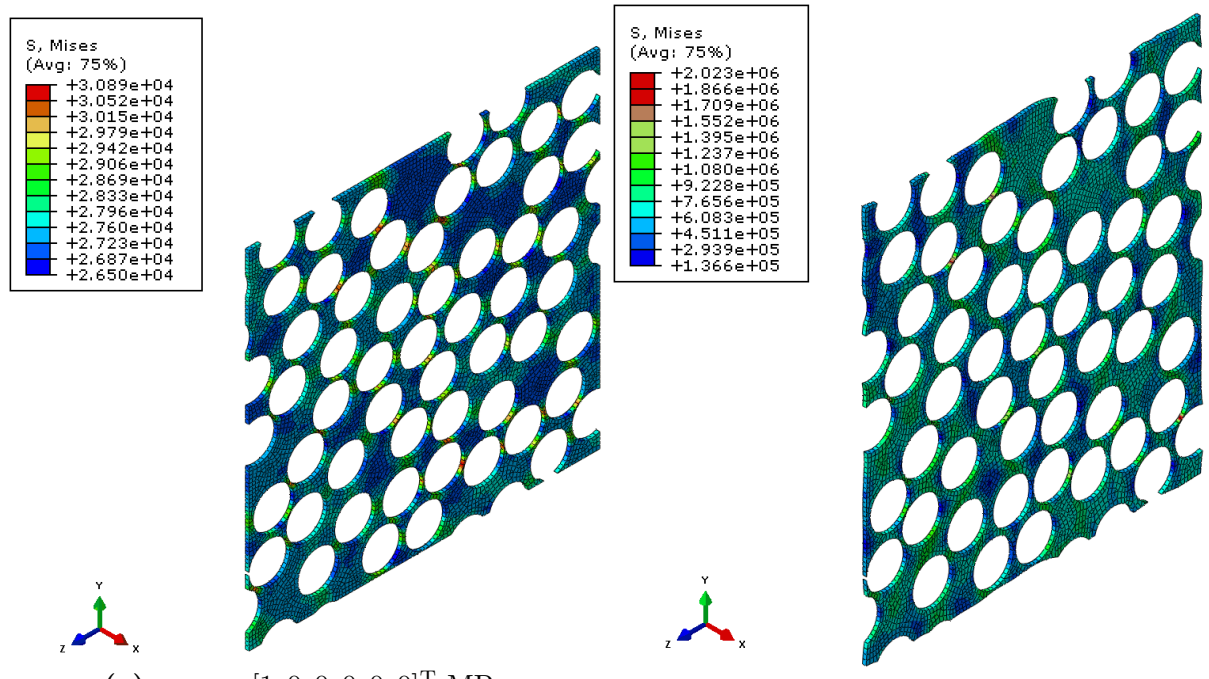

(a) $\boldsymbol{\sigma}_{123} = [1, 0, 0, 0, 0, 0]^{\mathrm{T}}$ MPa

(b) $\boldsymbol{\sigma}_{123} = [0, 1, 0, 0, 0, 0]^{\mathrm{T}}$ MPa

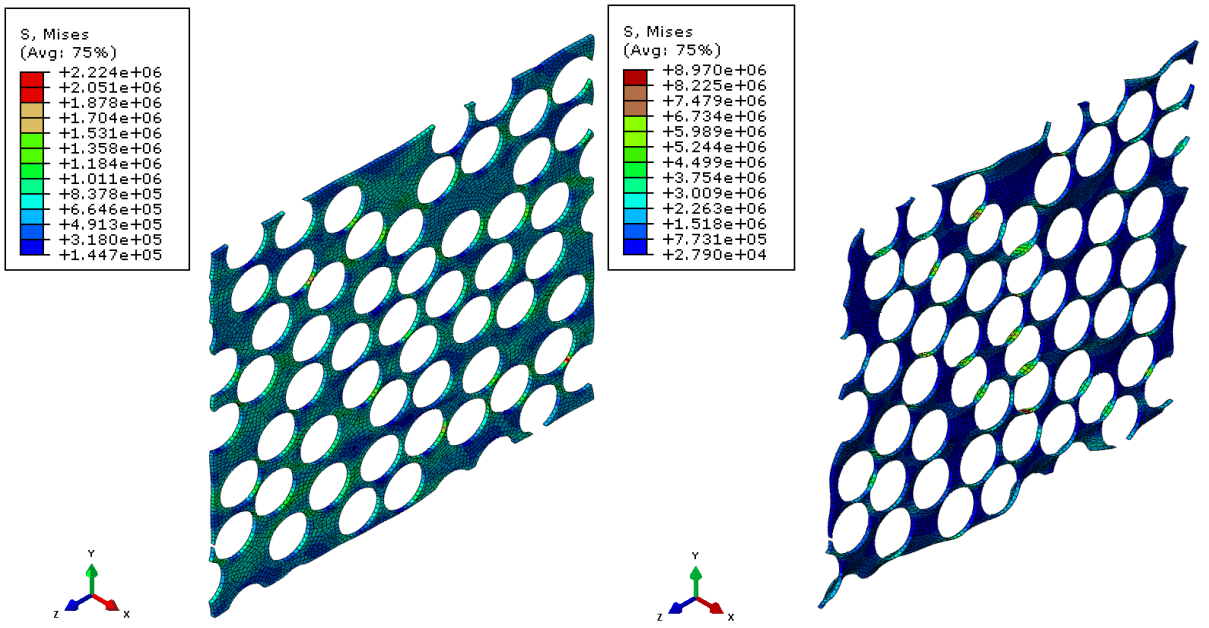

(c) $\boldsymbol{\sigma}_{123} = [0, 0, 1, 0, 0, 0]^{\mathrm{T}}$ MPa

(d) $\boldsymbol{\sigma}_{123} = [0, 0, 0, 1, 0, 0]^{\mathrm{T}}$ MPa

Figure D.3: Equivalent von Mises stress on matrix elements of random unit cell **b** loaded by uniaxial stress.

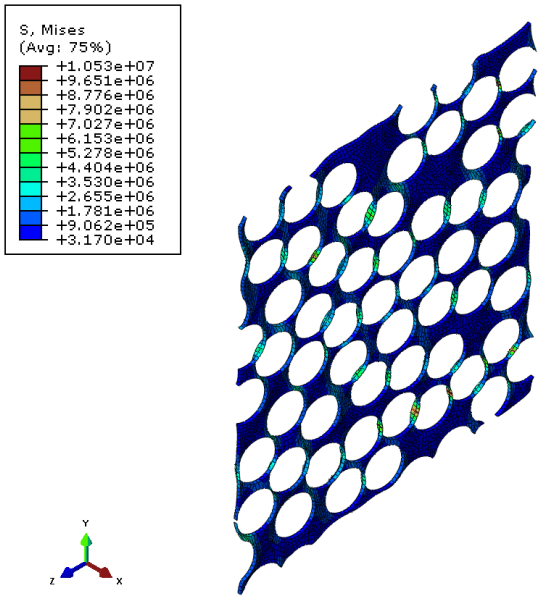

(a) $\boldsymbol{\sigma}_{123} = [0, 0, 0, 0, 1, 0]^{\mathrm{T}}$ MPa

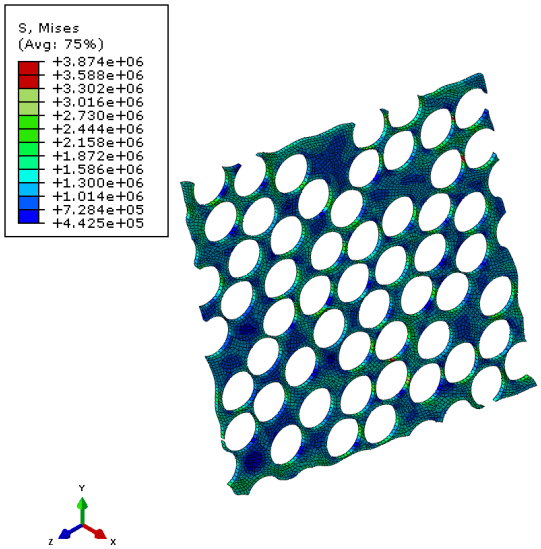

(b) $\boldsymbol{\sigma}_{123} = [0, 0, 0, 0, 0, 1]^{\mathrm{T}}$ MPa

Figure D.4: Equivalent von Mises stress on matrix elements of random unit cell **b** loaded by uniaxial stress.

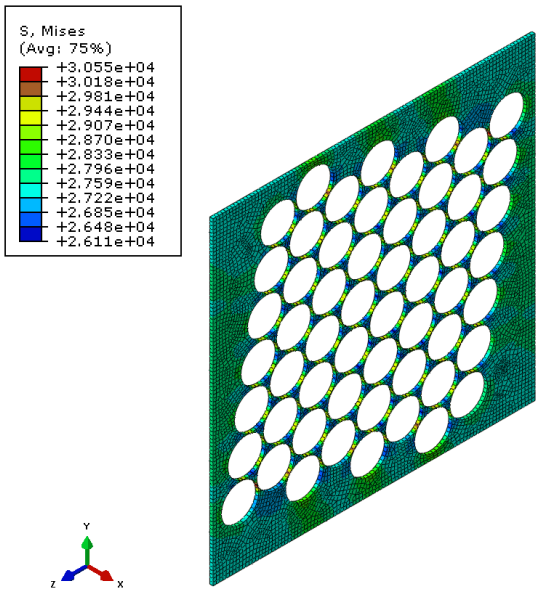

(a) $\boldsymbol{\sigma}_{123} = [1, 0, 0, 0, 0, 0]^{\mathrm{T}}$ MPa

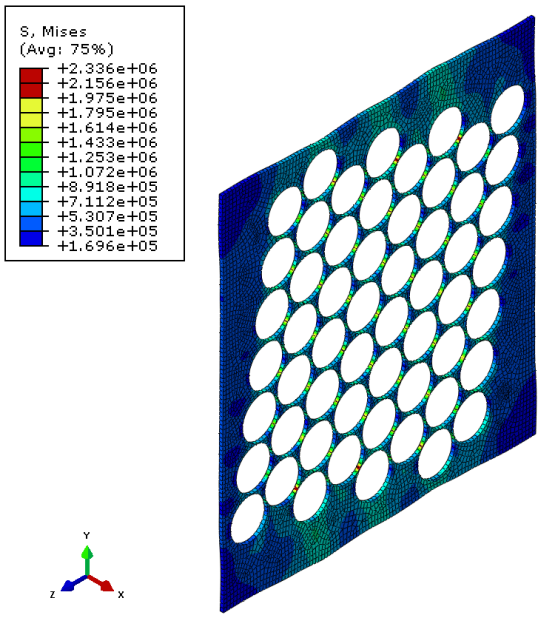

(b) $\boldsymbol{\sigma}_{123} = [0, 1, 0, 0, 0, 0]^{\mathrm{T}}$ MPa

Figure D.5: Equivalent von Mises stress on matrix elements of cluster unit cell **c** loaded by uniaxial stress.

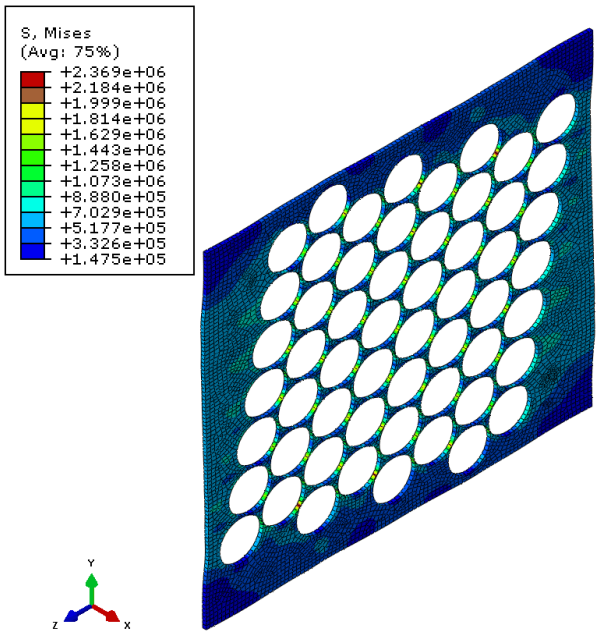

(a) $\boldsymbol{\sigma}_{123} = [0, 0, 1, 0, 0, 0]^{\mathrm{T}}$ MPa

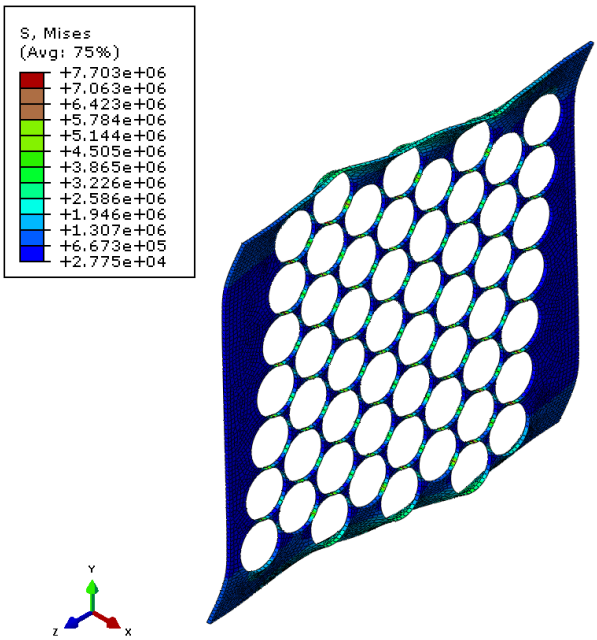

(b) $\boldsymbol{\sigma}_{123} = [0, 0, 0, 1, 0, 0]^{\mathrm{T}}$ MPa

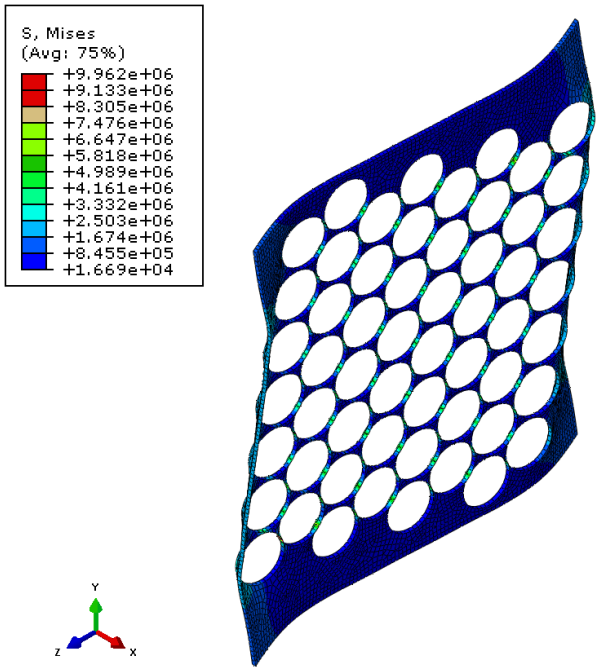

(c) $\boldsymbol{\sigma}_{123} = [0, 0, 0, 0, 1, 0]^{\mathrm{T}}$ MPa

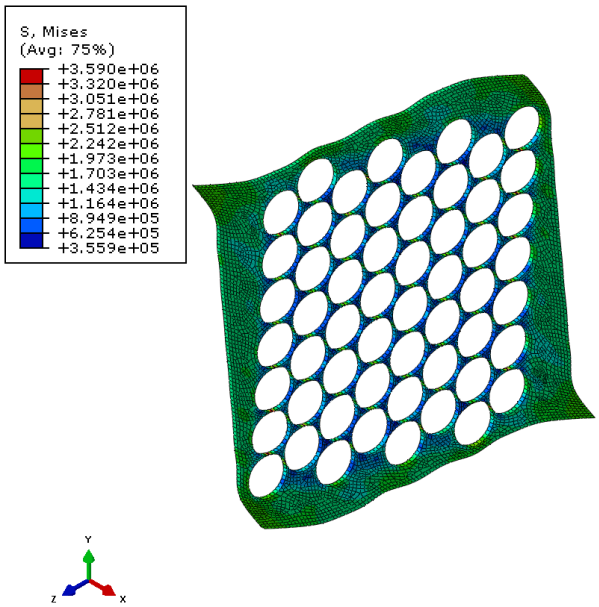

(d) $\boldsymbol{\sigma}_{123} = [0, 0, 0, 0, 0, 1]^{\mathrm{T}}$ MPa

Figure D.6: Equivalent von Mises stress on matrix elements of cluster unit cell **c** loaded by uniaxial stress.

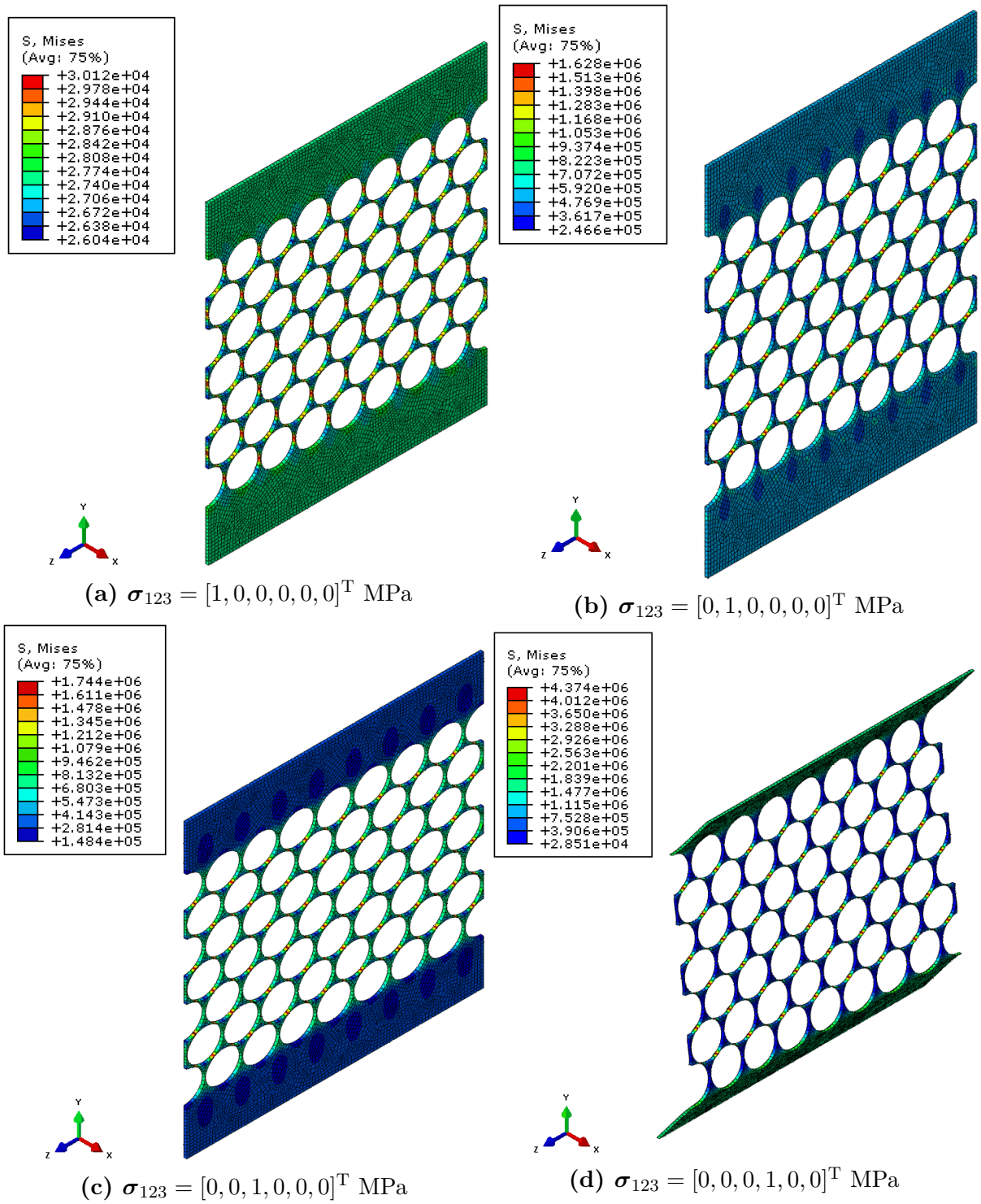

(a) $\boldsymbol{\sigma}_{123} = [1, 0, 0, 0, 0, 0]^{\mathrm{T}}$ MPa

(b) $\boldsymbol{\sigma}_{123} = [0, 1, 0, 0, 0, 0]^{\mathrm{T}}$ MPa

(c) $\boldsymbol{\sigma}_{123} = [0, 0, 1, 0, 0, 0]^{\mathrm{T}}$ MPa

(d) $\boldsymbol{\sigma}_{123} = [0, 0, 0, 1, 0, 0]^{\mathrm{T}}$ MPa

Figure D.7: Equivalent von Mises stress on matrix elements of stripe unit cell **d** loaded by uniaxial stress.

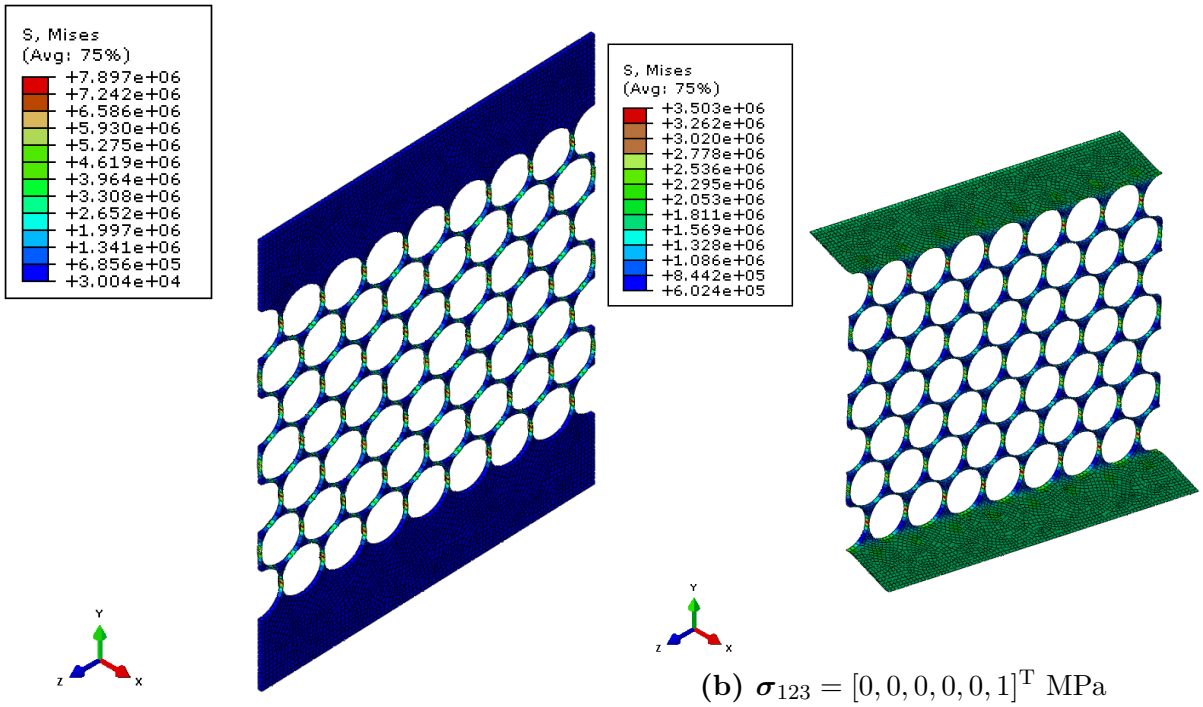

(a) $\boldsymbol{\sigma}_{123} = [0, 0, 0, 0, 1, 0]^{\mathrm{T}}$ MPa

(b) $\boldsymbol{\sigma}_{123} = [0, 0, 0, 0, 0, 1]^{\mathrm{T}}$ MPa

Figure D.8: Equivalent von Mises stress on matrix elements of stripe unit cell **c** loaded by uniaxial stress.

Bibliography

[1] Zemčík, R., Srbová, H., Ekštein, K., Medlín, R. Analysis of fiber distribution, size, and volume ratio of unidirectional composite plates with different thicknesses. *Materiali in Tehnologije*, 51:59–64, January 2017. ISSN 1580-2949.

[2] Srbová, H., Pirner, I., Zemčík, R., Medlín, R. Analysis of Fiber Distribution and Volume Ratio of Unidirectional Composite for Micromodels. *Transactions of the VŠB – Technical University of Ostrava, Civil Engineering Series*, 1(59):99–102, 2013. ISSN: 1213-1962.

[3] Srbová, H., Kroupa, T., Lukeš, V. Comparison of Homogenization Approaches Used for Identification of Material Parameters of Unidirectional Composite. *Materiali in Tehnologije*, 51(2), March 2017. ISSN 1580-2949.

[4] Srbová, H., Zemčík, R., Kroupa, T., Laš, V. Identification of the Material Parameters of a Unidirectional Fiber Composite Using a Micromodel. *Materiali in Tehnologije*, 46(5):431–434, 2012. ISSN: 1580-2949.

[5] Srbová, H., Kroupa, T., Zemčík, R. Identification of the Intial Failure and Damage of Substituents of a Unidirectional Fiber-reinforced Composite Using a Micromodel. *Materiali in Tehnologije*, 48(4):549–553, 2014. ISSN: 1580-2949.

[6] Kroupa, T., Srbová, H., Zemčík, R. Micromechanical model of substituents of unidirectional fiber reinforced composite and its response to tensile cyclic loading. *Materiali in Tehnologije*, 46(1):99–102, 2015. ISSN: 1580-2949.

[7] Kroupa, T., Srbová, H., Klesa, J. One Dimensional Elasto-plastic Material Model with Damage for Quick Identification of Material Properties. *Materiali in Tehnologije*, 51(2), April 2017. ISSN 1580-2949.

References

[8] Pinho-da-Cruz, J., Oliveira, J. A., Teixeira-Dias, F. Asymptotic homogenisation in linear elasticity. Part I: Mathematical formulation and finite element modelling. *Computational MAterials Science*, 45:1073–1080, 2009. ISSN: 0927-0256.

[9] Bensoussan, A., Lions J. L., Papanicolaou, G. *Asymptotic analysis for periodic structures*. American Mathematical Soc., New York, October 26 2011. ISBN-10: 0821853244.

[10] Hassani, B., Hinton, E. *Homogenization and Structural Topology*. Springer, London, 1998. ISBN-10: 3540762116.

[11] Flodén , L. G-convergence and homogenization of some sequeces of monotone differential operators. Mid Sweden University Doctoral Thesis 70, 2009. ISBN 978-91-86073-36-7.

[12] Ansini, N., Maso, G. D., Zeppieri, C. I. Γ-convergence and H-convergence of linear elliptic operators. *Journal de Mathématiques Pures et Appliquées*, 99(3):321–329, March 2013. ISSN: 1095-7154.

[13] Moes, N., Oden, J. T., Vemaganti, K., Remacle, J. F. Simplified methods and a posteriori error estimation for the homogenization of representative volume elements (RVE). *Computer Methods in Applied Mechanics and Engineering*, 176(1-4):265–278, July 1999. ISSN: 0045-7825.

[14] Wannier, G. H. *Statistical Physics*. Dover Publications, New York, 1966. ISBN: 9780486654010.

[15] Popov, V. L., Kröner, E. On the role of scaling in the theory of elastoplasticity. *Physical Mesomechanics*, 1:103–112, 1998. ISSN: 1029-9599.

[16] Rohan, E., Cimrman, R., Lukeš, V. Two-scale modeling of strongly heterogeneous continua using the homogenization approach. *Engineering Mechanics 2012, 18th International Conference*, pages 5–21, 2012. ISSN: 978-80-86246-40-6.

[17] Mori, T., Tanaka, K. Average stress in matrix and average elastic energy of materials with misfitting inclusions. *Acta Metallurgica*, 21(5):571–574, 1973.

[18] Mercier, S., Molinari, A. Homogenization of elastic-viscoplastic heterogeneous materials: Self-consistent and Mori-Tanaka schemes. *International Journal of Plasticity*, 25:1024–1048, 2009. ISSN: 0749-6419.

[19] Peng, X., Hu, N., Zheng, H., Fukunaga, H. Evaluation of mechanical properties of particulate composites with combined self-consistent and Mori-Tanaka approach. *Mechanics of Materials*, 41:1288–1297, 2009. ISSN: 0167-6636.

[20] Bayat, M., Aghdam, M. M. A micromechanics-based analysis of effects of square and hexagonal fiber arrays in fibrous composites using DQEMs. *European Journal of Mechanics A/Solids*, 32:32–40, 2012. ISSN: 0997-7538.

[21] Qing, H., Mischnaevsky, L. Jr. Unidirectional high fiber content composites: Automatic 3D FE model generation and damage simulation. *Computational Materials Science*, 47:548–555, 2009. ISSN: 0927-0256.

[22] Park, M. S., Kwon, Y. W. Elastoplastic micromechanics model for multiscale analysis of metal matrix composite structures. *Computers and Structures*, 123:28–38, 2013. ISSN: 0045-7949.

[23] Hill, R. Elastic Properties of Reinforced Solids: Some Theoretical Principles. *Journal of the Mechanics and Physics of Solids*, 11:357–372, 1963.

[24] Hashin, Z., Shtrikman, S. A variational approach to the theory of elasttic behaviour of multiphase materials. *Journal of the Mechanics and Physics of Solids*, 11:127–140, 1963.

[25] Hashin, Z., Rosen, B. W. The Elastic Moduli of Fiber Reinforced Materials. *Journal of Applied Mechanics*, 31:223–232, 1964.

[26] Halpin, J. C., Kardos, J. L. The Halpin-Tsai Equations: A Review. *Polymer Engineering and Science*, 16:344–352, 1976.

[27] Dvorak, G. *Micromechanics of Composite Materials*. Solid Mechanics and Its Applications. Springer Netherlands, 2012. ISBN 978-94-007-4100-3, DOI 10.1007/978-94-007-4101-0.

[28] Beran, M. J. Statistical Continuum Theories. *Monographs in Statistical Physics and Thermodynamics*, 9:+422, 1968. DOI: 10.1122/1.54899.

[29] Torquato, S., Stell, G. Microstructure of two-phase random media. I. The n-point probability functions. *Journal of Chemical Physics*, pages 2071–2077, 1982. DOI: 10.1063/1.444011.

[30] Šejnoha, M., Zeman, J. Micromechanical analysis of random composites. *CTU Reports*, 2002.

[31] Kochová, P.,Tonar, Z. Structural and Mechanical Properties of Gastropod Connective and Smooth Muscle Tissue. *Experimental Mechanics*, 54:791–803, 2014. DOI: 10.1007/s11340-014-9852-8.

[32] Decost, B. L.,Holm, E. A. A computer vision approach for automated analysis and classification of microstructural image data. *Computational Material Science*, 110:126–133, 2015.

[33] Boublík, T. *Statistical Thermodynamics*. Academia, 1996. ISBN: 8020005668.

[34] Hashin, Z.,Shtrikman, S. A variational approach to the theory of the elastic behaviour of multiphase materials. *Journal of the Mechanics and Physics of Solids*, 11:127–140, 1963. DOI: 10.1016/0022-5096(63)90060-7.

[35] Beicha, D., Kanit, T., Brunet, Y., Imad, A., El Moumen, A., Khelfaoui, Y. Effective transverse elastic properties of unidirectional fiber reinforced composites. *Mechanics of Materials*, 102:47–53, 2016.

[36] Peng, X., Hu, N., Zheng, H., Fukunaga, H. Effects of fiber volume fraction on transverse tensile properties of SiC/Ti-6Al-4V composites. *Rare Metal Materials and Engineering*, 40(4):575–579, 2011. ISSN: 18755372.

[37] Reavely, R. T., Kim, W. Method of fabricating fiber reinforced composite articles by resin transfer molding. *United States Patent*, Patent 4988469, Jan. 29 1991.

[38] Romanov, V., Lomov, S. V., Swolfs, Y., Orlova, S., Gorbatikh, L., Verpoest, I. Statistical analysis of real and simulated fibre arrangements in unidirectional composites. *Composites Science and Technology*, 87:126–134, 2013. ISSN: 0266-3538.

[39] Sorenson, B. F., Tarleja, R. Effects of nonuniformity of fiber distribution on thermally-induced residual stresses and cracking in ceramic matrix composites. *Mechanics of Materials*, 16:351–363, 1993. ISSN: 0167-6636.

[40] Kowalczyk, P. Parametric constitutive model of uni-directional fiber-matrix composite. *Finite Elements in Analysis and Design*, 50:243–254, 2012.

[41] Soden, P. D., Hinton, M. J., Kaddour, A. S. Lamina Properties, Lay-up Configurations and Loading Conditions for a Range of Fibre-reinforced Composite Laminates. *Composites Science and Technology*, 58:1011–1022, 1998.

[42] Barbič, J., Li, Y. Stable Orthotropic Materials. *Eurographics/ ACM SIGGRAPH Symposium on Computer Animation*, 2014.

[43] Feng, Y., Okamoto, R. J., Genin, G. M., Bayly, P. V. On the accuracy and fitting of transversley isotropic material models. *Journal of the Mechanical Behavior of Biomedical Materials*, 61:554–566, 2016.

[44] Standard test method for tensile properties of polymer matrix composite materials. Standard D 3039/D 3039M, ASTM International, West Conshohocken, United States, 2008.

[45] Plastics – determination of tensile properties – part 5: Test conditions for unidirectional fibre-reinforced plastic composites. Standard ISO 527-5:2009(E), International Organization for Standardization, Geneva, Switzerland, 2009.

[46] Aerospace series – carbon fibre reinforced plastics – unidirectional laminates – tensile test parallel to te fibre direction. Standard CSN EN 2561 (317710), Czech standards institute, Prague, Czech republic, 1998.

[47] Huntsman Advanced Materials. *Araldite AV 138M with Hardener HV 998*, 2004.

[48] Open Source Computer Vision. `http://docs.opencv.org/3.1.0/d3/db4/tutorial_py_watershed.html#gsc.tab=0`.

[49] Chauduri, S. `http://graphics.stanford.edu/`, Summer 2010.

[50] Wikipedia. Adaptive histogram equalization. `https://en.wikipedia.org/wiki/Adaptive_histogram_equalization`.

[51] Wikipedia. Histogram equalization. `https://en.wikipedia.org/wiki/Histogram_equalization`.

[52] Wikipedia. Otsu's method. `https://en.wikipedia.org/wiki/Otsu%27s_method`.

[53] Wikipedia. Random sample consensus. `https://en.wikipedia.org/wiki/Random_sample_consensus`.

[54] The Scipy community. Scipy documentation. `http://docs.scipy.org/doc/scipy/reference/generated/scipy.optimize.leastsq.html`.

[55] Python documentation. `https://python4mpia.github.io/fitting_data/least-squares-fitting.html`.

[56] Krig S. *Computer Vision Metrics,Survey, Taxonomy, and Analysis*. Apress.

[57] Křen, J., Rosenberg, J. *Continuum mechanics*. University of west Bohemia, Pilsen, CZ, 2006. ISBN 80-7082-908-7.

[58] Berthelot J., M. *Composite Materials: Mechanical Behavior and Structural Analysis*. Mechanical Engineering Series. Springer Science & Business Media.

[59] An in-depth tutorial on constitutive equations for elastic anisotropic materials. Report NASA/TM–2011-217314, National Aeronautics and Space Administration, Langley Research Center, Hampton, Virginia, 2011.

[60] de Souza Neto, E., Perić, D., Owen, D. *Computational methods for plasticity: theory and applications*. John Wiley and Sons Ltd, West Sussex, UK, 2008. ISBN 978-0-470-69452-7.

[61] Christensen R., M. *Mechanics of Composite Materials*. Dover Publications, Mineola, New York, USA, 2005. ISBN: 0-486-44239-X.

[62] National Physical Laboratory. *Manual for the Calculation of Elastic-Plastic Materials Models Parameters*. Crown copyright 2007.

[63] D. Lubachevsky, B. How to simulate billiards and similar systems. *Journal of Computational Physics*, 94(2):255–283, 1991.

[64] Dassault Systemes. *Abaqus Analysis User's Manual*.

[65] J. Yang P. Rozycki. Development about composite homogenization in static and in dynamic - application to ud composite materials. Master's thesis, Ecole Centrale de Nantes, Nantes, France.

[66] Plastics – determination of tensile properties – part 1: General principles. Standard ISO 527-1:2012, International Organization for Standardization, Geneva, Switzerland, 2012.

[67] Chowdhury, A., Kostem, C. N. Significance of mesh-fineness in accuracy of finite element analysis of hyperbolic cooling tower shells. *Computers & Structure*, 40:237–241, 1991. DOI: 10.1016/0045-7949(91)90350/U.

[68] Christensen R., M. Sufficient Symmetry Conditions for Isotropy of the Elastic Moduli Tensor. *Journal of Applied Mechanics*, 54:772–777, 1987. DOI: 10.1115/1.3173115.

[69] Gurit. *Spabond 345 EPOXY ADHESIVE SYSTEM*. Datasheet.

[70] Standard test method for tensile properties of plastics. Standard D 638-10, ASTM International, West Conshohocken, United States, 2010.